Design and Evaluation of a Photovoltaic Inverter with Grid-Tracking and Grid-Forming Controls

Rebecca Pilar Rye

Thesis submitted to the faculty of the

Virginia Polytechnic Institute and State University

in partial fulfillment of the requirements for the degree of

Master of Science

in

Electrical Engineering

Rolando Burgos, Chair

Steve C. Southward

Vassilis Kekatos

February 20, 2020

Blacksburg, Virginia

Keywords: control, three-phase, high-power, PLL, virtual synchronous machine, renewable energy, *dq* ac impedance, GNC, stability

Design and Evaluation of a Photovoltaic Inverter with Grid-Tracking and Grid-Forming Controls

Rebecca Pilar Rye

(ABSTRACT)

This thesis applies the concept of a virtual-synchronous-machine- (VSM-) based control to a conventional 250-kW utility-scale photovoltaic (PV) inverter. VSM is a recently-developed control scheme which offers an alternative grid-synchronization method to the conventional grid-tracking control scheme, which is based on the *dq* phase-locked-loop- (PLL-) oriented vector control. Synchronous machines inherently synchronize to the grid and largely partake in the stabilization of the grid frequency during power system dynamics. The purpose of this thesis is primarily to present the design of a grid-forming control scheme based on the VSM and the derivation of the terminal *dq*-frame ac impedance of the small-signal model of the inverter and control scheme. This design is also compared to the design of the conventional grid-tracking control structure, both from a loop design and terminal *dq*-frame ac impedance standpoint. Due to the inherent lax power-balance synchronization, the grid-forming control scheme results in 1 to 2 decades' lower frequency range of negative incremental input impedance in the diagonal elements, which is a favorable condition for stability. Additionally, the stability of the grid-forming control scheme is compared to the conventional grid-tracking control using the generalized Nyquist criterion (GNC) for stability under three modes of operation of active and reactive power injection. It is found that the connection is stable for both control schemes under unity power factor and fixed reactive power modes; however, the grid-forming control is able to inject twice the amount of active power under the voltage regulation mode when compared to the grid-tracking control.

Design and Evaluation of a Photovoltaic Inverter with Grid-Tracking and Grid-Forming Controls

Rebecca Pilar Rye

(GENERAL AUDIENCE ABSTRACT)

Concerns about the current and future state of the environment has prompted government and non-profit agencies to enact regulatory legislation on fossil fuel emissions. In 2017, electricity generation comprised 28% of total U.S. greenhouse gas emissions with 68% of this generation being due to coal combustion sources [1]. As a result, utilities have retired a number of coal power plants and have employed alternative means of power generation, specifically renewable energy sources (RES).

Most RES operate as variable-frequency ac sources (wind) or dc sources (solar) and are interfaced with the power grid through ac-dc-ac or dc-ac converters, respectively, which are power-electronic devices used to control the injection of power to the grid. Conventional converters synchronize with the grid by tracking the phase of the voltage at the point of common coupling (PCC) through a phase-locked loop (PLL). While power system dynamics significantly affect the performance of a PLL [2, 3], and, subsequently, inverters' operation, the initial frequency regulation during grid events is attributed to the system's inherent inertia due to the multitude of synchronous machines (SM). However, with the steady increase of RES penetration, even while retaining the number of SM units, the net inertia in the system will decrease, thus resulting in prolonged responses in frequency regulation to the aforementioned dynamics.

This thesis investigates the control of variable-frequency sources as conventional synchronous machines and provides a detailed design procedure of this control structure for photovoltaic (PV) inverter applications. Additionally, the stability of the connection of the inverter to the grid is analyzed using innovative stability analysis techniques which treat the inverter and control as a black box. In this manner, the inner-workings of the inverter need not be known, especially since it is proprietary information of the manufacturer, and the operator can measure the output response of the device to some input signal.

In this work, it is found that the connection between the inverter and grid is stable with this new control scheme and comparable to conventional control structures. Additionally, the control based on synchronous machine characteristics shows improved stability for voltage and frequency regulation, which is key to maintaining a stable grid.

Acknowledgments

First, I would like to extend my gratitude to my advisor, Dr. Rolando Burgos, for introducing me to the world of power electronics and bringing me into CPES. His guidance and feedback have been invaluable in completing the work for this degree. I would also like to extend my dearest thanks to him for his patience with me through the times of slow progress and for continuously pushing me over the course of the past few years in this uphill battle.

Thank you to my committee members, Dr. Steve Southward and Dr. Vassilis Kekatos, for their invaluable knowledge and input into controller design and power systems, respectively.

I would also like to thank the CPES industry members from Dominion Energy, specifically Mr. Kyle Thomas, Dr. Hung-Ming Chou, and Dr. Duotong Yang, for allowing me to learn about the practical applications of power electronic devices in the power system. It helps to have an idea of where the research will be applying.

Many thanks to the U.S. Department of Energy's Wide Bandgap Generation (WBGen) Graduate Research Assistantship for allowing me to pursue graduate research in power electronics and financially supporting this work.

My deepest thanks to my CPES peers who helped me on this journey: Mrs. Grace Watt Hunt, Mr. Slavko Mocevic, Mr. Victor Turriate, Mr. Joseph Kozak, Mr. Chris Salvo, Mr. Lee Gill, Mr. David Nam, Mr. Daniel Kellet, and Dr. Igor Cvetkovic.

To my close friend from CPES, Ms. Emma Raszmann, for the continued support and long nights with coffee in the lab. To my close friend from undergrad, Mr. Alex Freeman, whose humor makes electrical engineering seem far easier than it actually is. To my mentor,

Mrs. Ye Tang, whose insight and support in both research and life cannot be repaid.

To Mr. Howard Swingle, for being my soundboard for my research and making me realize my mistakes while talking out loud. To Dr. Nahum Arav, for taking my mind off research and talking about the cosmos and providing me weekly sanity checks.

To my parents, who have pushed me beyond my limits on multiple occasions. To my grandparents, for their continued support and encouragement. And to my sister, who listened to my endless qualms throughout the completion of this degree.

And, finally, to my best friend and life partner, Mr. Reed Schadegg, for putting up with me and endlessly supporting me throughout this degree. Without you, this would have never been published.

Contents

List of Figures

List of Tables

Chapter 1

Introduction

1.1 Background

Recently, the concept of a virtual synchronous machine (VSM) has been introduced as a means of emulating synchronous machine (SM) in a converter's control scheme [4, 5]. In [6], Zhong introduces the concept of a synchronverter which mimics a real synchronous generator by using the detailed equations which represent the machine. Zhong goes further in [7] to provide a control strategy to synchronize the synchronverter to the grid, which is of key importance for any unit being tied to the grid.

In [8–12], the concept of a synchronous power converter (SPC) is introduced. The control is based on a dual-loop control structure, similar to the conventional PLL control, but instead uses a modified swing equation for synchronization. Additionally, the concept of virtual impedance, which mimics the impedance of a real SM, is included in the control structure to generate references for an inner control loop. The synchronization method for the SPC is explored in [13–16], where the concept is similar to that of the synchronverter in that a virtual current and measured voltage is provided to the controller, to which the SPC is able to match the voltage waveforms and connect to the grid with zero power injection. Experimental validation of the SPC controller synchronizing to and operating with the grid is provided in [17], in which it is shown that the SPC has an improved performance compared to the PLL-oriented vector control in response to grid frequency disturbances.

Until recently, however, no detailed design of the virtual synchronous machine controller was provided. In [18–20], a design procedure is detailed for a grid-tied static synchronous compensator (STATCOM) with VSM control based on the SPC concept. In [20] and [18], specifically, the effect of the virtual inertia and virtual impedance parameters on the control

loops and impedance of the inverter, respectively, is also explored, thus giving insight on selecting the parameters appropriately. However, while the concept of a PV inverter with SPC control has been explored in [21], no detailed explanation of such a controller for PV application has been provided.

In addition to the design of the VSM-based controller for renewable energy applications, it is important to analyze the stability of such a connection to the grid since this is a relatively new control schematic. A conventional means of stability analysis is to use classical methods, such as the analysis of participation factors, as in [22, 23]. Stability analysis for the SPC using participation factors and parametric sensitivities is presented in [24, 25]; however, this requires that every part of the system under study, including the inverter and control parameters, are known. Since inverters comprise manufacturer proprietary information, this is not a feasible method for analyzing the stability of a real unit. As a result, Wen develops a method of stability analysis for three-phase ac systems using *dq*-frame terminal ac impedance, as presented in [26] and in his dissertation, [27], in which the generalized Nyquist criterion (GNC) for stability can be applied to analyze the stability of the connection [28]. The benefit of using the terminal *dq*-frame ac impedance is that the parameters of the system are not required to be known; instead, the inverter remains a black box and a voltage perturbation is provided at the terminal of the inverter and the resulting current is measured. With these two known values, the ac impedance can be measured and GNC can be applied. This method of stability analysis is presented in [29–32] for a utility-scale grid-tied PV inverter with PLL-oriented *dq*-frame vector control. However, this form of stability analysis has not been performed for PV inverter with a VSM-based control structure.

1.2 Synchronization Methods

Maintaining synchronization with the grid at the point of common coupling (PCC) is one of the fundamental functionalities of a grid-tied inverter, even before any other control. The reasoning for this is due the necessity of maintaining the grid frequency at 60 Hz (or 50 Hz, depending on the country) to ensure the continued stable operation of the grid.

In order to synchronize to the grid, the terminal voltage of the PV inverter must match in voltage phase, frequency, and amplitude, within a given range of error defined by IEEE 1547-2018 [33]. This work explores two methods of synchronization: 1) phase-locked loop, which obtains the phase information of the voltage at the PCC, and 2) power-balance synchronization, which partakes in frequency regulation and mimics the synchronization method of a conventional synchronous machine.

1.2.1 Phase-Locked Loop

A synchronous-reference-frame phase-locked loop (SRF-PLL) is the conventional method of synchronizing the inverter to the grid. In order to synchronize the inverter to the ac grid, a PLL is used as shown in Fig. 1.1 [34]. This PLL scheme comprises three main components: a phase detector (PD), a loop filter (LF), and a voltage controlled oscillator (VCO) [35]. The PD generates a signal which is proportional to the phase difference between the measured voltage signal and that of the voltage signal generated by the PLL. The LF is designed to attenuate the high-frequency ac components generated by the PD. Finally, the VCO generates an ac signal with a frequency which varies with respect to a nominal frequency. In essence, the PLL aims to mitigate the phase difference between the inverter and grid, which results from dynamics either on the grid or inverter side [36].

Although the SRF-PLL is simple in its control and has a quick response under normal

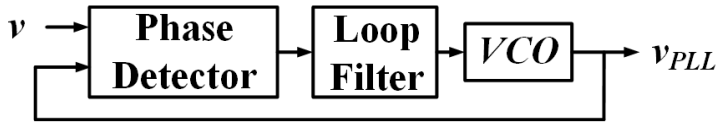

Figure 1.1: Basic structure of a PLL.

operating conditions, its performance is mediocre under unbalanced three-phase conditions [2]. If the unbalance is severe enough, the SRF-PLL may not even be able to track the positive sequence of the voltage accurately enough to maintain synchronization. Of course, other design schemes for a PLL have been analyzed, such as the decoupled double synchronous reference frame phase-locked loop (DDSRF-PLL), which aims to accurately track the positive-sequence voltage even under unbalanced conditions [37–39]. Another design is a PLL based on the fast Fourier transformation (FFT-PLL), which applies FFT instead of PI feedback control like the SRF-PLL and DDSRF-PLL [40, 41]. However, the phase of the tracked voltage is only equal to the positive sequence three-phase voltage when the system is balanced. It has been shown that the PLL's performance is significantly affected by power system dynamics [2].

1.2.2 Power-Balance Synchronization

Under nominal grid conditions, synchronous machines (SM) are synchronized to the grid frequency ω_n; this results in a balance between the input mechanical power, P_m, and the output electrical power, P_e, if the damping coefficient, D, is neglected. However, during system disturbances, the frequency fluctuation will cause the rotor speed to fall out of sync with the grid frequency, resulting in an accelerating power P_a and a power angle of δ, where P_a is a function of the inertia J and angular acceleration, ω. It should be noted that δ is the same angle difference between the rotating grid frame and the rotating controller frame discussed in 3.2.1.

Additionally, to avoid hunting, a damping coefficient should be included to model the

damping winding in a physical SM. With these considerations, the swing equation in (1.1) can be constructed to describe the dynamic behavior of an SM.

$$\begin{aligned} \frac{d\delta}{dt} &= \omega - \omega_n \\ J\omega_n \frac{d^2\delta}{dt^2} &= P_a = P_m - P_e - D\omega_n \left(\frac{d\delta}{dt}\right) \end{aligned} \tag{1.1}$$

In a similar fashion, the swing equation can be modified for a virtual synchronous machine in inverter control such that the mechanical power is represented by the active power at the dc-link, P_{dc}, and the electrical power is represented by the active power at the point of common coupling (PCC), P_{ac}. Therefore, the swing equation is rewritten as

$$\begin{aligned} \frac{d\delta}{dt} &= \omega - \omega_n \\ J\omega_n \frac{d^2\delta}{dt^2} &= P_{dc} - P_{ac} - D\omega_n \left(\frac{d\delta}{dt}\right) \end{aligned} \tag{1.2}$$

In this manner, when ω is greater than the nominal frequency, ω_n, then the power angle, δ, will also increase, causing the ac active power P_{ac} to increase. As a result, ω will decrease due to the braking effect of P_{dc}, causing the two frames to realign. As such, it is clear to see that this method of synchronization is grid-forming.

1.3 Motivation and Objective

The concept of the virtual synchronous machine has been discussed in several papers, as mentioned in 1.1. Additionally, it has been shown that this control structure offers an improved performance over the conventional PLL-oriented vector control due to the inherent frequency and voltage support offered by a synchronous machine. However, only a few papers discuss the design procedure for a VSM-based control, and only for STATCOM applications.

Due to the increase in penetration of renewable energy resources in the grid, it is necessary

to consider a VSM-based control of these sources such that they provide frequency and voltage support similar to synchronous generators. Therefore, it is necessary to also provide a design procedure for VSM-based control for these renewable energy applications, such as solar, and to analyze the stability of such a design in a manner that the inverter is a black box, in which only the inputs to and outputs from the system are known.

1.4 Thesis Organization

The remainder of this thesis is organized as follows:

Chapter 2 covers the modeling procedure of PV arrays, including the derivation of the equivalent model, as well as the derivation of the equations used to describe the power stage of the inverter. Additionally, switching network topologies are discussed, from which one is chosen to be used in the small-signal model derivation of the power stage, which is used in later chapters for small-signal stability analysis.

Chapter 3 discusses the basics of a phase-locked loop and the design of a grid-tracking dq-frame PLL-oriented vector control scheme for PV inverter with active and reactive power injection capability. The terminal dq-frame ac impedance of the PV inverter is derived for unity power factor, fixed reactive power, and volt-var control modes. An analysis of the dq impedance is provided.

Chapter 4 focuses on a detailed derivation of a grid-following control scheme which aims to emulate the characteristics of a synchronous machine. The designed control scheme also takes into consideration the injection of active and reactive control under the same control modes as investigated in Chapter 3. Additionally, the terminal dq-frame ac impedance of the PV inverter is derived, verified, and compared to the impedance obtained for the grid-tracking control scheme. Lastly, the influence of key parameter variations, such as virtual

inertia and virtual impedance, on the terminal impedance is investigated.

Chapter 5 utilized the generalized Nyquist criterion (GNC) for stability to analyze the small-signal stability of the grid-tracking and grid-forming control. Using this technique for stability analysis, a comparison between the maximum stable power injection for both control schemes is compared under the voltage regulation control mode, volt-var, in which it is found that the grid-tracking control is unstable.

Finally, Chapter 6 concludes the thesis, presenting the key accomplishments of this work. Additionally, future considerations are provided to continue the work presented in this thesis.

Chapter 2

Modeling of Grid-Tied Photovoltaic Inverters

2.1 Introduction

This chapter covers the derivation of the small-signal model for the power stage of the grid-tied photovoltaic (PV) inverter. The inverter topology under consideration is shown in Fig. 2.1. It consists of a 250-kW PV array connected to a 330-V ac bus through an LCL filter, whose values are shown in Table 2.1. The small-signal model obtained in this chapter is used in Ch. 3 and Ch. 4 in the development of the small-signal model of the system with grid-tracking and grid-forming control, which is then used in Ch. 5 for the analysis of the small-signal stability.

Table 2.1: LCL Filter Values

L_c	0.32 mH
R_c	1 mΩ
L_g	0.32 mH
R_g	1 mΩ
C_f	70.3 μF
R_f	0.5027 Ω
C_{dc}	8.2 mF

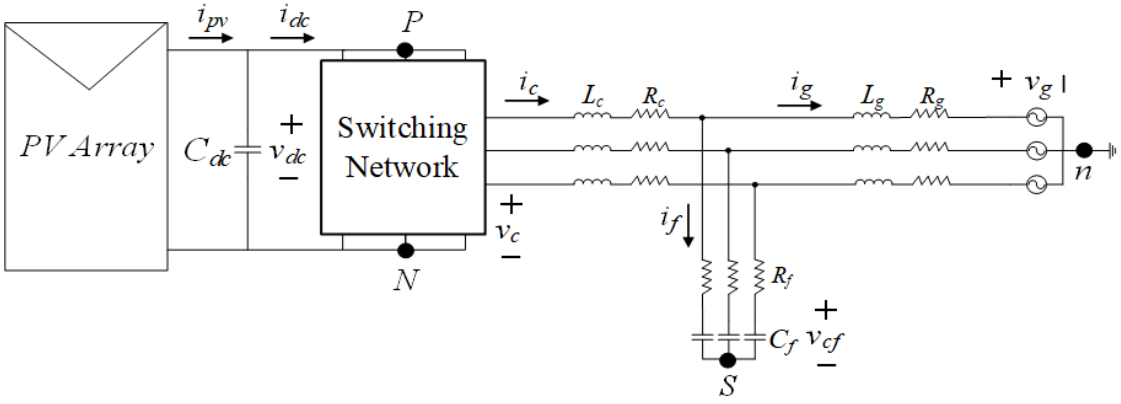

Figure 2.1: PV inverter topology.

2.2 Modeling of PV Arrays

Photovoltaic (PV) arrays comprise of a string of modules connected in parallel, where each string consists of modules connected in series. By adjusting the number of parallel strings or series-connected modules, the characteristic curve of the PV array is adjusted and the maximum power point (MPP) is adjusted. The PV array can be modeled as shown in Fig. 2.2, where the source current is I_L, the current through the diode is I_d, and the output current of the PV array is i_{pv}. The equation which defines the relationship between the output current and terminal voltage is (2.1) [42].

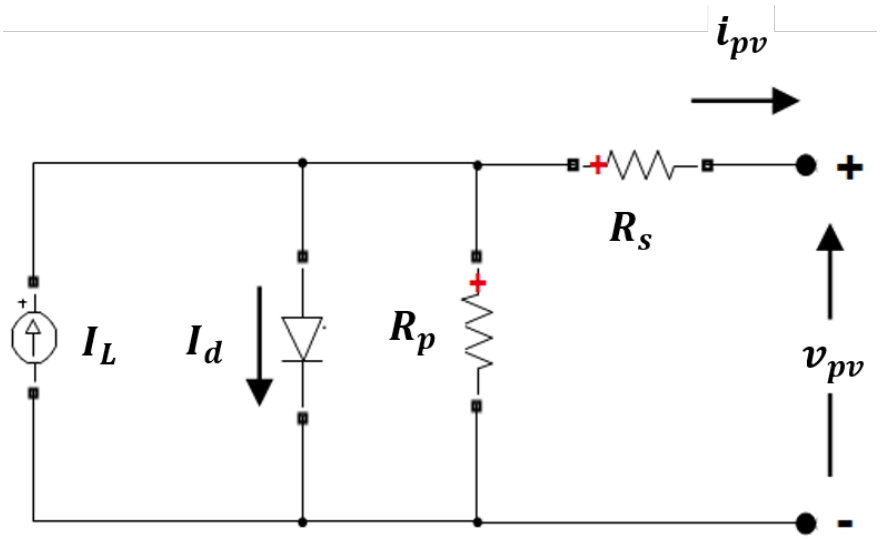

Figure 2.2: PV array equivalent model.

$$i_{pv} = I_L - I_0 \left[\exp\left(\frac{v_{pv} + R_s i_{pv}}{V_t a} \right) - 1 \right] - \frac{v_{pv} + R_s i_{pv}}{R_p} \tag{2.1}$$

where I_0 is the saturation current; $V_t = N_s kT/q$ is the thermal voltage such that N_s is the number of cells connected in series, k is the Boltzmann constant, q is the electron charge, and T is the temperature of the PV cells in Kelvin; R_s is the series resistance; R_p is the shunt resistance; and a is the ideality constant of the diode.

The derivative of the non-linear $i \times v$ characteristic curve of a PV array at an operating point defined by (V_{PV}, I_{PV}) is [42]

$$g(V_{PV}, I_{PV}) = -\frac{I_0}{V_t N_s a} \exp\left(\frac{V_{PV} + I_{PV} R_s}{V_t N_s}\right) - \frac{1}{R_p} \tag{2.2}$$

from which the linear model is defined as the line that runs tangent to the derivative of the non-linear curve at some operating point such that

$$i_{pv} = (-g V_{PV} + I_{PV}) + g v_{pv} \tag{2.3}$$

Now, consider the simple circuit shown in Fig. 2.3, in which the output current, i_{pv}, is

$$i_{pv} = \frac{V_{eq} - v_{pv}}{R_{eq}} \tag{2.4}$$

Then, by comparing (2.4) with (2.3), it is seen that

$$R_{eq} = -\frac{1}{g} \qquad \text{and} \qquad V_{eq} = V_{PV} - \frac{I_{PV}}{g}$$

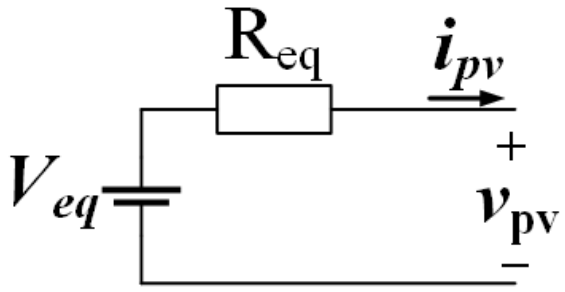

Figure 2.3: PV array equivalent model with voltage source.

A separate way to obtain the values for the equivalent voltage source and resistance, V_{eq} and R_{eq}, respectively, can be done in the simulation environment in MATLAB Simulink. The PV array model can be connected to a dc voltage source, as shown in Fig. 2.4, where the dc voltage source represents the desired dc-link voltage, v_{dc}. The dc voltage source can then be given a small-signal perturbation, $\tilde{v}_{dc}$ and the current can be measured. In this manner, a transfer function from the voltage to the current is obtained, which is representative of the conductance. By taking the inverse of this value, the equivalent resistance can be obtained directly. The equivalent voltage is then calculated as

$$V_{eq} = V_{dc} + \frac{P_{dc}}{V_{dc}} R_{eq} \tag{2.5}$$

where V_{dc} is the steady-state value of the dc-link voltage and P_{dc} is the steady-state value of the active power injection of the PV array.

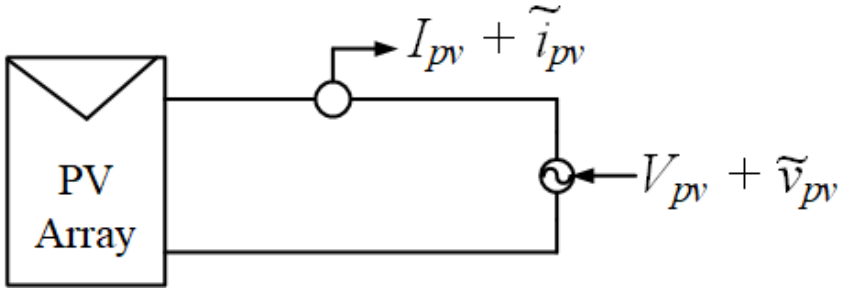

Figure 2.4: Small-signal perturbation of PV array to obtain equivalent model.

It should be noted that the values of the equivalent voltage and resistance which are used to represent the PV array are only valid for the operating point at which they were obtained. Therefore, this method is only useful for steady-state and small-signal analysis and should not be used to investigate dynamic responses of the PV system to grid fluctuations, contingencies, or events.

2.3 Inverter Modeling

This section covers various switching network topologies used for modern-day inverters, including multilevel configurations. Additionally, the equations used to describe the converter layout are derived, from which the small-signal model of the power stage is obtained. This small-signal model is used in later chapters in the analysis of the small-signal stability of the system.

2.3.1 Switching Network Topology

There are various topologies for the switching network of an inverter, the simplest of which is a two-level, three-phase configuration, as shown in Fig. 2.5 [43]. The two-level topology yields $-v_{dc}$ or v_{dc} at the ac-side terminal based on the switching of the power electronics, here modeled as IGBTs. It should be noted that the switching network can be comprised of any switching device, including IGBTs, GTOs, and thyristors, which are the most commonly used.

However, the two-level, three-phase configuration does not mitigate harmonics well enough

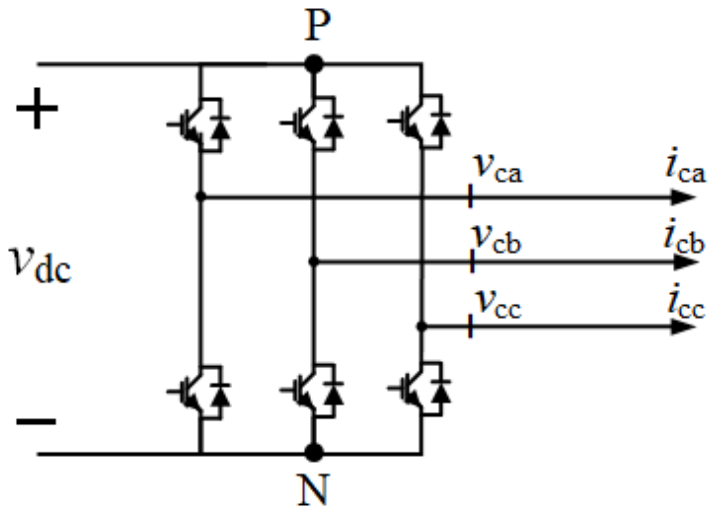

Figure 2.5: Two-level, three-phase switching network.

for grid-connection standards, specifically IEEE 519-2014 [44], and, therefore, also has a significantly high total harmonic distortion (THD). Although improvements to this topology have been proposed, as in [45, 46], there still exist superior topologies which are better suited for high-voltage applications, offer more modularity, and inherently have a reduced harmonic content [47].

One such general configuration is known as the multilevel converter topology, of which there are three types: 1) diode-clamped, 2) capacitor-clamped, and 3) cascaded [48–53]. In the diode-clamped, also known as neutral-point-clamped as shown in Fig. 2.6, configuration, the dc-bus comprises $n-1$ capacitors, where n is the level of the converter and produces n levels of the phase voltage on the ac bus. The voltage across each capacitor is the total dc bus voltage divided by the number of capacitors and, therefore, the produced phase voltage is clamped by the diodes. For this configuration, there exists a unique switching sequence to produce each voltage level which, while it results in a simplified control, requires different voltage and current ratings for the switching devices due to reverse voltage blocking and unequal conduction, respectively. Additionally, the diode-clamped multilevel structure can be used to mitigate harmonics if the number of levels is high enough; however, this also increases cost, so a balance must be found [54, 55].

The capacitor-clamped, or flying-capacitor, configuration is similar to that of the diode-clamped configuration in that $n-1$ capacitors are required to produce an n-level converter. Once again, with the higher level converter, the harmonics are mitigated and may even be enough to avoid the use of a filter; however, the higher the level of the converter, the harder it is to package and the more expensive the system due to the necessary amount of capacitors needed for such a configuration. On the other hand, the quantity of capacitors allows for ride-through capability during system dynamics, but the overall control of the inverter will

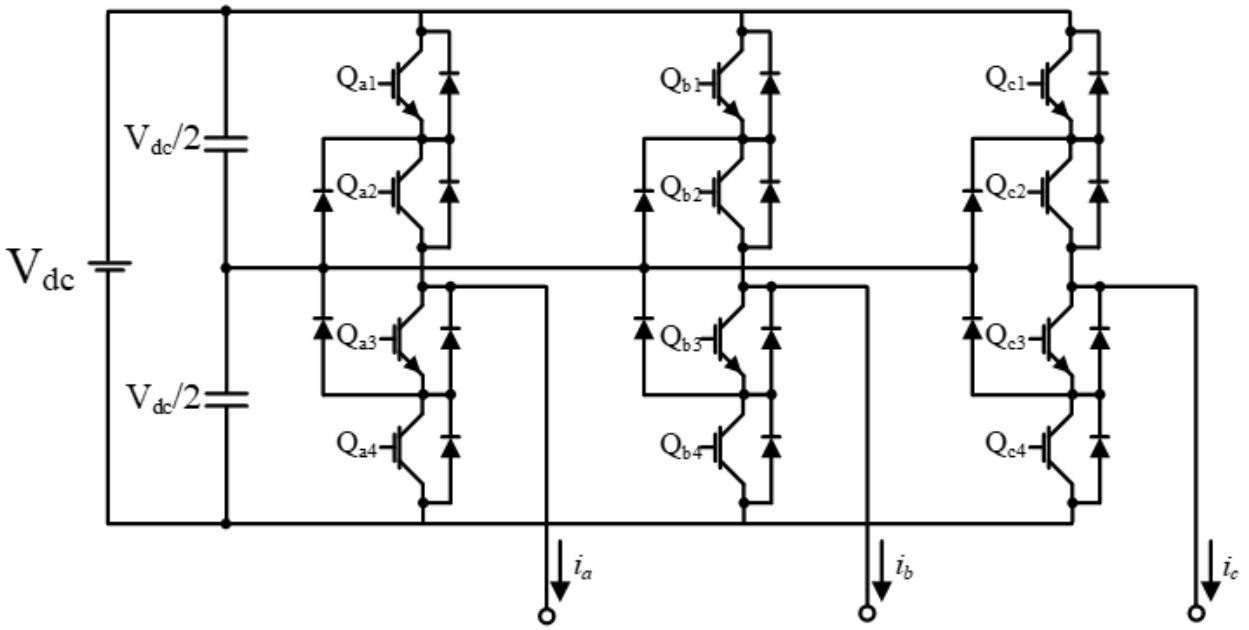

Figure 2.6: Three-phase, three-level neutral-point-clamped switching topology.

be far more complex compared to the diode-clamped configuration. Unfortunately, the need for a high switching frequency will result in high switching losses for active power injection.

Finally, the cascaded multilevel structure comprises separate dc sources per level, in which each level is a single-phase full-bridge inverter and the ac terminal voltage of each level is connected in series. This configuration is well-suited for renewable energy generation as each source can be used as the dc source per level. Additionally, this configuration requires the fewest number of components when compared to the diode- and capacitor-clamped structures to reach the same voltage level. Another advantage is that the layout and packaging of this configuration is modular, since each level is comprised of the same topology.

However, since this work focuses on the design, implementation, and evaluation of the controller of a PV inverter, the topology of the switching network is not necessarily an important consideration since an average model of the switching network will be used to analyze the small-signal stability of the system in Ch. 5. Therefore, if the THD requirement

is met and the inverter operates as needed, then the simple two-level, three-phase topology can be used for the sake of simplicity.

Since this work primarily focuses on the analysis of the small-signal stability of the PV inverter and control, then it is necessary to obtain the small-signal representation of the power stage of the inverter. For control design and stability analysis, the switching network of the two-level, three-phase configuration can be simplified as ideal switches, as shown in Fig. 2.7. For any given branch, when one switch is closed, its complementary is open and vice versa. In other words,

$$s_{ip} + s_{in} = 1, \qquad i \in \{a, b, c\} \tag{2.6}$$

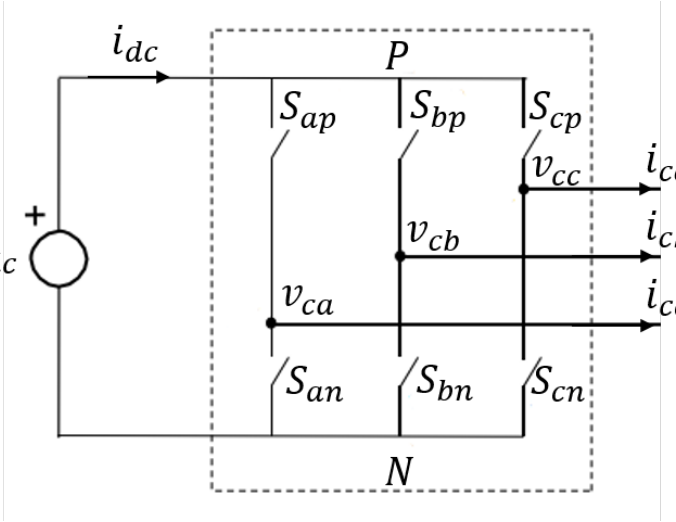

Figure 2.7: Switching devices modeled as ideal switches.

The ideal switch can be further simplified to a single-pole-double-throw switch such that

$$s_i = s_{ip} = 1 - s_{in}, \qquad i \in \{a, b, c\} \tag{2.7}$$

as shown in Fig. 2.8. The three-phase output voltages and dc-side current, respectively, are given by [27, 56]

$$\begin{bmatrix} v_{ca} \\ v_{cb} \\ v_{cc} \end{bmatrix} = \begin{bmatrix} S_a \\ S_b \\ S_c \end{bmatrix} v_{dc} \tag{2.8}$$

$$i_{dc} = [S_a \quad S_b \quad S_c] \begin{bmatrix} i_{ca} \\ i_{cb} \\ i_{cc} \end{bmatrix} \tag{2.9}$$

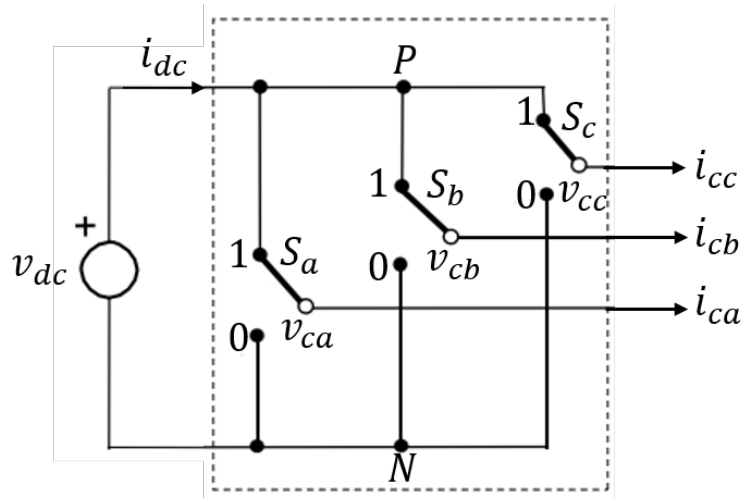

Figure 2.8: Switching devices modeled as single-pole-double-throw ideal switches.

In this work, it is assumed that the ratio of the switching-to-line frequency is high enough such that the variations of the ac-terminal voltages and dc-side current is negligible [57]. As such, then the switching function can be averaged to obtain the duty cycle of the switch, such that

$$d_i = \frac{1}{T} \int_{t-T}^{t} s_i(\tau) d\tau \quad i \in \{a, b, c\} \tag{2.10}$$

In this manner, then (2.8) and (2.9) are rewritten as

$$\begin{bmatrix} v_{ca} \\ v_{cb} \\ v_{cc} \end{bmatrix} = \begin{bmatrix} d_a \\ d_b \\ d_c \end{bmatrix} v_{dc} \tag{2.11}$$

$$i_{dc} = [d_a \quad d_b \quad d_c] \begin{bmatrix} i_{ca} \\ i_{cb} \\ i_{cc} \end{bmatrix} \tag{2.12}$$

The average model of the switching network is shown in Fig. 2.9.

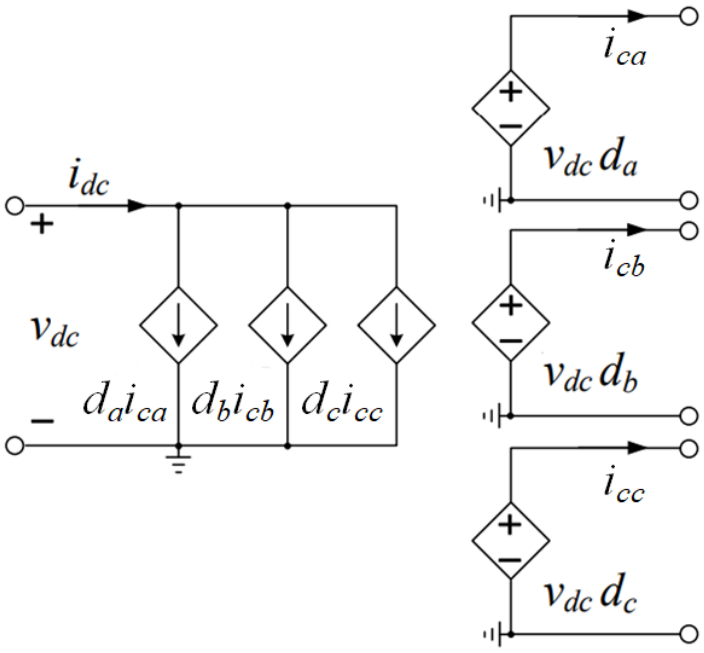

Figure 2.9: Average model of switching network.

2.3.2 Computation and PWM Delay

Due to the digital control of the inverter, two significant delays are introduced. The first delay is due to the computation time required by the controller and the second is due to the pulse-width modulation (PWM) [58, 59].

The computation delay is considered as the time lapsed from the moment a signal is sampled to the moment the PWM reference is updated, which is one sampling period ($T_{del-comp} = T_s$), in which a single ($f_s = f_{sw}$) or double ($f_s = 2f_{sw}$) update is implemented [60]. The delay due to PWM is due to the zero-order hold, which keeps the PWM signal constant after it has been updated, thus resulting in a delay of half a sampling period, ($T_{del-PWM} = 0.5T_s$). Therefore, the total delay is the sum of the individual delays, such that $T_{del} = T_{del-comp} + T_{del-PWM} = 1.5T_s$. In a continuous-time system, a delay of T_{del} seconds is

$$e^{-sT_{del}} \tag{2.13}$$

This can be approximated using a Padé approximant such that

$$1^{st} \text{ order approximation:} \qquad e^{-sT_{del}} \approx \frac{-\left(T_{del}\right)s + 2}{\left(T_{del}\right)s + 2} \tag{2.14}$$

$$2^{nd} \text{ order approximation:} \qquad e^{-sT_{dc}} \approx \frac{\left(T_{del}\right)^2 s^2 - 6\left(T_{del}\right)s + 12}{\left(T_{del}\right)^2 s^2 + 6\left(T_{del}\right)s + 12} \tag{2.15}$$

$$3^{rd} \text{ order approximation:} \qquad e^{-sT_{del}} \approx \frac{-\left(T_{del}\right)^3 s^3 + 12\left(T_{del}\right)^2 s^2 - 60\left(T_{del}\right)s + 120}{\left(T_{del}\right)^3 s^3 + 12\left(T_{del}\right)^2 s^2 + 60\left(T_{del}\right)s + 120} \tag{2.16}$$

In this work, a first-order approximation of the delay will be considered, such that the small-signal equation of the delay is shown in (2.17) [27, 29, 61].

$$\mathbf{G_{del}} = \begin{bmatrix} \frac{1-0.5T_{del}s}{1+0.5T_{del}s} & 0 \\ 0 & \frac{1-0.5T_{del}s}{1+0.5T_{del}s} \end{bmatrix} \tag{2.17}$$

2.3.3 Small-Signal Model

In order to design the control of the inverter, the small-signal model of the power stage must first be obtained [57]. To do so, Kirchhoff's Voltage Law (KVL) and Kirchhoff's Current Law (KCL) are used. First, KVL is used on the loop defining the path of the converter-side current, i_c, to the wye-connected capacitor branch of the LCL filter such that the a-phase loop is

$$-v_{ca} + L_c\frac{i_{ca}}{dt} + (R_c + R_f)i_{ca} - R_f i_{ga} + v_{cfa} + v_{SN} = 0 \tag{2.18}$$

The potential between the neutral point of the wye-connection to the negative terminal of the switching network is modeled as shown in (2.19) by considering the fact that the sum of the currents flowing into the node is zero.

$$v_{SN} = \frac{1}{3}(v_{ca} + v_{cb} + v_{cc}) + \frac{1}{3}(-v_{cfa} - v_{cfb} - v_{cfc}) \tag{2.19}$$

Substituting (2.19) into (2.18) and considering the average model of the switching network from 2.3.1, then extending to all three phases and solving for $\frac{di_c}{dt}$ yields

$$\frac{d\mathbf{i}_c}{dt} = \frac{1}{L_c}\left(\frac{1}{3}\begin{bmatrix} 2 & -1 & -1 \\ -1 & 2 & -1 \\ -1 & -1 & 2 \end{bmatrix}\mathbf{d}v_{dc} - (R_c + R_f)\,\mathbf{i}_c + R_f\mathbf{i}_g + \frac{1}{3}\begin{bmatrix} -2 & 1 & 1 \\ 1 & -2 & 1 \\ 1 & 1 & -2 \end{bmatrix}\mathbf{v}_{Cf}\right) \tag{2.20}$$

KVL is then applied to the path of the grid-side current, i_g, such that the a-phase loop

is defined as

$$-v_{cfa} + L_g \frac{di_{ga}}{dt} + (R_g + R_f) i_{ga} - R_f i_{ca} + v_{ga} + v_{nS} = 0 \tag{2.21}$$

The potential between the neutral point of the wye-connected shunt capacitor branch and the ground of the grid-side voltage is

$$v_{nS} = \frac{1}{3}(v_{cfa} + v_{cfb} + v_{cfc}) + \frac{1}{3}(-v_{ga} - v_{gb} - v_{gc}) \tag{2.22}$$

Substituting (2.22) into (2.21) and considering the average model of the switching network from 2.3.1, then extending to all three phases and solving for $\frac{di_g}{dt}$ yields

$$\frac{d\mathbf{i}_g}{dt} = \frac{1}{L_g}\left(\frac{1}{3}\begin{bmatrix} 2 & -1 & -1 \\ -1 & 2 & -1 \\ -1 & -1 & 2 \end{bmatrix} \mathbf{v}_{Cf} + R_f \mathbf{i}_c - (R_g + R_f)\,\mathbf{i}_g + \frac{1}{3}\begin{bmatrix} -2 & 1 & 1 \\ 1 & -2 & 1 \\ 1 & 1 & -2 \end{bmatrix} \mathbf{v}_g \right) \tag{2.23}$$

KCL is applied to the node of the shunt capacitor branch such that

$$\begin{aligned} i_{fa} &= i_{ca} - i_{ga} \\ C_f \frac{di_{fa}}{dt} &= i_{ca} - i_{ga} \end{aligned} \tag{2.24}$$

Extending to all three phases yields

$$\frac{d\mathbf{v}_{Cf}}{dt} = \frac{1}{C_f}\left(\mathbf{i}_c - \mathbf{i}_g\right) \tag{2.25}$$

Finally, KCL is applied to the dc-side currents at the node defined by the dc-bus capacitor such that

$$i_{pv} = i_{Cdc} + i_{dc} \tag{2.26}$$

Recall from 2.2 that the PV array is modelled as a voltage source in series with a resistor. Therefore, i_{pv} in (2.26) is expressed as the potential difference between the voltage source and voltage across the capacitor and i_{dc} may be rewritten in terms of the average model of the switching network from 2.3.1 such that

$$\frac{dv_{dc}}{dt} = \frac{1}{C_{dc}}\left(\frac{V_{eq}}{R_{eq}} - \frac{v_{dc}}{R_{eq}} - d_a i_{ca} - d_b i_{cb} - d_c i_{cc}\right) \tag{2.27}$$

Since the stationary *abc* frame does not result in a dc equilibrium point which may be used in the control scheme, then the derived KVL and KCL equations are transformed to the rotating *dq* frame. To transform to the *dq*0 frame from the *abc* frame, the following relationship can be formed:

$$\mathbf{x}_{abc} = T^{-1}_{dq0/abc}\mathbf{x}_{dq0} \tag{2.28}$$

where

$$T_{dq0/abc} = \sqrt{\frac{2}{3}}\begin{bmatrix} \cos(\delta) & \cos(\delta - \frac{2\pi}{3}) & \cos(\delta + \frac{2\pi}{3}) \\ -\sin(\delta) & -\sin(\delta - \frac{2\pi}{3}) & -\sin(\delta + \frac{2\pi}{3}) \\ \frac{1}{\sqrt{2}} & \frac{1}{\sqrt{2}} & \frac{1}{\sqrt{2}} \end{bmatrix} \tag{2.29}$$

It should be noted that the obtainment of δ is derived in Ch. 3 and Ch. 4 for each control mode and will not be discussed in this chapter. In essence, this variable is used in the transformation of stationary-frame variables to rotating-frame variables.

Applying (2.28) to (2.20) yields

$$\begin{aligned}\frac{d(T_{dq0/abc}^{-1}\mathbf{i}_{c,dq})}{dt} &= \frac{1}{3L_c}\begin{bmatrix}2 & -1 & -1\\ -1 & 2 & -1\\ -1 & -1 & 2\end{bmatrix}(T_{dq0/abc}^{-1}\mathbf{d}_{dq})v_{dc} - \frac{(R_c+R_f)}{L_c}(T_{dq0/abc}^{-1}\mathbf{i}_{c,dq}) \\ &+ \frac{R_f}{L_c}(T_{dq0/abc}^{-1}\mathbf{i}_{g,dq}) + \frac{1}{3L_c}\begin{bmatrix}-2 & 1 & 1\\ 1 & -2 & 1\\ 1 & 1 & -2\end{bmatrix}(T_{dq0/abc}^{-1}\mathbf{v}_{Cf,dq})\end{aligned} \tag{2.30}$$

Pre-multiplying both sides through by $T_{dq0/abc}$ yields

$$\begin{aligned}\left(T_{dq0/abc}\frac{dT_{dq0/abc}^{-1}}{dt}\right)\mathbf{i}_{c,dq} + \frac{d\mathbf{i}_{c,dq}}{dt} &= \frac{1}{3L_c}\left(T_{dq0/abc}\begin{bmatrix}2 & -1 & -1\\ -1 & 2 & -1\\ -1 & -1 & 2\end{bmatrix}T_{dq0/abc}^{-1}\right)\mathbf{d}_{dq}v_{dc} \\ &- \frac{(R_c+R_f)}{L_c}\mathbf{i}_{c,dq} + \frac{R_f}{L_c}\mathbf{i}_{g,dq} \\ &+ \frac{1}{3L_c}\left(T_{dq0/abc}\begin{bmatrix}-2 & 1 & 1\\ 1 & -2 & 1\\ 1 & 1 & -2\end{bmatrix}T_{dq0/abc}^{-1}\right)\mathbf{v}_{Cf,dq}\end{aligned} \tag{2.31}$$

where

$$\left(T_{dq0/abc}\begin{bmatrix}2 & -1 & -1\\ -1 & 2 & -1\\ -1 & -1 & 2\end{bmatrix}T_{dq0/abc}^{-1}\right) = \begin{bmatrix}3 & 0 & 0\\ 0 & 3 & 0\\ 0 & 0 & 0\end{bmatrix} \tag{2.32}$$

and

$$\left(T_{dq0/abc}\begin{bmatrix}-2 & 1 & 1\\ 1 & -2 & 1\\ 1 & 1 & -2\end{bmatrix}T_{dq0/abc}^{-1}\right) = \begin{bmatrix}-3 & 0 & 0\\ 0 & -3 & 0\\ 0 & 0 & 0\end{bmatrix} \tag{2.33}$$

and

$$\left(T_{dq0/abc}\frac{dT^{-1}_{dq0/abc}}{dt}\right) = \begin{bmatrix} 0 & -\omega & 0 \\ \omega & 0 & 0 \\ 0 & 0 & 0 \end{bmatrix} \tag{2.34}$$

Substituting (2.32) - (2.34) into (2.31) yields

$$\begin{bmatrix} 0 & -\omega & 0 \\ \omega & 0 & 0 \\ 0 & 0 & 0 \end{bmatrix} \mathbf{i}_{c,dq} + \frac{d\mathbf{i}_{c,dq}}{dt} = \frac{1}{3L_c}\begin{bmatrix} 3 & 0 & 0 \\ 0 & 3 & 0 \\ 0 & 0 & 0 \end{bmatrix} \mathbf{d}_{dq} v_{dc} - \frac{(R_c + R_f)}{L_c}\mathbf{i}_{c,dq} + \frac{R_f}{L_c}\mathbf{i}_{g,dq} + \frac{1}{3L_c}\begin{bmatrix} -3 & 0 & 0 \\ 0 & -3 & 0 \\ 0 & 0 & 0 \end{bmatrix} \mathbf{v}_{Cf,dq} \tag{2.35}$$

Assuming a balanced system in this work, the same process can be applied to the remainder of the derived equations and simplified to yield the final large-signal equations for the power stage such that

$$\frac{d\mathbf{i}_{c,dq}}{dt} = \frac{1}{L_c}\left(\mathbf{d}_{dq} v_{dc} - (R_c + R_f + j\omega L_c)\,\mathbf{i}_{c,dq} + R_f \mathbf{i}_{g,dq} - \mathbf{v}_{Cf,dq}\right) \tag{2.36}$$

$$\frac{d\mathbf{i}_{g,dq}}{dt} = \frac{1}{L_g}\left(\mathbf{v}_{Cf,dq} + R_f \mathbf{i}_{c,dq} - (R_g + R_f + j\omega L_g)\,\mathbf{i}_{g,dq} - \mathbf{v}_{g,dq}\right) \tag{2.37}$$

$$\frac{d\mathbf{v}_{Cf}}{dt} = \frac{1}{C_f}\left(\mathbf{i}_{c,dq} - \mathbf{i}_{g,dq} - j\omega C_f \mathbf{v}_{Cf,dq}\right) \tag{2.38}$$

$$\frac{dv_{dc}}{dt} = \frac{1}{C_{dc}}\left(\frac{V_{eq}}{R_{eq}} - \frac{v_{dc}}{R_{eq}} - d_d i_{c,d} - d_q i_{c,q}\right) \tag{2.39}$$

The resulting small-signal equations are expressed in (2.40), where ~ denotes small-signal

values and capital letters denote steady-state values at the operating point.

$$\frac{d\tilde{\mathbf{i}}_{c,dq}}{dt} = \frac{1}{L_c}\left[\tilde{\mathbf{d}}_{dq}\tilde{v}_{dc} - (R_c + R_f + j\omega L_c)\,\tilde{\mathbf{i}}_{c,dq} + R_f\tilde{\mathbf{i}}_{g,dq} - \tilde{\mathbf{v}}_{Cf,dq}\right] \tag{2.40}$$

$$\frac{d\tilde{\mathbf{i}}_{g,dq}}{dt} = \frac{1}{L_g}\left[\tilde{\mathbf{v}}_{Cf,dq} + R_f\tilde{\mathbf{i}}_{c,dq} - (R_g + R_f + j\omega L_g)\,\tilde{\mathbf{i}}_{g,dq} - \tilde{\mathbf{v}}_{g,dq}\right] \tag{2.41}$$

$$\frac{d\tilde{\mathbf{v}}_{Cf}}{dt} = \frac{1}{C_f}\left[\tilde{\mathbf{i}}_{c,dq} - \tilde{\mathbf{i}}_{g,dq} - j\omega C_f\tilde{\mathbf{v}}_{Cf,dq}\right] \tag{2.42}$$

$$\frac{d\tilde{v}_{dc}}{dt} = \frac{1}{C_{dc}}\left[\frac{V_{eq}}{R_{eq}} - \frac{\tilde{v}_{dc}}{R_{eq}} - \tilde{d}_d I_{c,d} - \tilde{d}_q I_{c,q} - \tilde{i}_{c,d} D_d - \tilde{i}_{c,q} D_q\right] \tag{2.43}$$

A state-space representation of the small-signal model is formed such that the state vector, input vector, and output vector, respectively, are

$$\tilde{\mathbf{x}} = \begin{bmatrix} \tilde{i}_{c,d} \\ \tilde{i}_{c,q} \\ \tilde{i}_{g,d} \\ \tilde{i}_{g,q} \\ \tilde{v}_{Cf,d} \\ \tilde{v}_{Cf,q} \\ \tilde{v}_{dc} \end{bmatrix}, \qquad \tilde{\mathbf{u}} = \begin{bmatrix} \tilde{v}_{g,d} \\ \tilde{v}_{g,q} \\ \tilde{d}_d \\ \tilde{d}_q \end{bmatrix}, \qquad \text{and} \qquad \tilde{\mathbf{y}} = \begin{bmatrix} \tilde{v}_{dc} \\ \tilde{i}_{g,d} \\ \tilde{i}_{g,q} \end{bmatrix}.$$

The state-space representation is expressed as

$$\begin{aligned} \dot{\tilde{\mathbf{x}}} &= \mathbf{A}\tilde{\mathbf{x}} + \mathbf{B}\tilde{\mathbf{u}} \\ \tilde{\mathbf{y}} &= \mathbf{C}\tilde{\mathbf{x}} + \mathbf{D}\tilde{\mathbf{u}} \end{aligned} \tag{2.44}$$

where the transfer function relating the inputs to the outputs of the state-space model is defined as

$$\tilde{\mathbf{y}} = \left[\mathbf{C}\left(s\mathbf{I} - \mathbf{A}\right)^{-1}\mathbf{B} + \mathbf{D}\right]\tilde{\mathbf{u}} \tag{2.45}$$

and

$$\mathbf{A} = \begin{bmatrix} -\frac{R_c+R_f}{L_c} & \omega & \frac{R_f}{L_c} & 0 & -\frac{1}{L_c} & 0 & \frac{D_d}{L_c} \\ -\omega & -\frac{R_c+R_f}{L_c} & 0 & \frac{R_f}{L_c} & 0 & -\frac{1}{L_c} & \frac{D_q}{L_c} \\ \frac{R_f}{L_g} & 0 & -\frac{R_g+R_f}{L_g} & \omega & \frac{1}{L_g} & 0 & 0 \\ 0 & \frac{R_f}{L_g} & -\omega & -\frac{R_g+R_f}{L_g} & 0 & \frac{1}{L_g} & 0 \\ \frac{1}{C_f} & 0 & -\frac{1}{C_f} & 0 & 0 & \omega & 0 \\ 0 & \frac{1}{C_f} & 0 & -\frac{1}{C_f} & -\omega & 0 & 0 \\ -\frac{D_d}{C_{dc}} & -\frac{D_q}{C_{dc}} & 0 & 0 & 0 & 0 & -\frac{1}{R_{eq}C_{dc}} \end{bmatrix} \tag{2.46}$$

$$\mathbf{B} = \begin{bmatrix} 0 & 0 & \frac{V_{dc}}{L_c} & 0 \\ 0 & 0 & 0 & \frac{V_{dc}}{L_c} \\ -\frac{1}{L_g} & 0 & 0 & 0 \\ 0 & -\frac{1}{L_g} & 0 & 0 \\ 0 & 0 & 0 & 0 \\ 0 & 0 & 0 & 0 \\ 0 & 0 & -\frac{I_{cd}}{C_{dc}} & -\frac{I_{cq}}{C_{dc}} \end{bmatrix} \tag{2.47}$$

$$\mathbf{C} = \begin{bmatrix} 0 & 0 & 0 & 0 & 0 & 0 & 1 \\ 1 & 0 & 0 & 0 & 0 & 0 & 0 \\ 0 & 1 & 0 & 0 & 0 & 0 & 0 \\ 0 & 0 & 1 & 0 & 0 & 0 & 0 \\ 0 & 0 & 0 & 1 & 0 & 0 & 0 \end{bmatrix} \tag{2.48}$$

$$\mathbf{D} = \begin{bmatrix} 0 & 0 & 0 & 0 \\ 0 & 0 & 0 & 0 \\ 0 & 0 & 0 & 0 \\ 0 & 0 & 0 & 0 \\ 0 & 0 & 0 & 0 \end{bmatrix} \tag{2.49}$$

Therefore, the resulting small-signal model of the power stage is expressed in (2.50), where the block diagram is shown in Fig. 2.10.

$$\begin{bmatrix} \tilde{v}_{dc} \\ \tilde{i}_{g,d} \\ \tilde{i}_{g,q} \end{bmatrix} = \begin{bmatrix} \mathbf{G_{Dv}} & \mathbf{G_{Dd}} \\ \mathbf{G_{iv}} & \mathbf{G_{id}} \end{bmatrix} \begin{bmatrix} \tilde{v}_{g,d} \\ \tilde{v}_{g,q} \\ \tilde{d}_d \\ \tilde{d}_q \end{bmatrix} \tag{2.50}$$

The block diagram of the power stage will be used as the main building block in Ch. 3 and Ch. 4 for the grid-tracking and grid-forming control scheme, respectively.

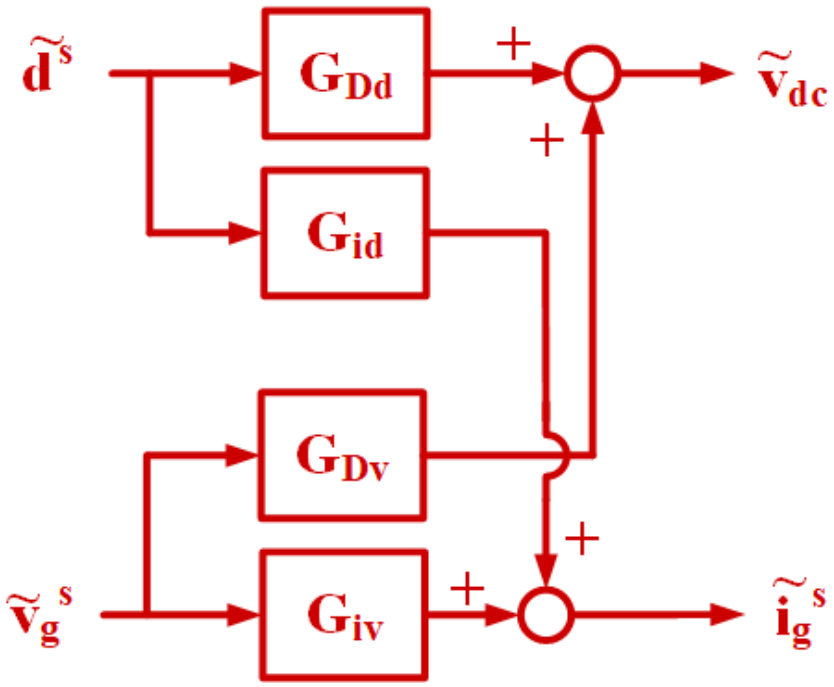

Figure 2.10: Power stage small-signal model.

Chapter 3

Grid-Tracking Control

3.1 Basics of a PLL

In this chapter, the design of a grid-tracking control scheme is detailed. The control scheme emulates a *dq* frame phase-locked-loop- (PLL-) oriented vector control and consists of a cascaded control structure with an outer voltage loop and inner current loop. The outer voltage loop regulates the active and reactive power injection of the inverter to the grid and provides the current reference to the inner current loop, which generates the duty cycles used for the switching of the converter switching network.

In order to synchronize the inverter to the grid, a PLL is used. However, the introduction of a PLL also results in two *dq* frames: that of the system, denoted by superscript s, and that of the controller, denoted by superscript c [26]. In steady-state, the two frames are aligned; however, when small-signal perturbations are introduced into the system, the two frames are offset, with angle deviation δ, as shown in Fig. 3.1. The inputs to the controller, the PCC voltage and current, are passed through a matrix $\mathbf{T}_\delta$ to convert the variables from the system *dq* frame to the controller *dq* frame. Similarly, the output of the controller, the duty cycles which drive the switching, are passed through the inverse of $\mathbf{T}_\delta$ to transform the variables back to the system frame. The transformation matrix is expressed in (3.1).

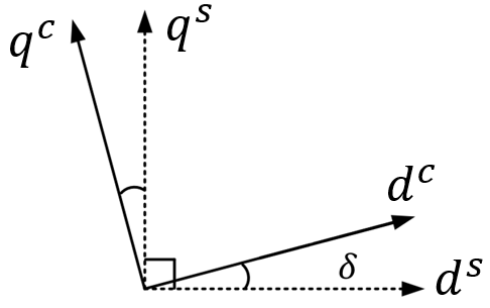

Figure 3.1: Offset between system and controller *dq* frames.

$$\mathbf{T}_\delta = \begin{bmatrix} \cos(\delta) & \sin(\delta) \\ -\sin(\delta) & \cos(\delta) \end{bmatrix} \tag{3.1}$$

where the input and output variables of the controller frame are passed from and to the system frame, respectively, such that

$$\mathbf{v}_g^c = \mathbf{T}_\delta \mathbf{v}_g^s, \qquad \mathbf{i}_g^c = \mathbf{T}_\delta \mathbf{i}_g^s, \qquad \mathbf{d}^s = \mathbf{T}_\delta^{-1} \mathbf{d}^c \tag{3.2}$$

The remainder of this chapter will discuss the design of the cascaded control structure and effects of the parameters on the control loops. Additionally, the derivation process of the terminal ac impedance of the inverter will be shown, from which the stability of the system will be analyzed in Ch. 5.

3.2 Design of the Grid-Tracking Control

3.2.1 Phase-Locked Loop

As was mentioned in the previous section, the inverter must maintain synchronization with the grid at the point of common coupling (PCC). The conventional method of maintaining this synchronization is through the use of a PLL, specifically a synchronous-reference-frame (SRF) PLL, as shown in Fig. 3.2 [34, 62], where a proportional-integrator (PI) controller is used in the LF due to its rapid response to system dynamics. The proportional component will mitigate the high-frequency system response while the integral component will manage the steady-state error and work to minimize it [63]. The transofrmation matrix is

$$\mathbf{T_{dq}} = \sqrt{\frac{\mathbf{2}}{\mathbf{3}}} \begin{bmatrix} \cos(\delta) & \cos(\delta - \frac{2\pi}{3}) & \cos(\delta + \frac{2\pi}{3}) \\ -\sin(\delta) & -\sin(\delta - \frac{2\pi}{3}) & -\sin(\delta + \frac{2\pi}{3}) \end{bmatrix} \tag{3.3}$$

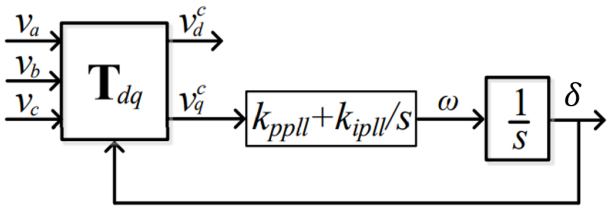

Figure 3.2: SRF PLL.

The SRF PLL is ideal in obtaining the phase and frequency information under a balanced grid condition [64]. In order to attenuate the influence of the synchronization scheme due to grid dynamics and reject the harmonics due the SRF PLL, the bandwidth of the SRF PLL is designed to be low. The small-signal model of the SRF PLL is shown in Fig. 3.3 [65], from which the SRF PLL can be designed.

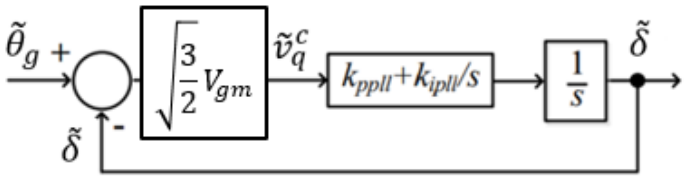

Figure 3.3: Small-signal model of SRF PLL.

The loop gain of the PLL structure is

$$T_{pll} = \frac{1}{s}\left(k_{ppll} + \frac{k_{ipll}}{s}\right)\sqrt{\frac{3}{2}}V_{gm} \tag{3.4}$$

where k_{ppll} is the proportional gain of the PI regulator, k_{ipll} is the integral gain of the PI regulator, and V_{gm} is the amplitude of the ac bus voltage at the PCC, which results in the PD being equivalent to the line-to-line voltage. The use of the PI results in a second-order closed loop transfer function [62, 66] such that

$$H_{pll} = \frac{T_{pll}}{1 + T_{pll}} \tag{3.5}$$

$$= \frac{\sqrt{\frac{3}{2}} V_{gm} k_{ppll} (\tau s + 1)}{s + \sqrt{\frac{3}{2}} V_{gm} k_{ppll} (\tau s + 1)} \tag{3.6}$$

$$= \frac{\sqrt{\frac{3}{2}} V_{gm} k_{ppll} s + \frac{\sqrt{\frac{3}{2}} V_{gm} k_{ppll}}{\tau}}{s^2 + \sqrt{\frac{3}{2}} V_{gm} k_{ppll} s + \frac{\sqrt{\frac{3}{2}} V_{gm} k_{ppll}}{\tau}} \tag{3.7}$$

where $\tau = \frac{k_{ppll}}{k_{ipll}}$. Eq. (3.5) takes on the general form of a second-order transfer function

$$H_{2nd-order} = \frac{2\zeta\omega_c s + \omega_c^2}{s^2 + 2\zeta\omega_c s + \omega_c^2} \tag{3.8}$$

where ζ is the damping coefficient and ω_c is the corner frequency, such that

$$\zeta = \frac{1}{2}\sqrt{\sqrt{\frac{3}{2}} V_{gm} k_{ppll} \tau} \qquad \text{and} \qquad \omega_c = \sqrt{\frac{\sqrt{\frac{3}{2}} V_{gm} k_{ppll}}{\tau}} \tag{3.9}$$

The PI gains for the SRF PLL are shown in Table 3.1, which results in a bandwidth of 5.5 Hz for the synchronization loop in the *dq* frame PLL-oriented vector control scheme, as shown in Fig. 3.4.

Table 3.1: SRF PLL PI gains

k_{ppll}	0.1
k_{ipll}	1

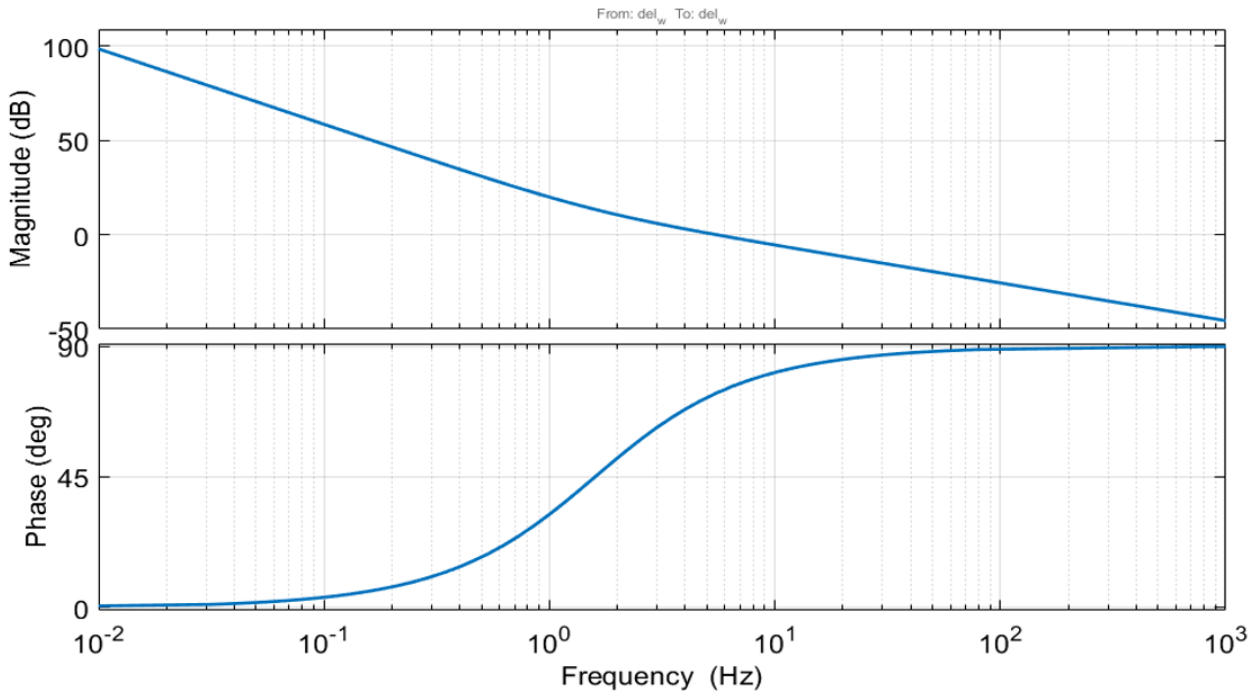

Figure 3.4: Synchronization loop gain of the SRF PLL.

3.2.1.1 Influence of the PLL

Small-signal perturbations of the grid voltage have a cascading effect on the rest of the control scheme as the grid voltage is used in the synchronization of the inverter to the grid as well as the transformation from the system to controller dq frame [67]. In steady-state, the angle difference between the two dq frames is 0 and, thus, the variables in both frames are equivalent, such that

$$\mathbf{V}_g^c = \mathbf{V}_g^s, \qquad \mathbf{I}_g^c = \mathbf{I}_g^s, \qquad \mathbf{D}^s = \mathbf{D}^c. \tag{3.10}$$

Eq. (3.10) is rewritten using the rotation matrix $\mathbf{T}_\delta$ such that

$$\mathbf{V}_g^c = \begin{bmatrix} \cos(0) & \sin(0) \\ -\sin(0) & \cos(0) \end{bmatrix} \mathbf{V}_g^s \tag{3.11}$$

$$\mathbf{I}_g^c = \begin{bmatrix} \cos(0) & \sin(0) \\ -\sin(0) & \cos(0) \end{bmatrix} \mathbf{I}_g^s \tag{3.12}$$

$$\mathbf{D}^s = \begin{bmatrix} \cos(0) & -\sin(0) \\ \sin(0) & \cos(0) \end{bmatrix} \mathbf{D}^c \tag{3.13}$$

To analyze the effect of the PLL on the small-signal model, a small-signal perturbation is added to (3.11), yielding

$$\begin{bmatrix} V_{gd}^c + \tilde{v}_{gd}^c \\ V_{gq}^c + \tilde{v}_{gq}^c \end{bmatrix} = \begin{bmatrix} \cos(0+\tilde{\delta}) & \sin(0+\tilde{\delta}) \\ -\sin(0+\tilde{\delta}) & \cos(0+\tilde{\delta}) \end{bmatrix} \begin{bmatrix} V_{gd}^s + \tilde{v}_{gd}^s \\ V_{gq}^s + \tilde{v}_{gq}^s \end{bmatrix} \tag{3.14}$$

$$\begin{bmatrix} I_{gd}^c + \tilde{i}_{gd}^c \\ I_{gq}^c + \tilde{i}_{gq}^c \end{bmatrix} = \begin{bmatrix} \cos(0+\tilde{\delta}) & \sin(0+\tilde{\delta}) \\ -\sin(0+\tilde{\delta}) & \cos(0+\tilde{\delta}) \end{bmatrix} \begin{bmatrix} I_{gd}^s + \tilde{i}_{gd}^s \\ I_{gq}^s + \tilde{i}_{gq}^s \end{bmatrix} \tag{3.15}$$

$$\begin{bmatrix} D_d^s + \tilde{d}_d^s \\ D_q^s + \tilde{d}_q^s \end{bmatrix} = \begin{bmatrix} \cos(0+\tilde{\delta}) & -\sin(0+\tilde{\delta}) \\ \sin(0+\tilde{\delta}) & \cos(0+\tilde{\delta}) \end{bmatrix} \begin{bmatrix} D_d^c + \tilde{d}_d^c \\ D_q^c + \tilde{d}_q^c \end{bmatrix} \tag{3.16}$$

to which the small-angle approximation may be applied to obtain

$$\begin{bmatrix} V_{gd}^c + \tilde{v}_{gd}^c \\ V_{gq}^c + \tilde{v}_{gq}^c \end{bmatrix} \approx \begin{bmatrix} 1 & \tilde{\delta} \\ -\tilde{\delta} & 1 \end{bmatrix} \begin{bmatrix} V_{gd}^s + \tilde{v}_{gd}^s \\ V_{gq}^s + \tilde{v}_{gq}^s \end{bmatrix} \tag{3.17}$$

$$\begin{bmatrix} I_{gd}^c + \tilde{i}_{gd}^c \\ I_{gq}^c + \tilde{i}_{gq}^c \end{bmatrix} \approx \begin{bmatrix} 1 & \tilde{\delta} \\ -\tilde{\delta} & 1 \end{bmatrix} \begin{bmatrix} I_{gd}^s + \tilde{i}_{gd}^s \\ I_{gq}^s + \tilde{i}_{gq}^s \end{bmatrix} \tag{3.18}$$

$$\begin{bmatrix} D_d^s + \tilde{d}_d^s \\ D_q^s + \tilde{d}_q^s \end{bmatrix} \approx \begin{bmatrix} 1 & -\tilde{\delta} \\ \tilde{\delta} & 1 \end{bmatrix} \begin{bmatrix} D_d^c + \tilde{d}_d^c \\ D_q^c + \tilde{d}_q^c \end{bmatrix} \tag{3.19}$$

Recalling that the steady-state variables are equivalent, (3.17) is simplified to

$$\begin{bmatrix} \tilde{v}_{gd}^{c} \\ \tilde{v}_{gq}^{c} \end{bmatrix} \approx \begin{bmatrix} \tilde{v}_{gd}^{s} + V_{g,q}^{s}\tilde{\delta} \\ \tilde{v}_{gq}^{s} - V_{g,d}^{s}\tilde{\delta} \end{bmatrix} \tag{3.20}$$

$$\begin{bmatrix} \tilde{i}_{gd}^{c} \\ \tilde{i}_{gq}^{c} \end{bmatrix} \approx \begin{bmatrix} \tilde{i}_{gd}^{s} + I_{g,q}^{s}\tilde{\delta} \\ \tilde{i}_{gq}^{s} - I_{g,d}^{s}\tilde{\delta} \end{bmatrix} \tag{3.21}$$

$$\begin{bmatrix} \tilde{d}_{d}^{s} \\ \tilde{d}_{q}^{s} \end{bmatrix} \approx \begin{bmatrix} \tilde{d}_{d}^{c} - D_{q}^{c}\tilde{\delta} \\ \tilde{d}_{q}^{c} + D_{d}^{c}\tilde{\delta} \end{bmatrix} \tag{3.22}$$

In (3.20) - (3.22), $\tilde{\delta}$ is a function of the PLL structure. Consider the average model of the PLL from Fig. 3.2, as shown in Fig. 3.5. $\bar{\delta}$ is then expressed as

$$\bar{\delta} = \frac{1}{s} \cdot tf_{pll} \cdot \bar{v}_{gq}^{c} \tag{3.23}$$

where $tf_{pll} = \left(k_{ppll} + \frac{k_{ipll}}{s}\right)$ and from which $\tilde{\delta}$ is

$$\tilde{\delta} = \frac{1}{s} \cdot tf_{pll} \cdot \tilde{v}_{gq}^{c} \tag{3.24}$$

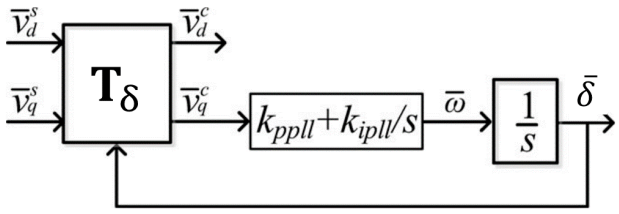

Figure 3.5: Average model of the SRF PLL.

Substituting (3.24) into (3.20) and solving for the relationship between the small-signal q-channel system voltage, $\tilde{v}_{gq}^{s}$, and the PLL angle yields

$$\tilde{\delta} = \frac{tf_{pll}}{s + V_{gd}^{s} tf_{pll}} \tilde{v}_{gq}^{s} \tag{3.25}$$

To further simplify the expression, G_{PLL} is defined as

$$G_{PLL} = \frac{tf_{pll}}{s + V_{gd}^{s} tf_{pll}} \tag{3.26}$$

such that (3.25) is redefined

$$\tilde{\delta} = G_{PLL} \tilde{v}_{gq}^{s} \tag{3.27}$$

The expression for the PLL output angle from (3.27) is substituted into (3.20) - (3.22) to obtain (3.28) - (3.30), which take into consideration the effect of the synchronization scheme on the input and output variables of the controller [26, 29].

$$\begin{bmatrix} \tilde{v}_{gd}^{c} \\ \tilde{v}_{gq}^{c} \end{bmatrix} \approx \mathbf{G_{PLL}^{v}} \begin{bmatrix} \tilde{v}_{gd}^{s} \\ \tilde{v}_{gq}^{s} \end{bmatrix} \tag{3.28}$$

$$\begin{bmatrix} \tilde{i}_{gd}^{c} \\ \tilde{i}_{gq}^{c} \end{bmatrix} \approx \mathbf{G_{PLL}^{i}} \begin{bmatrix} \tilde{v}_{gd}^{s} \\ \tilde{v}_{gq}^{s} \end{bmatrix} + \begin{bmatrix} \tilde{i}_{gd}^{s} \\ \tilde{i}_{gq}^{s} \end{bmatrix} \tag{3.29}$$

$$\begin{bmatrix} \tilde{d}_{d}^{s} \\ \tilde{d}_{q}^{s} \end{bmatrix} \approx \mathbf{G_{PLL}^{d}} \begin{bmatrix} \tilde{v}_{gd}^{s} \\ \tilde{v}_{gq}^{s} \end{bmatrix} + \begin{bmatrix} \tilde{d}_{d}^{c} \\ \tilde{d}_{q}^{c} \end{bmatrix} \tag{3.30}$$

where

$$\mathbf{G_{PLL}^{v}} = \begin{bmatrix} 1 & V_{gq}^{s} G_{PLL} \\ 0 & 1 - V_{gd}^{s} G_{PLL} \end{bmatrix}, \quad \mathbf{G_{PLL}^{i}} = \begin{bmatrix} 0 & I_{gq}^{s} G_{PLL} \\ 0 & -I_{gd}^{s} G_{PLL} \end{bmatrix}, \quad \text{and} \quad \mathbf{G_{PLL}^{d}} = \begin{bmatrix} 0 & D_{q}^{c} G_{PLL} \\ 0 & -D_{d}^{c} G_{PLL} \end{bmatrix}.$$

The influence of the PLL can now be incorporated into the small-signal diagram, as shown in Fig. 3.6 in blue. As can be seen, the perturbation of the system voltage, $\tilde{v}_{g}^{s}$ impacts the

current and voltage inputs to the controller as well as the duty cycles from the controller.

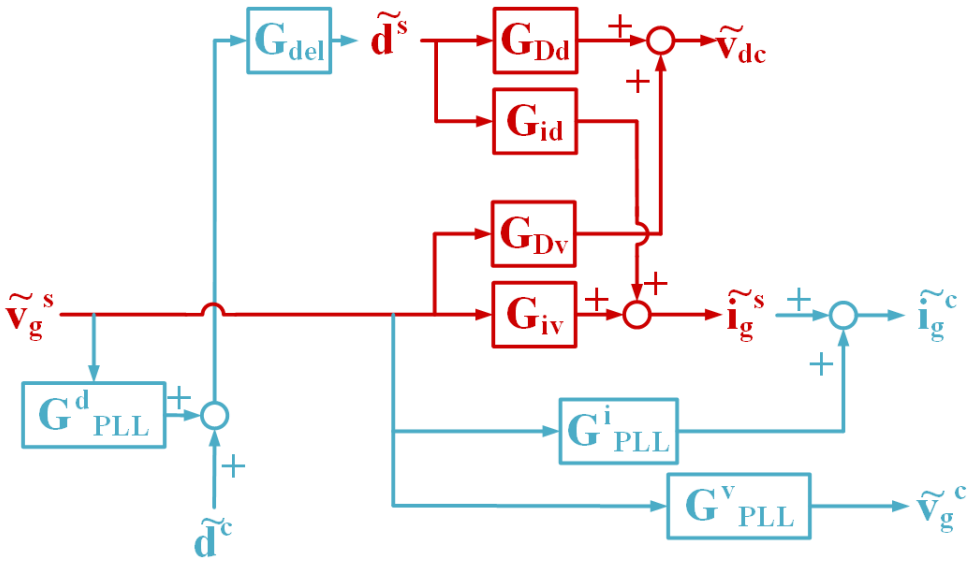

Figure 3.6: Influence of the PLL in the small-signal model.

3.2.2 AC Current Loop

In 3.2.1, it is mentioned that the *dq* frame PLL-oriented vector control comprises of a cascaded control structure, in which the innermost loop generates the duty cycle reference for the switching by regulating the measured current to a reference point, which is generated by the outer loop and will be discussed in the next section.

The current control loop can be designed for implementation in the stationary or synchronous rotating frame. For a control loop operated in the stationary frame, there are various methods of generating the reference to the switching network, as presented in [68–71]. However, this work focuses on the implementation of the controller in the synchronous rotating frame.

The ac current loop comprises a PI regulator on the *d*- and *q*-channels, which serves to regulate the deviation of the measured current passed to the controller and the generated

current reference from the outer voltage loop. Additionally, due to the coupling terms introduced by the reactive electrical components, as discussed in Chapter 2, it is necessary to decouple these dynamics; specifically, the cross-coupling terms of the inductors of the LCL filter are mitigated in the ac current loop in the feedforward term, as in [72]. The resulting inner ac current loop is shown in Fig. 3.7. In this manner, the two channels can be used to independently control the active and reactive power of the inverter, as will be discussed in the next subsection.

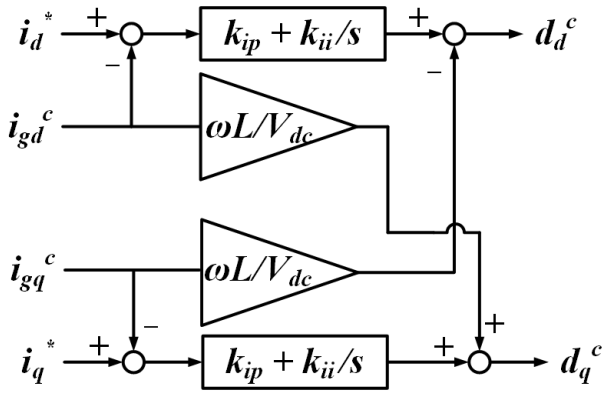

Figure 3.7: Ac current controller with decoupling.

The current control loop bandwidth is designed based on the values chosen of the PI gains. However, due to the cascaded control structure, it is necessary to ensure the mitigation of the dynamic interactions between each loop. As such, the ac current loop is designed to have the highest bandwidth within the control structure and the outer loops are designed for lower bandwidths. In this manner, the generated references from the output loops are seen as static values from the perspective of the inner loop. In this work, the ac current loop is designed for a bandwidth of 300 Hz, one-tenth of the switching frequency. The PI gains for the current control loop are shown in Table 3.2. From Fig. 3.7, the expressions for the

Table 3.2: Grid-tracking Ac Current Loop PI gains

k_{ip}	0.0012
k_{ii}	0.32

duty cycle reference in the controller frame, $\mathbf{d^c_{dq}}$, are

$$d_d^c = \left(k_{ip} + \frac{k_{ii}}{s}\right)\left(i_d^* - i_{gd}^c\right) - \frac{\omega L}{V_{dc}} i_{gq}^c \tag{3.31}$$

$$d_q^c = \left(k_{ip} + \frac{k_{ii}}{s}\right)\left(i_q^* - i_{gq}^c\right) + \frac{\omega L}{V_{dc}} i_{gd}^c \tag{3.32}$$

where ω is the frequency of the grid with the deviation due to synchronization under the influence of grid dynamics, L is $L_c + L_g$ from the LCL filter from Chapter 2, and V_{dc} is the steady-state dc-link voltage across the dc-bus capacitor. Reformatting (3.31) and (3.32) yields

$$\begin{bmatrix} d_d^c \\ d_q^c \end{bmatrix} = \begin{bmatrix} k_{ip} + \frac{k_{ii}}{s} & 0 \\ 0 & k_{ip} + \frac{k_{ii}}{s} \end{bmatrix} \begin{bmatrix} i_d^* - i_{gd}^c \\ i_q^* - i_{gq}^c \end{bmatrix} + \begin{bmatrix} 0 & -\frac{\omega L}{V_{dc}} \\ \frac{\omega L}{V_{dc}} & 0 \end{bmatrix} \begin{bmatrix} i_{gd}^c \\ i_{gq}^c \end{bmatrix} \tag{3.33}$$

from which the small-signal expression is

$$\begin{bmatrix} \tilde{d}_d^c \\ \tilde{d}_q^c \end{bmatrix} = \mathbf{G_{ci}} \begin{bmatrix} \tilde{i}_d^* - \tilde{i}_{gd}^c \\ \tilde{i}_q^* - \tilde{i}_{gq}^c \end{bmatrix} + \mathbf{G_{dei}} \begin{bmatrix} \tilde{i}_{gd}^c \\ \tilde{i}_{gq}^c \end{bmatrix} \tag{3.34}$$

where

$$\mathbf{G_{ci}} = \begin{bmatrix} k_{ip} + \frac{k_{ii}}{s} & 0 \\ 0 & k_{ip} + \frac{k_{ii}}{s} \end{bmatrix} \quad \text{and} \quad \mathbf{G_{dei}} = \begin{bmatrix} 0 & -\frac{\omega L}{V_{dc}} \\ \frac{\omega L}{V_{dc}} & 0 \end{bmatrix}.$$

The expression for the small-signal duty cycle references are incorporated in the small-signal diagram from Fig. 3.6 to obtain Fig. 3.8, where the ac current loop is in black. Evidently, the influence of the PLL propagates through the control structure as the controller's only input, at this point, is the transformed current measurement from the system to controller

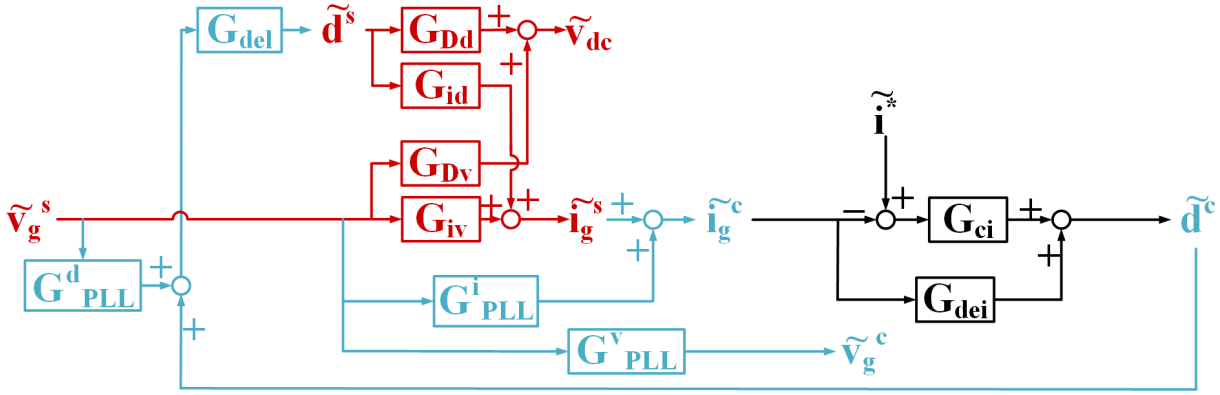

Figure 3.8: Small-signal model with ac current loop for grid-tracking control.

dq frame using the angle obtained from the PLL.

From Fig. 3.8, the ac current loop gain is derived such that

$$\frac{\tilde{\mathbf{i}}_g^c}{\left(\tilde{\mathbf{i}}^* - \tilde{\mathbf{i}}_g^c\right)} = \left(\mathbf{I} - \mathbf{G_{id}}\mathbf{G_{del}}\mathbf{G_{dei}}\right)^{-1}\left(\mathbf{G_{id}}\mathbf{G_{del}}\mathbf{G_{ci}}\right) \tag{3.35}$$

Fig. 3.9 shows the Bode plot of the ac current loop gain transfer function, in which it is shown that the bandwidth of the ac current loop is designed to be 293 Hz, which is a tenth of the switching frequency of 3kHz. In this manner, the dynamics of the inner ac current loop and the switching will be decoupled.

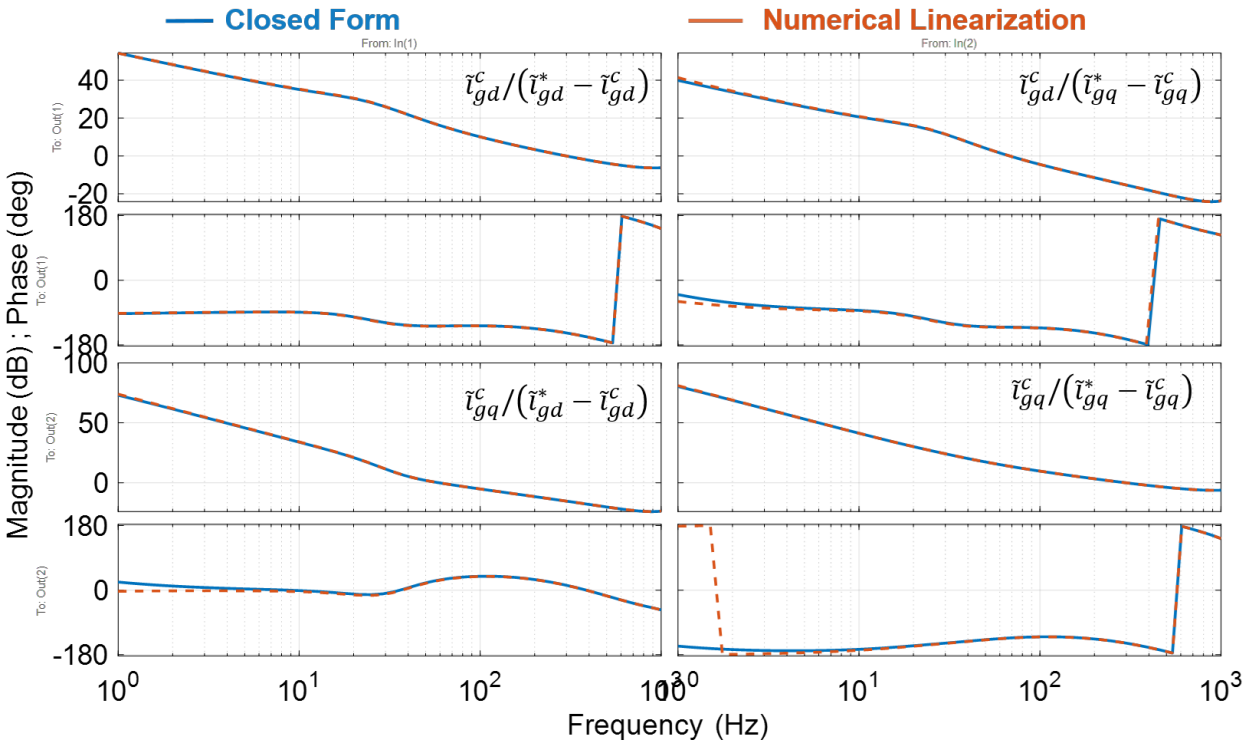

Figure 3.9: Bode plot of ac current loop gain for grid-tracking control.

3.2.3 DC Voltage Loop

The regulation of the dc bus voltage is important in the control and operation of three-phase power converters [73]. The PV array inherently fluctuates the output active power due to environmental conditions and, as a result, the dc bus voltage is effected and will overshoot, undershoot, or sag. The fluctuations in the dc bus voltage will then propagate to the system, thus resulting in reduced efficiency or, worse, an unstable operating condition [74, 75].

The reference for the inner ac current loop is generated by an outer voltage loop in the cascaded control structure. In the previous section, a decoupling term is introduced in the ac current loop in order to decouple the dynamics of the inductor currents in the dq frame. By decoupling the d- and q-channels of the rotating frame, it is possible to independently

control the two channels and, subsequently, the active and reactive power. In the power invariant transformation to the dq frame, the active and reactive power are defined as

$$P = v_{gd}^{c} i_{gd}^{c} + v_{gq}^{c} i_{gq}^{c} \tag{3.36}$$

$$Q = -v_{gd}^{c} i_{gq}^{c} + v_{gq}^{c} i_{gd}^{c} \tag{3.37}$$

Conventionally, v_{gq} is driven to zero to align the d-channel voltage, v_{gd}, to the a-phase voltage, v_{ga}, in the stationary frame. Subsequently, this action also enables the independent control of the active and reactive power such that

$$P = v_{gd}^{c} i_{gd}^{c} \tag{3.38}$$

$$Q = -v_{gd}^{c} i_{gq}^{c}. \tag{3.39}$$

As a result, the q-channel current is used to control the reactive power while the d-channel current is used to control the active power.

In Chapter 2, the relationship between the dc bus voltage and the output active power of the PV array is discussed. In this manner, it is clear that controlling the dc bus voltage leads to the regulation of the active power injection into the grid. Since the d-channel current is used to control the active power injection, according to (3.38), then the d-channel current reference, i_d^*, will stem from the deviation of the dc bus voltage from some dc set point, which is determined by the desired amount of active power. A PI regulator can be used to regulate the dc bus voltage to generate the i_d^*, as shown in Fig. 3.10, from which the expression i_d^* is

$$i_d^* = \left(k_{dcp} + \frac{k_{dci}}{s} \right) (v_{dc}^* - v_{dc}) \tag{3.40}$$

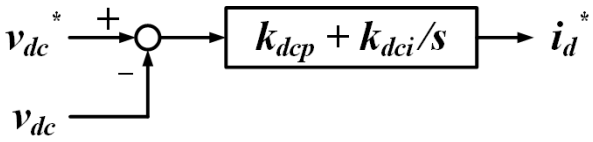

Figure 3.10: Dc voltage controller.

Taking into consideration that the q-channel current reference is 0 for the inverter under unity power factor mode of operation, then the small-signal expression of (3.40) is (3.41)

$$\begin{bmatrix} \tilde{i}_d^* \\ \tilde{i}_q^* \end{bmatrix} = \mathbf{G_{cvd}} \left(\tilde{v}_{dc}^* - \tilde{v}_{dc} \right) \tag{3.41}$$

where

$$\mathbf{G_{cvd}} = \begin{bmatrix} k_{dcp} + \frac{k_{dci}}{s} \\ 0 \end{bmatrix}.$$

Incorporating the dc voltage loop control in the small-signal model of the system under consideration results in Fig. 3.11, where the dc voltage loop control is incorporated into the control scheme in black.

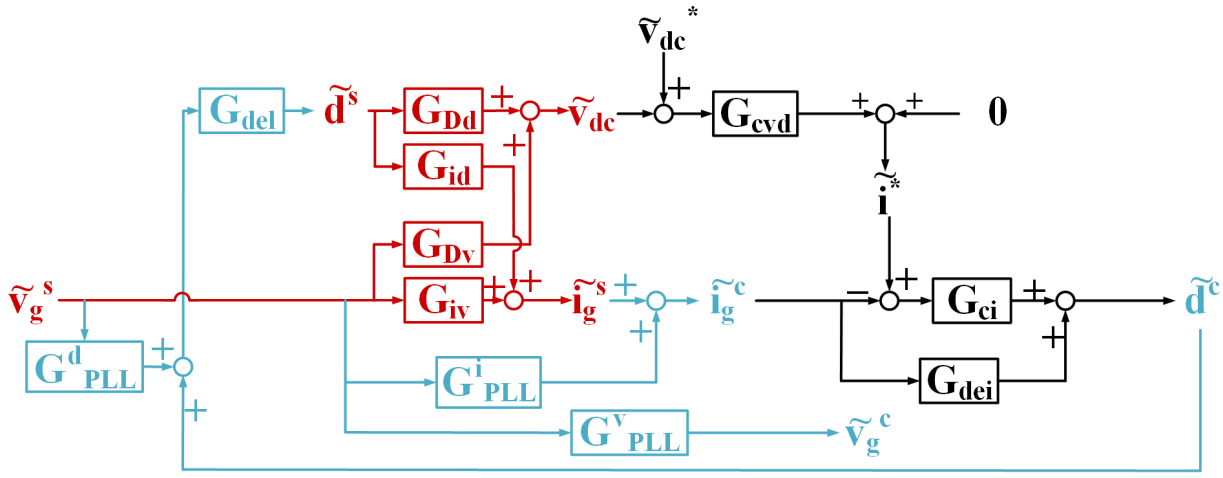

Figure 3.11: Small-signal model with dc voltage loop for grid-tracking control.

From Fig. 3.11, the expression of the dc voltage loop gain is expressed in (3.42). The bandwidth of the dc voltage loop is designed to be one-tenth of the ac current loop bandwidth in order to decouple the dynamics of the cascaded controller. In this manner, the reference generated by the outer dc voltage loop is seen as a static value by the faster inner ac current loop.

$$\frac{\tilde{v}_{dc}^{*}}{(\tilde{v}_{dc}^{*} - \tilde{v}_{dc})} = \mathbf{G_{Dd}}\left(\left(\mathbf{I} - \mathbf{G_{del}}\left(\mathbf{G_{dei}} - \mathbf{G_{ci}}\right)\mathbf{G_{id}}\right)^{-\mathbf{1}}\mathbf{G_{del}}\mathbf{G_{ci}}\mathbf{G_{cvd}}\right) \tag{3.42}$$

Using the PI gains from Table 3.3, a bandwidth of 22 Hz for the dc voltage loop is achieved, which is shown in the Bode plot for the dc voltage loop gain in Fig. 3.12, which also shows the comparison of the numerical linearization and closed form transfer function of the dc voltage loop, where the two match. At this bandwidth, a tenth of the inner ac current loop, the dynamics between the two control loops are decoupled.

Table 3.3: Grid-tracking Dc Voltage Loop PI gains

k_{dcp}	-3
k_{dci}	-30

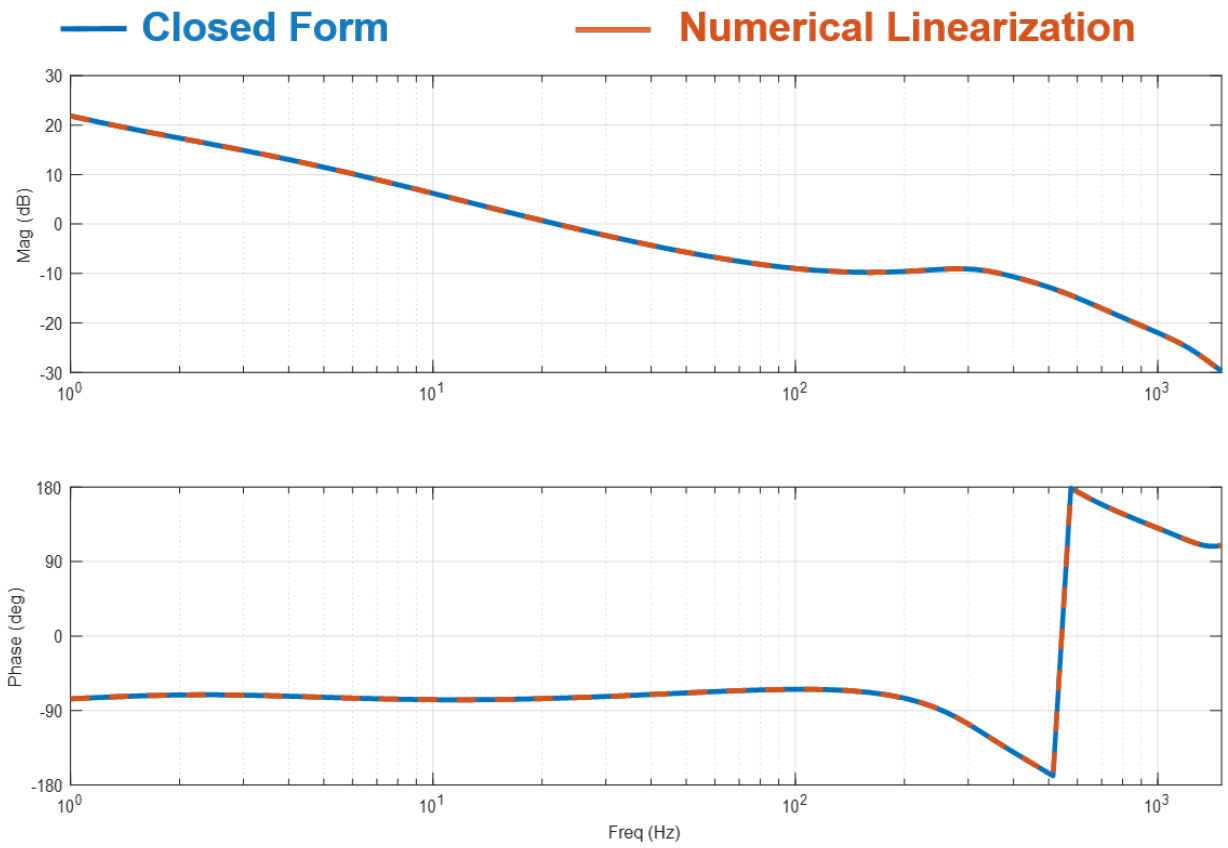

Figure 3.12: Bode plot of dc voltage loop gain for grid-tracking control.

3.3 Reactive Power Control Modes

Due to the increased penetration of renewable energy sources (RES), it is no longer feasible to simply install grid-supporting equipment in the distribution network to compensate for the rapid fluctuations of power injection from these resources [76]. However, due to the flexible control design for inverters, it is possible to implement a reactive power control scheme in which the inverter can be used for both active power injection based on the current load of the system and for reactive power injection based on the voltage at the connection; in this way, the overall cost of maintaining the grid stability can be reduced [76–78]. Additionally, this form of reactive power compensation is far more flexible and rapid compared to the

traditional reactor banks and synchronous machines.

To further compensate for the increased penetration of RES, these sources are now required to have reactive power capability and voltage/power control functionalities, as per the IEEE 1547-2018 Standard [33]. This work considers three modes of operation: 1) unity power factor, which is considered in the previous section, 2) constant reactive power, and 3) voltage-reactive power. According to [33], the inverter must be able to operate in each mode one at a time. Additionally, the standard differentiates between two categories of sources: 1) Category A, in which the RES is applied in an area of the distribution system where the penetration level is low and, thus, is not subject to frequent large variations, and 2) Category B, in which the RES is applied in an area of the distribution system where the penetration level is higher or is subject to frequent large variations. Since Category B is more restrictive in terms of requirements for the design of the controller, the control scheme in this work is designed in accordance to Category B requirements for reactive power control.

3.3.1 Fixed Reactive Power Mode

In the fixed reactive power control mode, the inverter provides a fixed amount of reactive power injection to the grid according to a set point determined by the system operators. In this manner, the PV inverter operates similar to a fixed reactor bank, which, when switched on, provides a fixed amount of reactive power based on the reactive power capabaility designed for the bank. However, the PV inverter will continue to also inject a set amount of active power based on the current load of the system.

From 3.2.3, it is shown that the reactive power injection can be controlled by regulating the q-channel current in the controller. Therefore, the reactive power controller is designed such that a q-channel current reference is generated for the inner current control loop. In this work, a PI regulator is used to generate the reference from the deviation of the measured

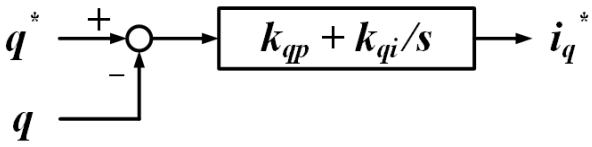

Figure 3.13: Fixed reactive power control.

reactive power at the PCC to the set point, as shown in Fig. 3.13, where the PI gains are shown in Table 3.4. From this figure, the expression for the q-channel current reference, i_q^*, is

$$i_q^* = \left(k_{qp} + \frac{k_{qi}}{s}\right)(q^* - q) \tag{3.43}$$

Recall that the reactive power in the rotating frame is expressed in terms of the measured

Table 3.4: Grid-tracking Reactive Power Loop PI Gains

k_{qp}	-2 $\times 10^{-4}$
k_{qi}	-0.8

voltage and currents in the dq frame, as shown in (3.39). Although the controller drives v_{gq} to zero in steady state, perturbations of the voltage will affect both channels when deriving the small-signal model of the controller. Therefore, (3.44) is expressed as

$$i_q^* = \left(k_{qp} + \frac{k_{qi}}{s}\right)\left(q^* + v_{gd}^c i_{gq}^c - v_{gq}^c i_{gd}^c\right) \tag{3.44}$$

The derivation of the small-signal expression of (3.44) is done as follows:

$$\tilde{i}_q^* = G_{qs}\left(\tilde{q}^* + \left(V_{gd}^c + \tilde{v}_g d^c\right)\left(I_{gq}^c + \tilde{i}_{gq}^c\right) - \left(V_{gq}^c + \tilde{v}_g q^c\right)\left(I_{gd}^c + \tilde{i}_{gd}^c\right)\right) \tag{3.45}$$

where

$$G_{qs} = k_{qp} + \frac{k_{qi}}{s}.$$

Considering only small-signal values and ignoring high-order components yields

$$\tilde{i}_q^* = G_{qs}\left(0 + V_{gd}^c\tilde{i}_{gq}^c + I_{gq}^c\tilde{v}_{gd}^c - V_{gq}^c\tilde{i}_{gd}^c - I_{gd}^c\tilde{v}_{gq}^c\right) \tag{3.46}$$

$$\Rightarrow \tilde{i}_q^* = \begin{bmatrix} -G_{qs}V_{gq}^c & G_{qs}V_{gd}^c \end{bmatrix} \begin{bmatrix} \tilde{i}_{gd}^c \\ \tilde{i}_{gq}^c \end{bmatrix} + \begin{bmatrix} G_{qs}I_{gq}^c & -G_{qs}I_{gd}^c \end{bmatrix} \begin{bmatrix} \tilde{v}_{gd}^c \\ \tilde{v}_{gq}^c \end{bmatrix} \tag{3.47}$$

Combining the expression for $\tilde{i}_d^*$ from (3.41) with the expression for $\tilde{i}_q^*$ just obtained, then

$$\begin{bmatrix} \tilde{i}_d^* \\ \tilde{i}_q^* \end{bmatrix} = \mathbf{G_{cvd}}\left(\tilde{v}_{dc}^* - \tilde{v}_{dc}\right) + \mathbf{G_{qi}} \begin{bmatrix} \tilde{i}_{gd}^c \\ \tilde{i}_{gq}^c \end{bmatrix} + \mathbf{G_{cvq}} \begin{bmatrix} \tilde{v}_{gd}^c \\ \tilde{v}_{gq}^c \end{bmatrix} \tag{3.48}$$

where

$$\mathbf{G_{cvd}} = \begin{bmatrix} k_{dcp} + \frac{k_{dci}}{s} \\ 0 \end{bmatrix}, \quad \mathbf{G_{qi}} = \begin{bmatrix} 0 & 0 \\ -G_{qs}V_{gq}^c & G_{qs}V_{gd}^c \end{bmatrix}, \quad \text{and} \quad \mathbf{G_{cvq}} \begin{bmatrix} 0 & 0 \\ G_{qs}I_{gq}^c & -G_{qs}I_{gd}^c \end{bmatrix}.$$

The generation of the current reference is incorporated in the controller, in black, in the small-signal model of the system, as shown in Fig. 3.14. In this manner, all control loops are closed and various transfer functions can be derived from the complete small-signal model.

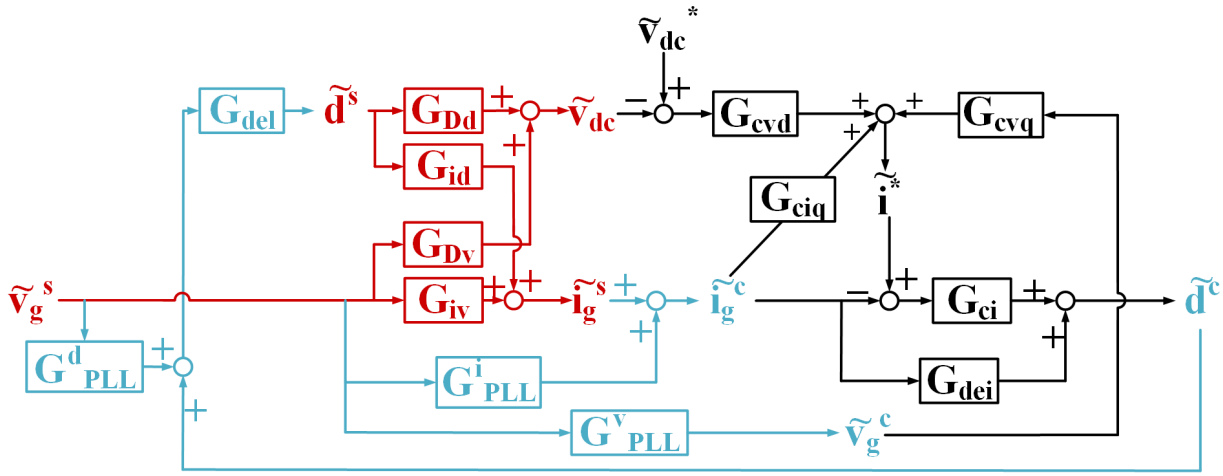

Figure 3.14: Small-signal model with fixed reactive power control for grid-tracking control.

3.3.2 Voltage-Reactive Power Mode

As discussed at the beginning of this section, the IEEE 1547-2018 standard requires the incorporation of a voltage-reactive mode, also known as reactive power droop control or volt-var. In this mode of operation, the inverter dynamically regulates the ac bus voltage through the injection of reactive power.

In this mode of operation, the controller takes the measured voltage at the PCC transformed to the controller dq frame as an input. This voltage is then passed through a droop function to generate a reactive power reference, which is then passed through a PI controller to obtain the q-channel current reference for the inner ac current loop. The droop function is defined by a piecewise function, in which each segment is partitioned by predetermined voltage values. In each segment, the value of reactive power injection is dependent which range of voltage set points the measured voltage falls under. The volt-var droop curve is shown in Fig. 3.15.

The segment defined by set points $V1$ and $V2$ is the region of dynamic capacitive reactive

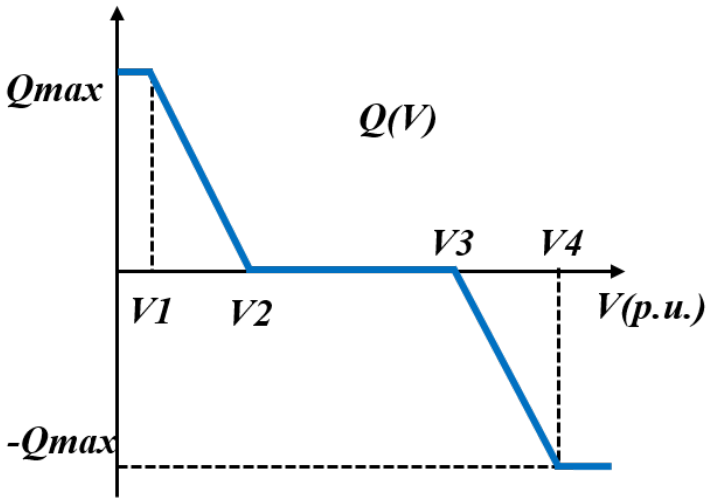

Figure 3.15: Volt-var droop curve.

power injection. Similarly, the segment defined by set points $V3$ and $V4$ is the region of dynamic inductive reactive power injection. Alternatively, if the measured voltage falls in the range determined by $V2$ and $V3$, no reactive power is injected from the inverter to the system; this is known as the deadband of the droop curve. The system operators decide that, within this band, no reactive power is needed to regulate the ac bus voltage as it falls within a predetermined acceptable voltage range. Lastly, there exists two segments at which the maximum reactive power capability of the inverter is reached. As a result, the inverter can no longer dynamically regulate the ac bus voltage and, instead, acts as a reactor bank from the viewpoint of the system. The injection capability of the inverter under Category B of the IEEE 1547-2018 standard is 44% of the nameplate apparent power rating of the inverter [33]. In this work, $V1 = 0.975$ p.u., $V2 = 1.0$ p.u., $V3 = 1.025$ p.u., and $V4 = 1.05$ p.u. and $Q_{max} = 112.5$ kvar.

The droop function is defined by [79]

$$q^* = \begin{cases} Q_{max} & K = \frac{\Delta Q}{\Delta V} & V < V1 \\ \left(\frac{Q_{max}}{V1-V2}\right)\left(v_{gd}^c - V1\right) + Q_{max} & K = \frac{\Delta Q}{\Delta V} = \frac{Q_{max}}{V1-V2} & V1 < V \leq V2 \\ 0 & K = \frac{\Delta Q}{\Delta V} = 0 & V2 < V \leq V3 \\ \left(\frac{Q_{max}}{V3-V4}\right)\left(v_{gd}^c - V3\right), & K = \frac{\Delta Q}{\Delta V} = \frac{Q_{max}}{V3-V4} & V3 < V \leq V4 \\ -Q_{max} & K = \frac{\Delta Q}{\Delta V} = 0 & V > V4 \end{cases} \tag{3.49}$$

where K is the slope of the droop curve.

Consider that the ac bus voltage is measured to be between $V3$ and $V4$ and, thus, the inverter operates in the inductive region of the volt-var droop curve. Then, by (3.49),

$$q^* = K\left(v_{gd}^c - V3\right), \qquad K = \left(\frac{Q_{max}}{V3 - V4}\right) \tag{3.50}$$

This expression is substituted into (3.44) to obtain

$$i_q^* = \left(k_{qp} + \frac{k_{qi}}{s}\right)\left(K\left(v_{gd}^c - V3\right) + v_{gd}^c i_{gq}^c - v_{gq}^c i_{gd}^c\right) \tag{3.51}$$

Similar to the procedure for the fixed reactive power control, the small-signal expression of (3.51) is

$$\tilde{i}_q^* = \begin{bmatrix} -G_{qs}V_{gq}^c & G_{qs}V_{gd}^c \end{bmatrix} \begin{bmatrix} \tilde{i}_{gd}^c \\ \tilde{i}_{gq}^c \end{bmatrix} + \begin{bmatrix} G_{qs}\left(I_{gq}^c + K\right) & -G_{qs}I_{gd}^c \end{bmatrix} \begin{bmatrix} \tilde{v}_{gd}^c \\ \tilde{v}_{gq}^c \end{bmatrix} \tag{3.52}$$

Combining the expression for $\tilde{i}_d^*$ from (3.41) with the expression for $\tilde{i}_q^*$ just obtained, then

$$\begin{bmatrix} \tilde{i}_d^* \\ \tilde{i}_q^* \end{bmatrix} = \mathbf{G_{cvd}} \left(\tilde{v}_{dc}^* - \tilde{v}_{dc} \right) + \mathbf{G_{qi}} \begin{bmatrix} \tilde{i}_{gd}^c \\ \tilde{i}_{gq}^c \end{bmatrix} + \mathbf{G_{cvq}} \begin{bmatrix} \tilde{v}_{gd}^c \\ \tilde{v}_{gq}^c \end{bmatrix} \tag{3.53}$$

where

$$\mathbf{G_{cvd}} = \begin{bmatrix} k_{dcp} + \frac{k_{dci}}{s} \\ 0 \end{bmatrix}, \quad \mathbf{G_{qi}} = \begin{bmatrix} 0 & 0 \\ -G_{qs} V_{gq}^c & G_{qs} V_{gd}^c \end{bmatrix}, \quad \text{and} \quad \mathbf{G_{cvq}} \begin{bmatrix} 0 & 0 \\ G_{qs} \left(I_{gq}^c + K \right) & -G_{qs} I_{gd}^c \end{bmatrix}.$$

It is clear to see that the expression for (3.53) is identical to (3.48) and the difference lies in the matrices relating the inputs to the power controller to the outputs fed to the inner control loop. As a result, the structure of the small-signal model remains unchanged from Fig. 3.14 for all modes of operation. It should be noted that for unity power factor operation, $\mathbf{G_{qi}}$ and $\mathbf{G_{cvq}}$ are 2×2 zero matrices. Additionally, the same procedure can be applied for capacitive reactive power injection in volt-var mode.

3.4 Terminal Ac Impedance Derivation

The *dq* ac impedance of the inverter is derived from solving the equations in (3.54), which are obtained from the small-signal model in Fig. 3.14.

$$\begin{cases} \tilde{\mathbf{i}}^* = \mathbf{G_{cvd}}\left(\tilde{v}_{dc}^* - \tilde{v}_{dc}\right) + \mathbf{G_{ciq}}\tilde{\mathbf{i}}_g^c + \mathbf{G_{cvq}}\tilde{\mathbf{v}}_g^c \\ \tilde{\mathbf{v}}_g^c = \mathbf{G_{PLL}^v}\tilde{\mathbf{v}}_g^s \\ \tilde{\mathbf{i}}_g^c = \tilde{\mathbf{i}}_g^s + \mathbf{G_{PLL}^i}\tilde{\mathbf{v}}_g^s \\ \tilde{v}_{dc} = \mathbf{G_{Dd}}\tilde{\mathbf{d}}^s + \mathbf{G_{Dv}}\tilde{\mathbf{v}}_g^s \\ \tilde{\mathbf{d}}^c = \mathbf{G_{ci}}\left(\tilde{\mathbf{i}}^* - \tilde{\mathbf{i}}_g^c\right) + \mathbf{G_{dei}}\tilde{\mathbf{i}}_g^c \\ \tilde{\mathbf{d}}^s = \mathbf{G_{del}}\left(\mathbf{G_{PLL}^d}\tilde{\mathbf{v}}_g^s + \tilde{\mathbf{d}}^c\right) \\ \tilde{\mathbf{i}}_g^s = \mathbf{G_{iv}}\tilde{\mathbf{v}}_g^s + \mathbf{G_{id}}\tilde{\mathbf{d}}^s \end{cases} \tag{3.54}$$

In order to derive the terminal *dq* ac impedance of the PV inverter for each mode of operation for the grid-tracking control, $\tilde{\mathbf{v}}_{dc}$, $\tilde{\mathbf{i}}_g^c$, and $\tilde{\mathbf{v}}_g^c$ are first substituted into $\tilde{\mathbf{i}}^*$ such that

$$\tilde{\mathbf{i}}^* = \mathbf{G_{cvd}}\left(\tilde{v}_{dc}^* - \mathbf{G_{Dd}}\tilde{\mathbf{d}}^s - \mathbf{G_{Dv}}\tilde{\mathbf{v}}_g^s\right) + \mathbf{G_{ciq}}\left(\tilde{\mathbf{i}}_g^s + \mathbf{G_{PLL}^i}\tilde{\mathbf{v}}_g^s\right) + \mathbf{G_{cvq}}\mathbf{G_{PLL}^v}\tilde{\mathbf{v}}_g^s \tag{3.55}$$

Substituting $\tilde{\mathbf{i}}^*$ into $\tilde{\mathbf{d}}^c$ and combining like-terms yields

$$\begin{aligned} \tilde{\mathbf{d}}^c = &- \mathbf{G_{ci}}\mathbf{G_{cvd}}\mathbf{G_{Dd}}\tilde{\mathbf{d}}^s + \left(\mathbf{G_{ci}}\mathbf{G_{ciq}} - \mathbf{G_{ci}} + \mathbf{G_{dei}}\right)\tilde{\mathbf{i}}_g^s + \\ &\left(\mathbf{G_{ci}}\mathbf{G_{ciq}}\mathbf{G_{PLL}^i} + \mathbf{G_{ci}}\mathbf{G_{cvq}}\mathbf{G_{PLL}^v} - \mathbf{G_{ci}}\mathbf{G_{PLL}^i} + \mathbf{G_{dei}}\mathbf{G_{PLL}^i} - \mathbf{G_{ci}}\mathbf{G_{cvd}}\mathbf{G_{Dv}}\right)\tilde{\mathbf{v}}_g^s \end{aligned} \tag{3.56}$$

Then, $\tilde{\mathbf{d}}^c$ is substituted into $\tilde{\mathbf{d}}^s$. Solving for $\tilde{\mathbf{d}}^s$ and combining like-terms

$$\begin{aligned}\tilde{\mathbf{d}}^s = &\left(\mathbf{I}+\mathbf{G_{del}}\mathbf{G_{ci}}\mathbf{G_{cvd}}\mathbf{G_{Dd}}\right)^{-1}\left[\mathbf{G_{del}}\left(\mathbf{G_{ci}}\mathbf{G_{ciq}}-\mathbf{G_{ci}}+\mathbf{G_{dei}}\right)\right]\tilde{\mathbf{i}}^{\mathbf{s}}_{\mathbf{g}}+\\ &\left(\mathbf{I}+\mathbf{G_{del}}\mathbf{G_{ci}}\mathbf{G_{cvd}}\mathbf{G_{Dd}}\right)^{-1}\left[\mathbf{G_{del}}\left(\mathbf{G^{d}_{PLL}}+\mathbf{G_{ci}}\mathbf{G_{ciq}}\mathbf{G^{i}_{PLL}}+\mathbf{G_{ci}}\mathbf{G_{cvq}}\mathbf{G^{v}_{PLL}}-\right.\right.\\ &\left.\left.\mathbf{G_{ci}}\mathbf{G^{i}_{PLL}}+\mathbf{G_{dei}}\mathbf{G^{i}_{PLL}}-\mathbf{G_{ci}}\mathbf{G_{cvd}}\mathbf{G_{Dv}}\right)\right]\tilde{\mathbf{v}}^s_g\end{aligned} \tag{3.57}$$

Finally, $\tilde{\mathbf{d}}^s$ is substituted into $\tilde{\mathbf{i}}^s_g$, from which the resulting terminal dq ac impedance of the PV inverter for all three modes of operation is derived as

$$\begin{aligned}\mathbf{Z}=\frac{\tilde{\mathbf{v}}^s_g}{-\tilde{\mathbf{i}}^s_g}=-&\left[\mathbf{G_{iv}}+\mathbf{G_{id}}\left(\mathbf{I}+\mathbf{G_{del}}\mathbf{G_{ci}}\mathbf{G_{cvd}}\mathbf{G_{Dd}}\right)^{-1}\cdot\right.\\ &\left[\mathbf{G_{del}}\left(\mathbf{G^{d}_{PLL}}+\mathbf{G_{ci}}\mathbf{G_{ciq}}\mathbf{G^{i}_{PLL}}+\mathbf{G_{ci}}\mathbf{G_{cvq}}\mathbf{G^{v}_{PLL}}-\mathbf{G_{ci}}\mathbf{G^{i}_{PLL}}+\right.\right.\\ &\left.\left.\mathbf{G_{dei}}\mathbf{G^{i}_{PLL}}-\mathbf{G_{ci}}\mathbf{G_{cvd}}\mathbf{G_{Dv}}\right)\right]^{-1}\cdot\\ &\left.\left[\mathbf{I}-\mathbf{G_{id}}\left(\mathbf{I}+\mathbf{G_{del}}\mathbf{G_{ci}}\mathbf{G_{cvd}}\mathbf{G_{Dd}}\right)^{-1}\left[\mathbf{G_{del}}\left(\mathbf{G_{ci}}\mathbf{G_{ciq}}-\mathbf{G_{ci}}+\mathbf{G_{dei}}\right)\right]\right]\right.\end{aligned} \tag{3.58}$$

where $\mathbf{G_{ciq}}$ and $\mathbf{G_{cvq}}$ are dependent on the mode of operation of the inverter.

The derived closed form of the terminal dq ac impedance for each mode of operation is compared to the numerical linearization using MATLAB Simulink and is shown in Figs. 3.16 - 3.18. For each operating mode, the closed form derivation matches the numerical linearization. The discrepancy in the magnitude of Z_{dq} at low frequency in Fig. 3.16 is due to the small magnitude in which the numerical linearization cannot achieve due to numerical error in the simulated environment.

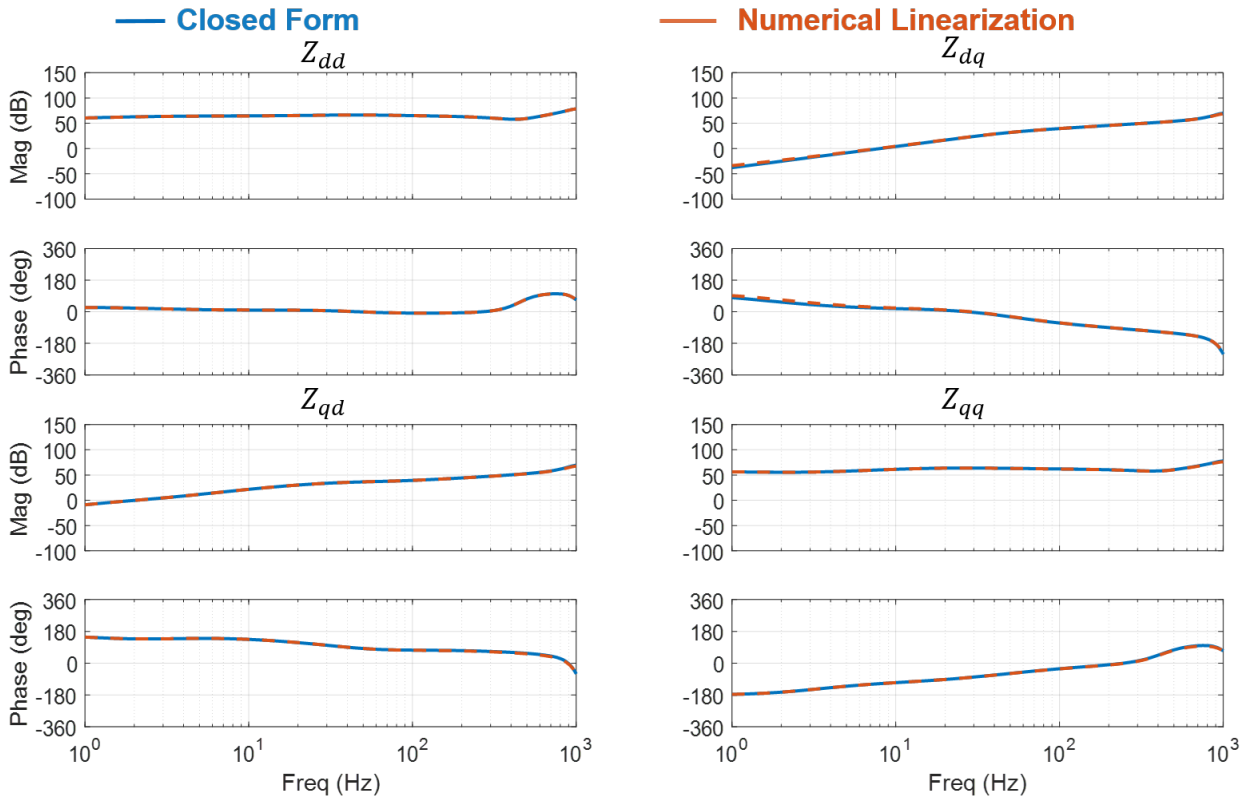

Figure 3.16: PV inverter terminal ac impedance under unity power factor mode for grid-tracking control.

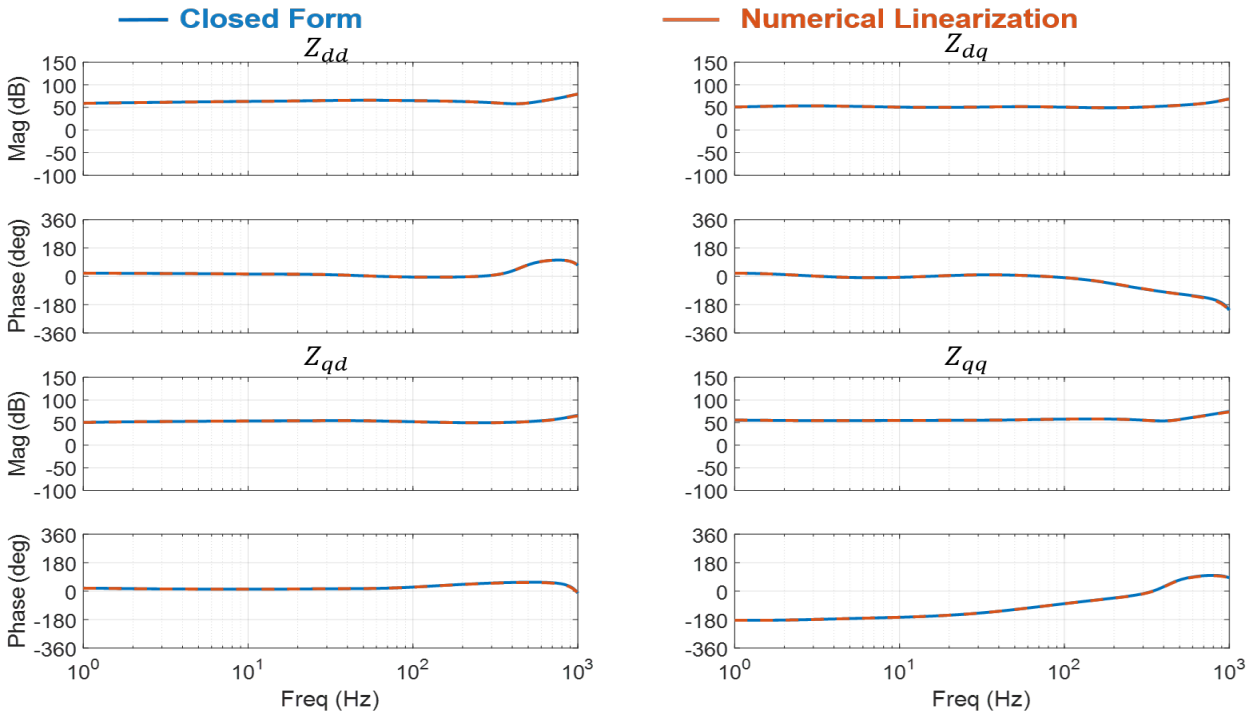

Figure 3.17: PV inverter terminal ac impedance under fixed reactive power mode for grid-tracking control.

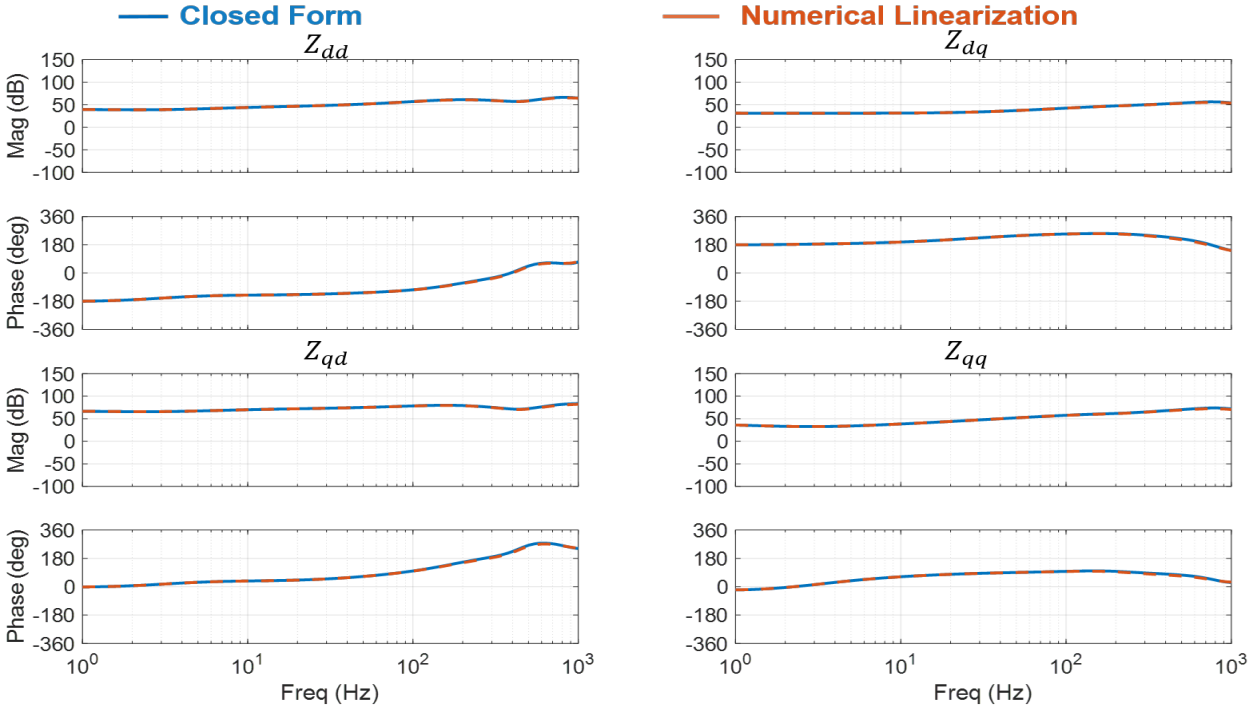

Figure 3.18: PV inverter terminal ac impedance under volt-var mode for grid-tracking control.

Fig. 3.19 compares the terminal ac impedance in the dq frame of the PV inverter with dq frame PLL-oriented vector control for the three operating modes considered in this work: unity power factor (blue), fixed reactive power (orange), and volt-var (yellow). Under unity power factor mode, the PV inverter is operating at $P = 250$ kW and $Q = 0$ kvar, whereas the PV inverter operates at $P = 250$ kW and $Q = -75$ kvar under fixed reactive power and volt-var modes. When the PV inverter operates under unity power factor mode, the terminal ac impedance is diagonally dominant in that the magnitudes of the Z_{dd} and Z_{qq} terms are considerably larger than Z_{dq} and Z_{qd} due to the fact that the reactive power injection is 0 kvar [32]. On the other hand, under the reactive power control modes, the terminal ac impedance of the inverter is not diagonally dominant, and thus, a conclusion on the system stability cannot be drawn. However, under volt-var mode, the signs of Z_{dd} and Z_{qq} are flipped such that Z_{qq} no longer is an incremental negative resistor at low frequency while Z_{dd} becomes a incremental negative resistor.

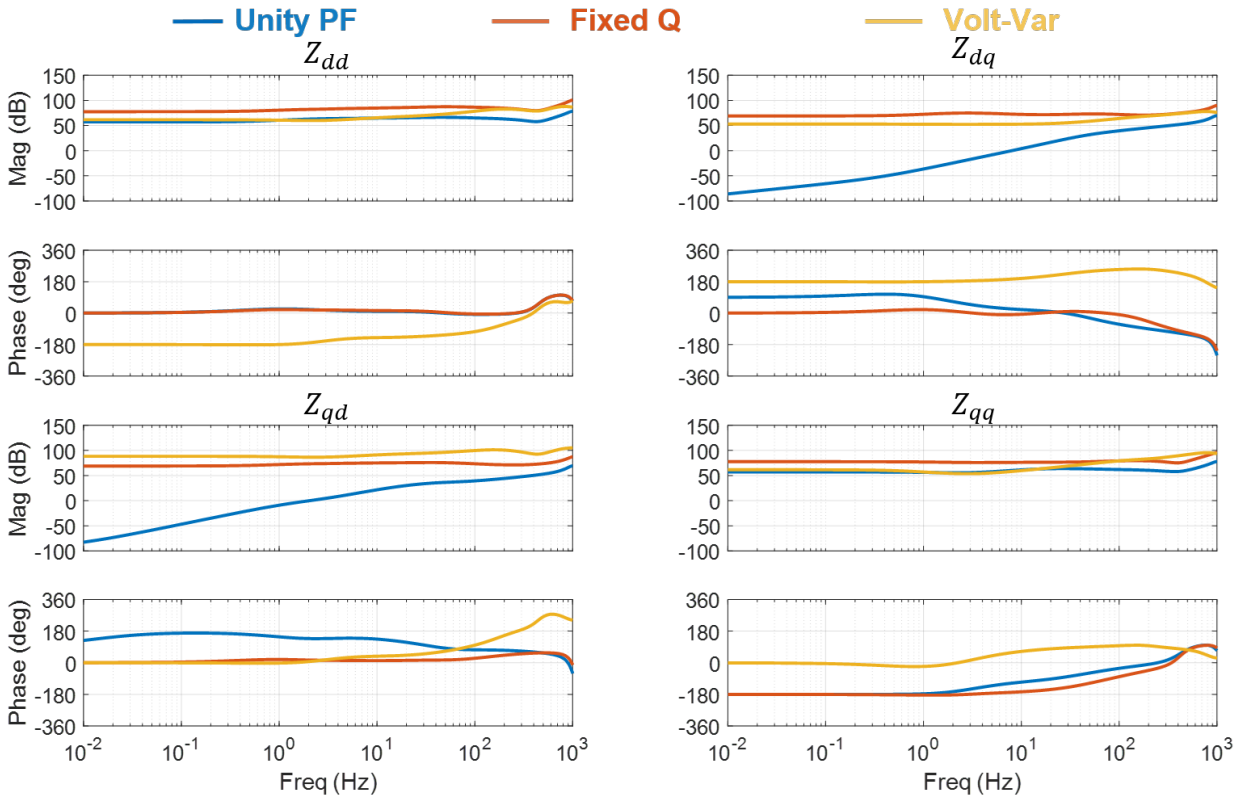

Figure 3.19: Comparison of terminal ac impedance with grid-tracking control for different modes of operation.

Chapter 4

Grid-Forming Control

4.1 Introduction

In this chapter, the design of a grid-forming control scheme is provided while also analyzing the effect of parameter changes on the control loops. The grid-forming control scheme is based on the concept of a virtual synchronous machine, discussed in Chapter 2, and comprises a cascaded control structure similar to the *dq* frame PLL-oriented vector control from Chapter 3. However, the main differences lie in the synchronization scheme in addition to the outer voltage control loop.

This chapter will discuss the design of the grid-forming control structure, including the influence of the new synchronization scheme on the small-signal model. Additionally, the effect of varying key parameters will be analyzed. Finally, the terminal *dq* ac impedance will be derived for this control scheme and will be compared to the impedance obtained from Chapter 3.

4.2 Synchronous Machine Fundamentals

A simple 2-pole synchronous machine is shown in Fig. 4.1, in which a dc current in the rotor (field) windings generates a magnetic flux across the air gap between the rotor and stator of the machine. As the rotor spins, the magnetic field also rotates, thus inducing a balanced three-phase voltage on the three-phase stator windings, denoted by $\mathbf{E}_A$. However, when current flows through the machine to some connected load, the voltage measured at the output of the machine, also known as the terminal voltage $\mathbf{V}_\phi$, will not be the same as the generated internal voltage. The difference between the internal and terminal voltages is attributed to several primary characteristics of the machine, including

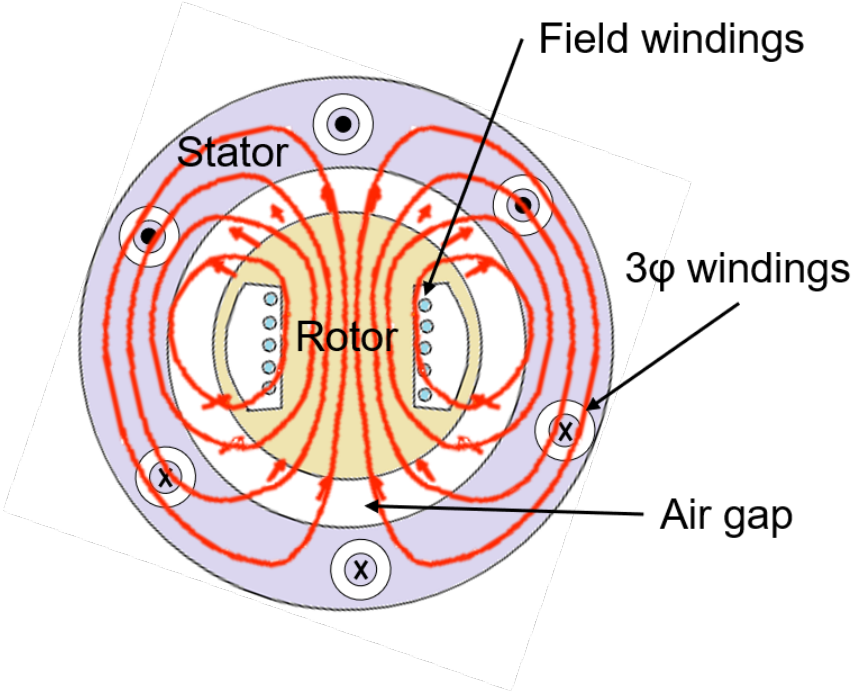

Figure 4.1: Simple 2-pole synchronous machine.

1. the armature reaction,

2. the self-inductance of the armature coils, and

3. the resistance of the armature coils [80].

Consider, first, the armature reaction. Recall that the induced voltage in the stator windings due to the spinning magnetic field, $\mathbf{B}_R$, is $\mathbf{E}_A$. Therefore, when a load is attached to the machine, ac current, $\mathbf{I}_A$, flows in the stator (armature) windings, which induces a separate magnetic field, $\mathbf{B}_S$. This current, in turn, induces a separate stator voltage, $\mathbf{E}_{stat}$, such that the voltage seen at the terminal of the machine is

$$\mathbf{V}_\phi = \mathbf{E}_A + \mathbf{E}_{stat} \tag{4.1}$$

as shown in Fig. 4.2. The relationship between the stator current and voltage is expressed

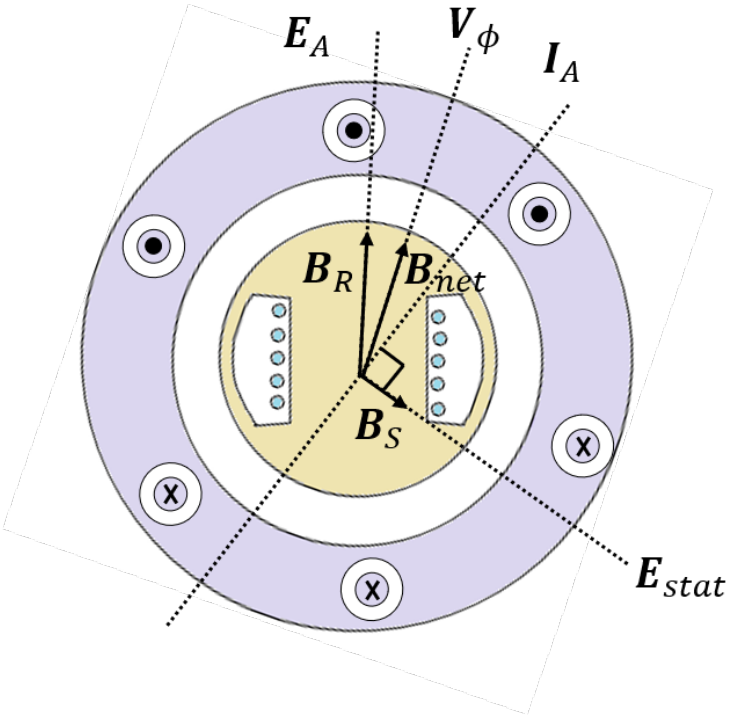

Figure 4.2: Armature reaction of a synchronous machine.

as

$$\mathbf{E}_A = -jX\mathbf{I}_A \tag{4.2}$$

such that the voltage seen at the terminal of the machine is

$$\mathbf{V}_\phi = \mathbf{E}_A - jX\mathbf{I}_A \tag{4.3}$$

Next, the self-inductance, L_A, and resistance, R_A, of the machine can be expressed as electrical components, such that (4.3) is rewritten as

$$\mathbf{V}_\phi = \mathbf{E}_A - jX\mathbf{I}_A - jX_A\mathbf{I}_A - R_A\mathbf{I}_A = \mathbf{E}_A - jX_S\mathbf{I}_A - R_A\mathbf{I}_A \tag{4.4}$$

from which a simple model of a synchronous machine is shown in Fig. 4.3.

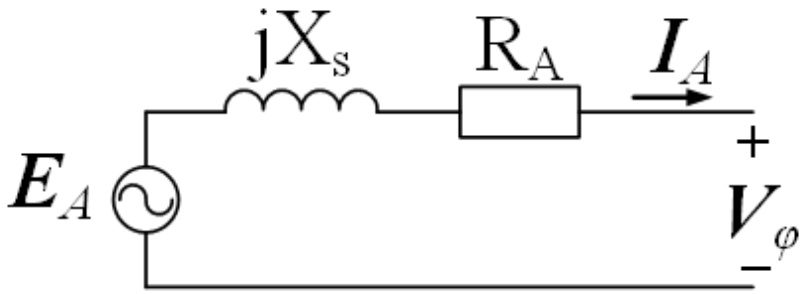

Figure 4.3: Equivalent model of a synchronous machine.

The load current, $\mathbf{I}_A$, is derived from Kirchhoff's Voltage Law, such that

$$\mathbf{I}_A = \frac{E_A \angle \delta - V_\phi \angle 0}{Z_s \angle -\theta_s} \tag{4.5}$$

where the grid voltage is taken as the reference voltage and the internal voltage of the machine has an angle difference of δ and $\mathbf{Z_s} = R_A + jX_S$. Considering a single phase of the machine, then the total apparent power exchange between two terminals is expressed as

$$\mathbf{S} = \mathbf{V}_\phi \mathbf{I}_A^* \tag{4.6}$$

where the asterisk symbolizes the complex conjugate of $\mathbf{I}_A$. Substituting (4.5) into (4.6) yields

$$\mathbf{S} = \frac{V_\phi E_A}{Z_s} \angle \theta_s - \delta - \frac{V_\phi^2}{Z_s} \angle \theta_s \tag{4.7}$$

The active power is considered to be the real component of the apparent power while the reactive power is considered to be the imaginary component such that

$$\mathbf{S} = P + jQ \tag{4.8}$$

Therefore,

$$P = Re\{\mathbf{S}\} = \frac{V_\phi E_A}{Z_s}\cos(\theta_s - \delta) - \frac{V_\phi^2}{Z_s}\cos(\theta_s) \tag{4.9}$$

$$Q = Im\{\mathbf{S}\} = \frac{V_\phi E_A}{Z_s}\sin(\theta_s - \delta) - \frac{V_\phi^2}{Z_s}\sin(\theta_s) \tag{4.10}$$

Considering that the reactance, $X_s = j\omega L_s$, of the impedance is much larger than the resistance, R_A, then (4.9) and (4.10) are rewritten as

$$P = Re\{\mathbf{S}\} = \frac{V_\phi E_A}{X_s}\cos(90^\circ - \delta) - \frac{V_\phi^2}{X_s}\cos(90^\circ) \tag{4.11}$$

$$Q = Im\{\mathbf{S}\} = \frac{V_\phi E_A}{X_s}\sin(90^\circ - \delta) - \frac{V_\phi^2}{X_s}\sin(90^\circ) \tag{4.12}$$

Simplifying and using trigonometric relationships yields

$$P = \frac{V_\phi E_A}{X_s}\sin(\delta) \tag{4.13}$$

$$Q = \frac{V_\phi E_A}{X_s}\cos(\delta) - \frac{V_\phi^2}{X_s} \tag{4.14}$$

For a synchronized condition, where δ is small and the small-angle approximation is used, then

$$P \approx \frac{V_\phi E_A}{X_s}\delta \tag{4.15}$$

$$Q \approx V_\phi\left(\frac{E_A - V_\phi}{X_s}\right) \tag{4.16}$$

It is clear to see that the power angle controls the magnitude of the active power injection while the adjustment of the internal voltage of the machine controls the magnitude of the reactive power.

4.3 Design of the Grid-Forming Control

4.3.1 Power-Balance Synchronization Loop

The ac active power is related to the power angle via the power-angle curve of a synchronous machine, as shown in Fig. 4.4, which is derived from (4.13). Using small-angle approximation such that

$$\sin\delta \approx \delta \tag{4.17}$$

then the ac active power is

$$P_{ac} = P_{max}\delta \tag{4.18}$$

where P_{max} is the maximum power capability of the system under consideration, whether it be a machine with rotating components or a power electronics system, such as an inverter.

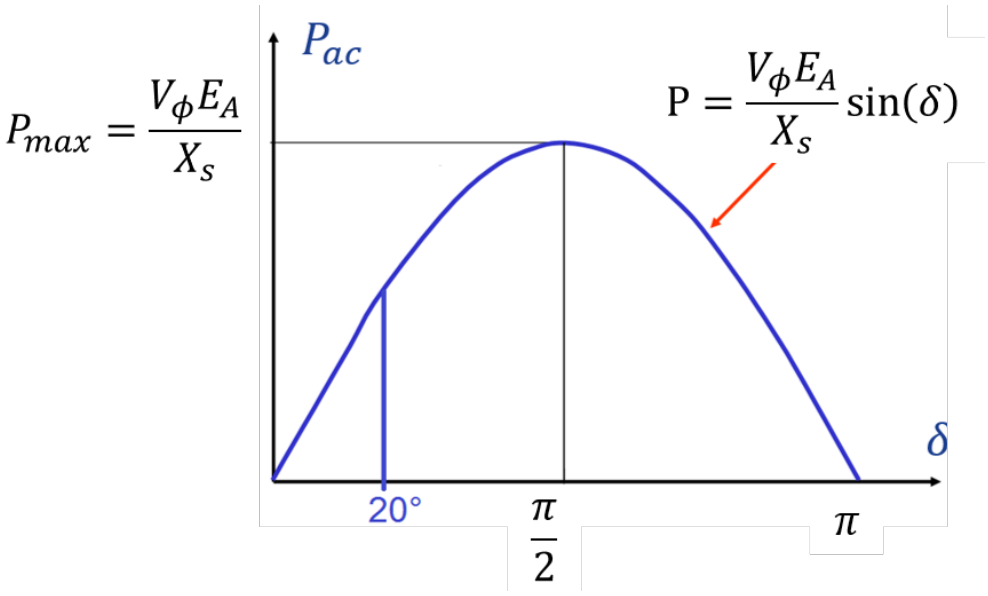

Figure 4.4: Power-angle curve of a synchronous machine.

Considering the swing equation (1.2) and (4.18), a basic control diagram of the power-balance-based synchronization is constructed, as shown in Fig. 4.5. From this figure, the

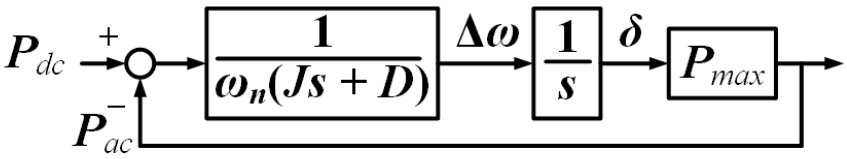

Figure 4.5: Control diagram of a basic power-balance-based synchronization.

loop gain is obtained, yielding

$$P_{ac} = P_{max} \cdot \frac{1}{s} \cdot \frac{1}{\omega_n \left(Js + D\right)} \cdot \left(P_{dc} - P_{ac}\right) \tag{4.19}$$

from which the closed loop transfer function is

$$\frac{P_{ac}}{P_{dc}} = \frac{\frac{P_{max}}{J\omega_n}}{s^2 + \frac{D}{J}s + \frac{P_{max}}{J\omega_n}} \tag{4.20}$$

It is clear to see that (4.20) resembles a second-order transfer function, (4.21), with corner frequency ω_c and damping ζ.

$$H_{2nd-order} = \frac{\omega_c^2}{s^2 + 2\zeta\omega_c s + \omega_c^2} \tag{4.21}$$

Therefore, the damping coefficient, D, can be defined as a function of ζ, J, ω_n, and P_{max} such that

$$D = 2\zeta\sqrt{\frac{J \cdot P_{max}}{\omega_n}} \tag{4.22}$$

The inertia, J, in Eq. (4.22), can be defined in terms of an inertia constant, H, which relates the kinetic energy of the rotor to the power rating, S_n, of a synchronous machine. In mathematical terms,

$$H = \frac{J\omega_n^2}{2S_n} \tag{4.23}$$

The parameters for the power-balanced-based synchronization utilizing virtual inertia is shown in Table 4.1. These parameters result in a synchronization loop bandwidth of 1 Hz for the grid-forming control scheme. The synchronization loop of the grid-forming control can be compared to that of the grid-tracking control scheme, as shown in Fig. 4.6.

Table 4.1: Parameters of the Power-Balance Synchronization Loop

P_{max}	250 kW
H	7 sec
ζ	0.7
J	24.6267 kg-m^2
D	178.9103
ω_n	$2\pi 60$ rad/s

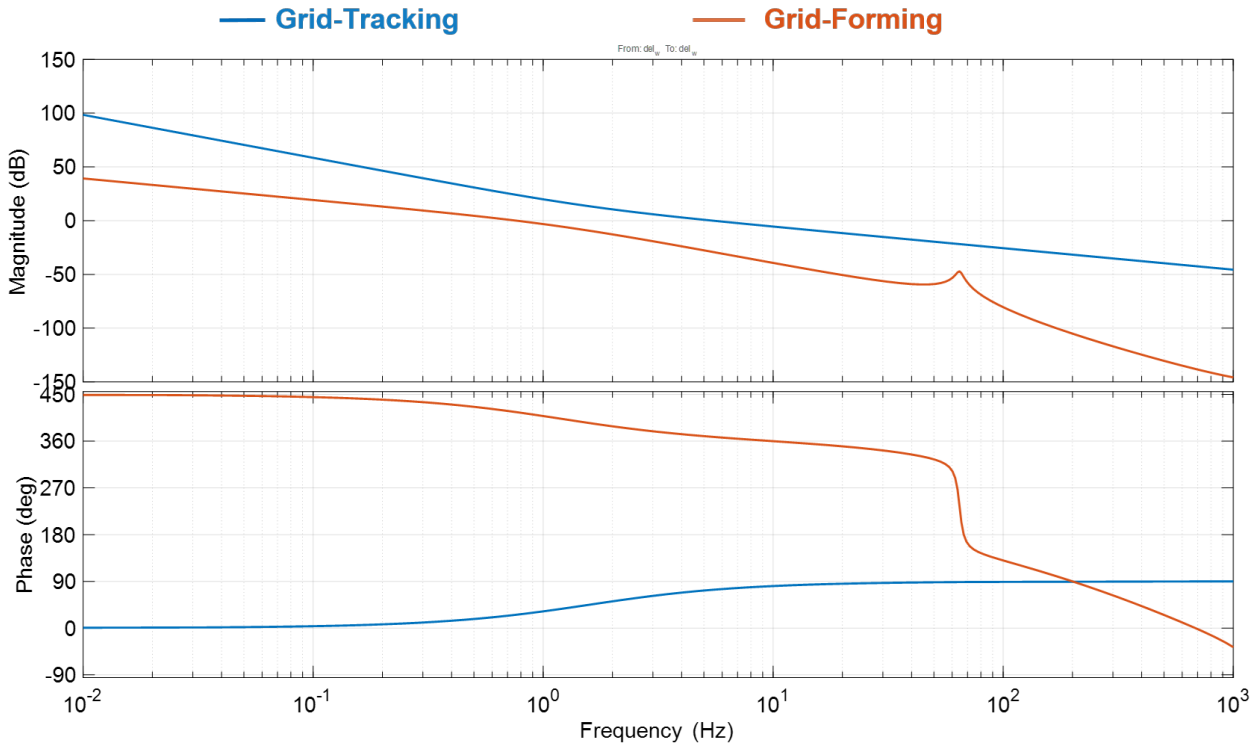

Figure 4.6: Comparison of the synchronization loop gain of two controllers.

4.3.1.1 Influence of Power-Balance Synchronization

Similar to the influence of the phase-locked-loop (PLL) on the small-signal model, the power-balance synchronization also introduces two dq frames: that of the grid, denoted by superscript s, and that of the controller, denoted by superscript c. Once again, the grid frame is defined by the voltage of the grid at the PCC while the controller frame is defined by the power-balance synchronization. In steady-state, the two frames are aligned; however, when small-signal perturbations are introduced into the system, the two frames are unaligned, with angle deviation δ, and the power-balance synchronization loop will work to realign the two frames.

The effect of the power-balance synchronization is considered in the voltage and current signals, which are passed to the controller, in addition to the duty cycles, which are passed to the system frame to drive the switching of the inverter. Similar to the derivation process used to obtain an expression for δ in the PLL case, it is also necessary to obtain an expression for δ in the power-balance case in order to continue analyzing the influence of this synchronization method on the small-signal model. From Fig. 4.5, the large signal δ is

$$\overline{\delta} = \frac{1}{s}\left[\frac{1}{\omega_n\left(Js + D\right)}\right]\left(\overline{p}_{dc} - \overline{p}_{ac}\right) \tag{4.24}$$

where $\overline{p}_{dc}$ and $\overline{p}_{ac}$ are rewritten in terms of the system variables such that

$$\overline{\delta} = \frac{1}{s}\left[\frac{1}{\omega_n\left(Js + D\right)}\right]\left(\overline{v}_{dc}\overline{i}_{dc} - \overline{v}^s_{g,d}\overline{i}^s_{g,d} - \overline{v}^s_{g,q}\overline{i}^s_{g,q}\right) \tag{4.25}$$

Deriving the small-signal expression of (4.25) and making p_{dc} constant gives

$$\tilde{\delta} = \frac{1}{s}\left[\frac{1}{\omega_n\left(Js+D\right)}\right]\left(-\begin{bmatrix} I^s_{g,d} & I^s_{g,q}\end{bmatrix}\begin{bmatrix}\tilde{v}^s_{g,d}\\ \tilde{v}^s_{g,q}\end{bmatrix} - \begin{bmatrix} V^s_{g,d} & V^s_{g,q}\end{bmatrix}\begin{bmatrix}\tilde{i}^s_{g,d}\\ \tilde{i}^s_{g,q}\end{bmatrix}\right) \tag{4.26}$$

Recall from 3.2.1.1 that the grid voltage, grid current, and duty cycles are passed between the grid dq frame and controller dq frame. When a small-signal perturbation is added to these signals, then

$$\begin{bmatrix}\tilde{v}^c_{gd}\\ \tilde{v}^c_{gq}\end{bmatrix} \approx \begin{bmatrix}\tilde{v}^s_{gd} + V^s_{g,q}\tilde{\delta}\\ \tilde{v}^s_{gq} - V^s_{g,d}\tilde{\delta}\end{bmatrix} \tag{4.27}$$

$$\begin{bmatrix}\tilde{i}^c_{gd}\\ \tilde{i}^c_{gq}\end{bmatrix} \approx \begin{bmatrix}\tilde{i}^s_{gd} + I^s_{g,q}\tilde{\delta}\\ \tilde{i}^s_{gq} - I^s_{g,d}\tilde{\delta}\end{bmatrix} \tag{4.28}$$

$$\begin{bmatrix}\tilde{d}^s_{d}\\ \tilde{d}^s_{q}\end{bmatrix} \approx \begin{bmatrix}\tilde{d}^c_{d} - D^c_{q}\tilde{\delta}\\ \tilde{d}^c_{q} + D^c_{d}\tilde{\delta}\end{bmatrix} \tag{4.29}$$

Substituting (4.26) into (4.27) - (4.29) yields

$$\begin{aligned}
\begin{bmatrix}\tilde{v}^c_{gd}\\ \tilde{v}^c_{gq}\end{bmatrix} &\approx \mathbf{G^v_{iVSM}}\begin{bmatrix}\tilde{i}^s_{gd}\\ \tilde{i}^s_{gq}\end{bmatrix} + \mathbf{G^v_{vVSM}}\begin{bmatrix}\tilde{v}^s_{gd}\\ \tilde{v}^s_{gq}\end{bmatrix}\\
\begin{bmatrix}\tilde{i}^c_{gd}\\ \tilde{i}^c_{gq}\end{bmatrix} &\approx \mathbf{G^i_{iVSM}}\begin{bmatrix}\tilde{i}^s_{gd}\\ \tilde{i}^s_{gq}\end{bmatrix} + \mathbf{G^i_{vVSM}}\begin{bmatrix}\tilde{v}^s_{gd}\\ \tilde{v}^s_{gq}\end{bmatrix}\\
\begin{bmatrix}\tilde{d}^s_{gd}\\ \tilde{d}^s_{gq}\end{bmatrix} \approx \begin{bmatrix}\tilde{d}^c_{gd}\\ \tilde{d}^c_{gq}\end{bmatrix} &+ \mathbf{G^d_{iVSM}}\begin{bmatrix}\tilde{i}^s_{gd}\\ \tilde{i}^s_{gq}\end{bmatrix} + \mathbf{G^d_{vVSM}}\begin{bmatrix}\tilde{v}^s_{gd}\\ \tilde{v}^s_{gq}\end{bmatrix}
\end{aligned} \tag{4.30}$$

where

$$\mathbf{G^v_{vVSM}} = \left(\mathbf{I} - \mathbf{G^v_{VSM}I^s_g}\right) \qquad \mathbf{G^v_{iVSM}} = -\mathbf{G^v_{VSM}V^s_g}$$
$$\mathbf{G^i_{vVSM}} = -\mathbf{G^i_{VSM}I^s_g} \qquad \mathbf{G^i_{iVSM}} = \left(\mathbf{I} - \mathbf{G^i_{VSM}V^s_g}\right)$$
$$\mathbf{G^d_{vVSM}} = -\mathbf{G^d_{VSM}I^s_g} \qquad \mathbf{G^d_{iVSM}} = -\mathbf{G^d_{VSM}V^s_g}$$

such that

$$\mathbf{G^v_{VSM}} = \begin{bmatrix} \frac{V^s_{gq}}{\omega_n(Js+D)} \\ \frac{-V^s_{gd}}{\omega_n(Js+D)} \end{bmatrix} \qquad \mathbf{G^i_{VSM}} = \begin{bmatrix} \frac{I^s_{gq}}{\omega_n(Js+D)} \\ \frac{-I^s_{gd}}{\omega_n(Js+D)} \end{bmatrix} \qquad \mathbf{G^d_{VSM}} = \begin{bmatrix} \frac{-D^c_q}{\omega_n(Js+D)} \\ \frac{D^c_d}{\omega_n(Js+D)} \end{bmatrix}$$

The influence of the power-balance synchronization from (4.30) is incorporated in the small-signal control block diagram in blue in Fig. 4.7, which can be directly compared to Fig. 3.6.

4.3.2 AC Current Loop

As mentioned in 4.1, the grid-forming control scheme is comprised of a cascaded structure in which the innermost loop is a conventional ac current control loop, like that discussed in 3.2.2, with a PI regulator on the d- and q-channels which once again takes the deviation of the measured current passed to the controller from a reference current and output the duty cycles used for the modulation of the switching network. Additionally, a decoupling term is once again included to decouple the two channels for independent control. The control structure of this loop is identical to that shown in Fig. 3.7. Including the ac current loop in the small-signal model of the grid-forming control using the same procedure from 3.2.2 is shown in black in Fig. 4.8. The expression for the ac current loop gain is derived as

$$\frac{\tilde{\mathbf{i}}^{\mathbf{c}}_{\mathbf{g}}}{\left(\tilde{\mathbf{i}}^{*} - \tilde{\mathbf{i}}^{\mathbf{c}}_{\mathbf{g}}\right)} = \left[\left(\mathbf{I} - \mathbf{G^i_{iVSM}}\left(\mathbf{I} - \mathbf{G_{id}G_{del}G^d_{iVSM}}\right)^{-1}\mathbf{G_{id}G_{del}G_{dei}}\right)\right]^{-1} \cdot \mathbf{G^i_{iVSM}}\left(\mathbf{I} - \mathbf{G_{id}G_{del}G^d_{iVSM}}\right)^{-1}\mathbf{G_{id}G_{del}G_{ci}} \tag{4.31}$$

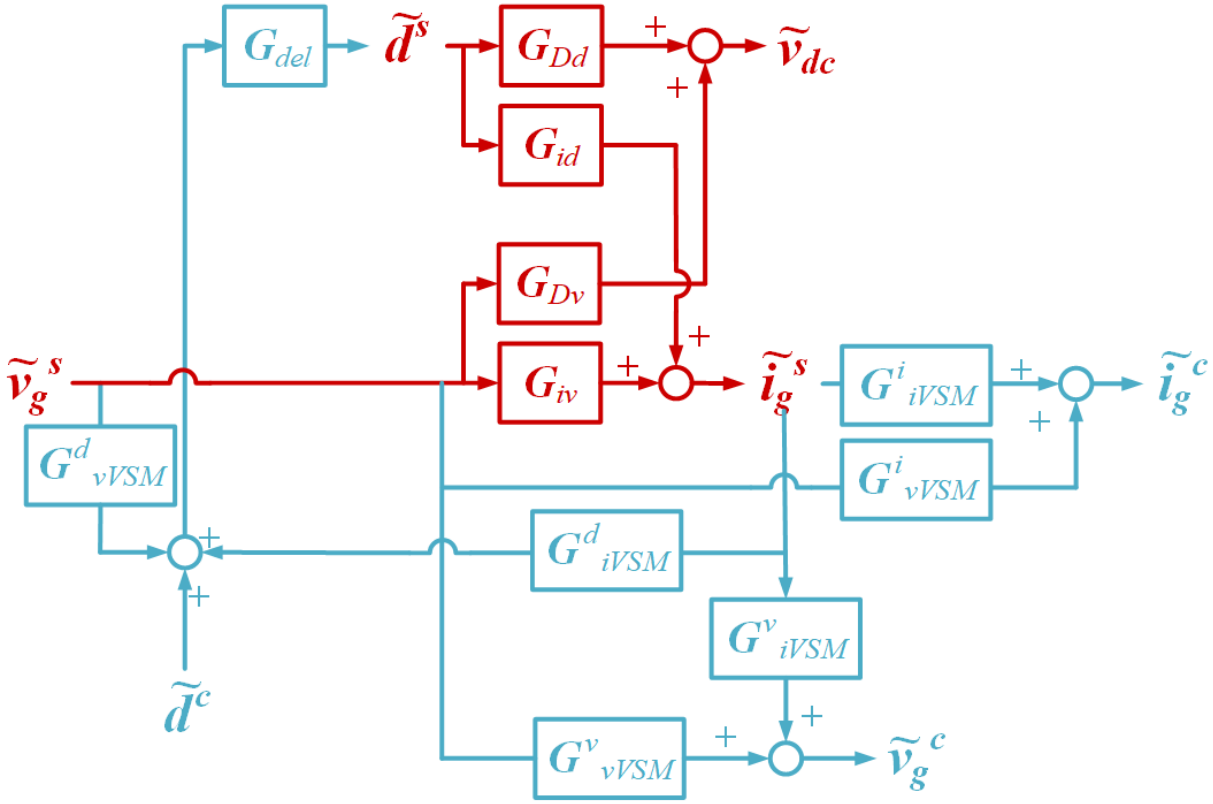

Figure 4.7: Influence of the power-balance synchronization in the small-signal model.

The PI gains used in the grid-forming ac current loop are shown in Table 4.2 and result in an ac current loop gain bandwidth of 293 Hz. Fig. 4.9 confirms the bandwidth design for the inner ac current loop for the grid-forming scheme and shows the comparison between the derived closed form and numerical linearization using MATLAB Simulink; it is clear to see that the two match.

Table 4.2: Grid-forming Ac Current Loop PI gains

k_{ip}	0.0014
k_{ii}	0.2614

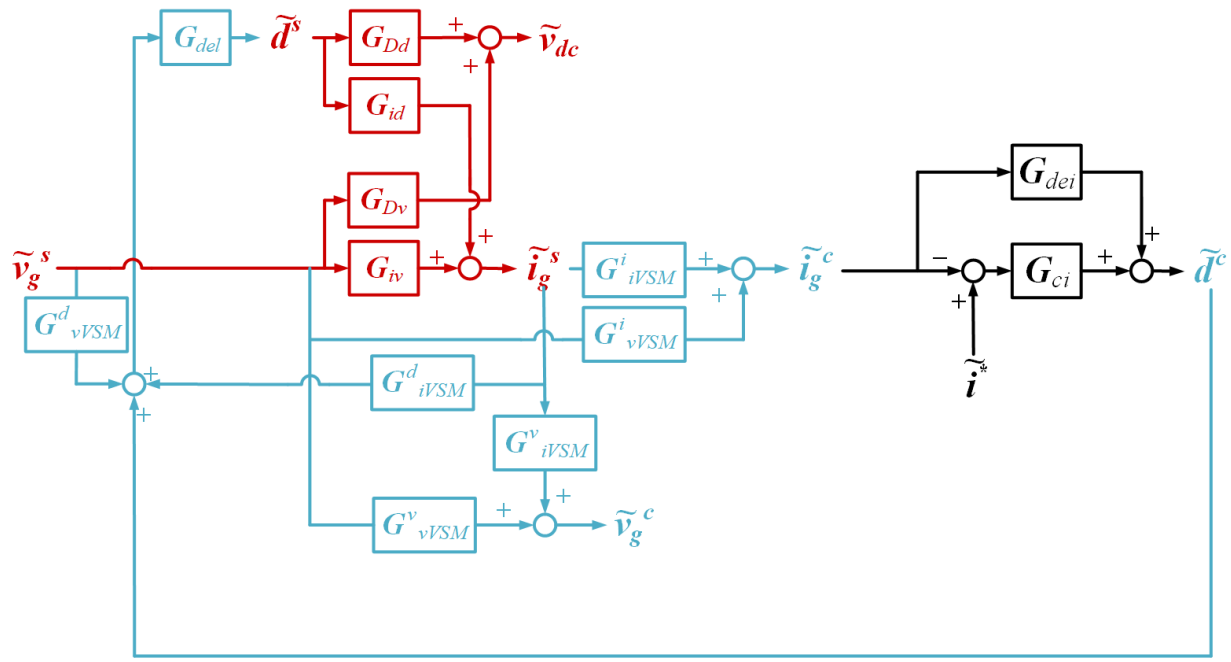

Figure 4.8: Small-signal model with ac current loop for grid-forming control.

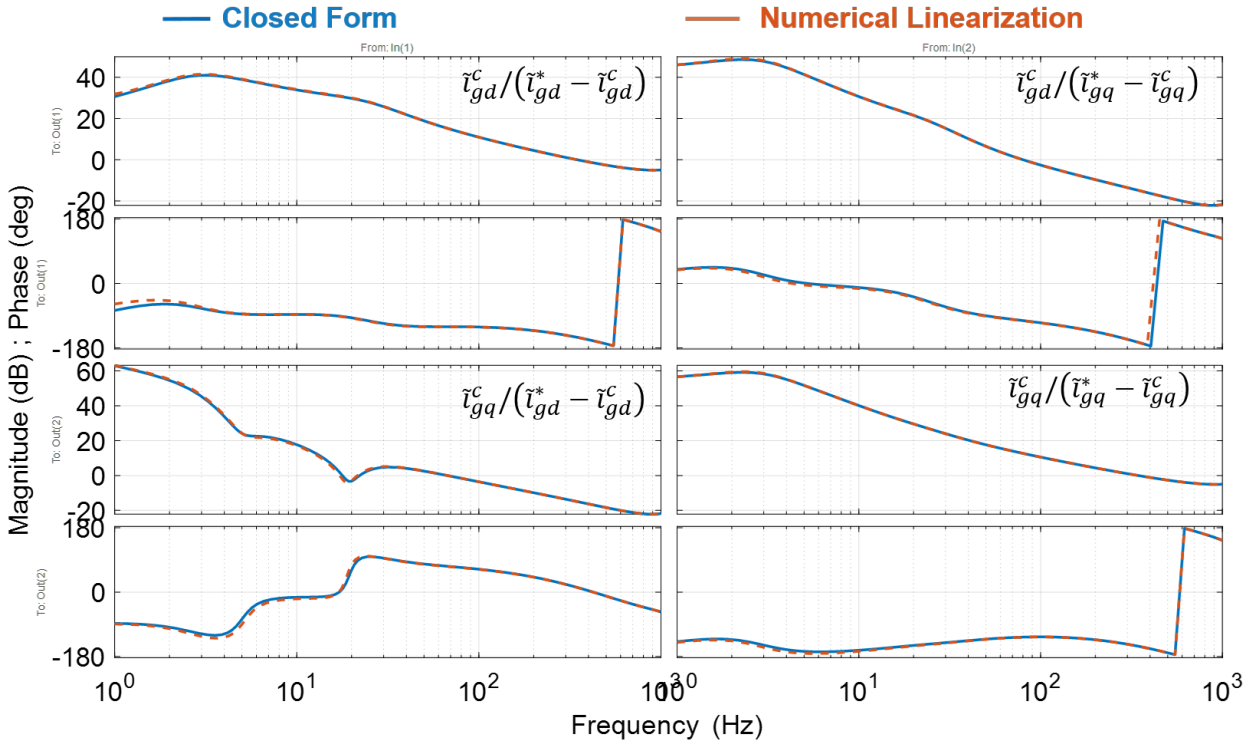

Figure 4.9: Bode plot of ac current loop gain for grid-forming control.

4.3.3 Virtual Impedance

The grid-forming control scheme for the PV inverter aims to emulate the behavior of a conventional synchronous machine (SM). The electromechanical concept of the SM is implemented in the power-balance synchronization scheme; however, the electrical operation of the machine must still be considered.

Recall from section 4.2 that the voltage seen at the terminals of a machine does not equal the internal voltage when a load is connected. The equivalent electrical model in Fig. 4.3 can be retrofitted for the PV inverter control such that the internal voltage in the coils of the stator is denoted by e and the terminal voltage v_g. The resulting equation is shown in (4.32). The model for a single-phase of the three-phase machine is shown in Fig. 4.10.

$$\mathbf{v}_g = \mathbf{e} - \mathbf{i}_v \left(L_v s + R_v\right) \tag{4.32}$$

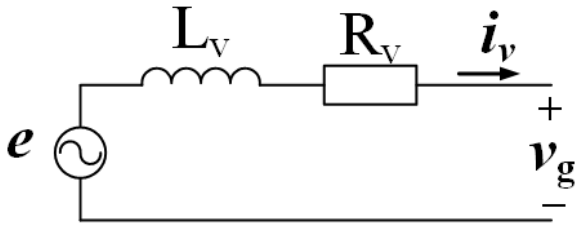

Figure 4.10: Equivalent single-phase model of a synchronous machine.

The expression in (4.32) can be used in a voltage controller, as in [81]; however, due to the derivative term, peaks and discontinuities may arise in the calculation of the voltage reference and, even with added filters, the robustness would be reduced considerably [9, 10]. Therefore, (4.32) can be modified for a current controller such that

$$\mathbf{i}_v = \frac{\mathbf{e} - \mathbf{v}_g}{\left(L_v s + R_v\right)} \tag{4.33}$$

which is based on the synchronous power controller [12, 82]. In this manner, (4.33) is a representation of the internal impedance of a virtual synchronous machine with inductance L_v and resistance R_v, which the grid-forming controller is emulating. Additionally, this equation can be used to generate the current reference, $\mathbf{i}^*$ for the inner ac current loop from 4.3.2. Transforming (4.33) from the stationary *abc* frame to the rotating synchronous *dq* frame that is being used for the control scheme of the PV inverter, the resulting control structure for the current reference generation loop is shown in Fig. 4.11, where a decoupling term exists due to the coupling induced by the reactive component, L_v.

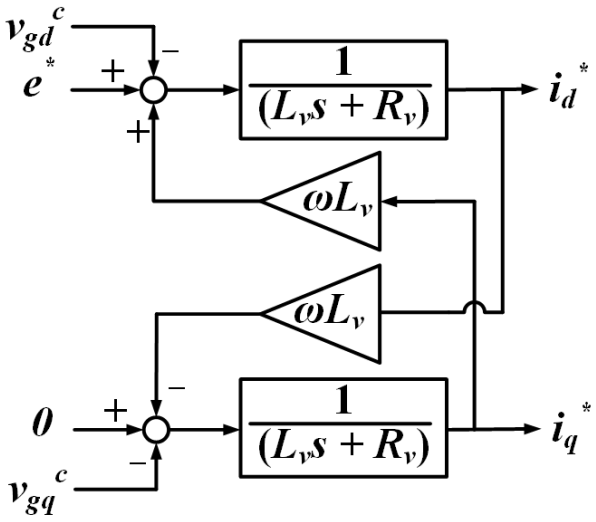

Figure 4.11: Virtual impedance controller.

As was mentioned in 3.2.3, one of the aims of the controller is to drive the q-channel voltage to zero in order to control the active and reactive power by adjusting i_d and i_q, respectively. As such, the voltage reference for the q-channel is set to 0, such that the controller will drive the q-channel of the grid voltage to 0. Alternatively, the d-channel voltage reference is determined by the power injection required of the inverter such that, for a given operating point,

$$e^* = \left|\left| \left(V_{gd}^c + jV_{gq}^c\right) + R_v \left(I_{gd}^c + jI_{gq}^c\right) + j\omega L_v \left(I_{gd}^c + jI_{gq}^c\right) \right|\right| \tag{4.34}$$

where ω is from the power-balance synchronization loop.

From Fig. 4.11, the equations for the current references generated by the virtual impedance loop are

$$i_d^* = \frac{1}{L_v s + R_v}\left(e^* - v_{gd}^c + \omega L_v i_q^*\right) \tag{4.35}$$

$$i_q^* = \frac{1}{L_v s + R_v}\left(-v_{gq}^c - \omega L_v i_d^*\right) \tag{4.36}$$

from which the small-signal is

$$\begin{bmatrix} \tilde{i}_d^* \\ \tilde{i}_q^* \end{bmatrix} = \mathbf{G_{zi}} \begin{bmatrix} \tilde{e}^* - \tilde{v}_{gd}^c \\ 0 - \tilde{v}_{gq}^c \end{bmatrix} + \mathbf{G_{dev}} \begin{bmatrix} \tilde{i}_d^* \\ \tilde{i}_q^* \end{bmatrix} \tag{4.37}$$

where

$$\mathbf{G_{zi}} = \begin{bmatrix} \frac{1}{L_v s + R_v} & 0 \\ 0 & \frac{1}{L_v s + R_v} \end{bmatrix} \quad \text{and} \quad \mathbf{G_{dev}} = \begin{bmatrix} 0 & \omega L_v \\ -\omega L_v & 0 \end{bmatrix}.$$

Equation (4.37) is incorporated into the small-signal model of the grid-forming controller as shown in Fig. 4.12 in black.

The transfer function of the virtual impedance may be rewritten to reflect the transfer function of a low-pass filter (LPF) with corner frequency ω_c and gain k such that

$$\frac{1}{L_v s + R_v} = \frac{1}{R_v}\left(\frac{1}{\frac{L_v}{R_v}s + 1}\right) = \frac{1}{R_v}\left(\frac{\frac{R_v}{L_v}}{s + \frac{R_v}{L_v}}\right) = k\left(\frac{\omega_c}{s + \omega_c}\right) \tag{4.38}$$

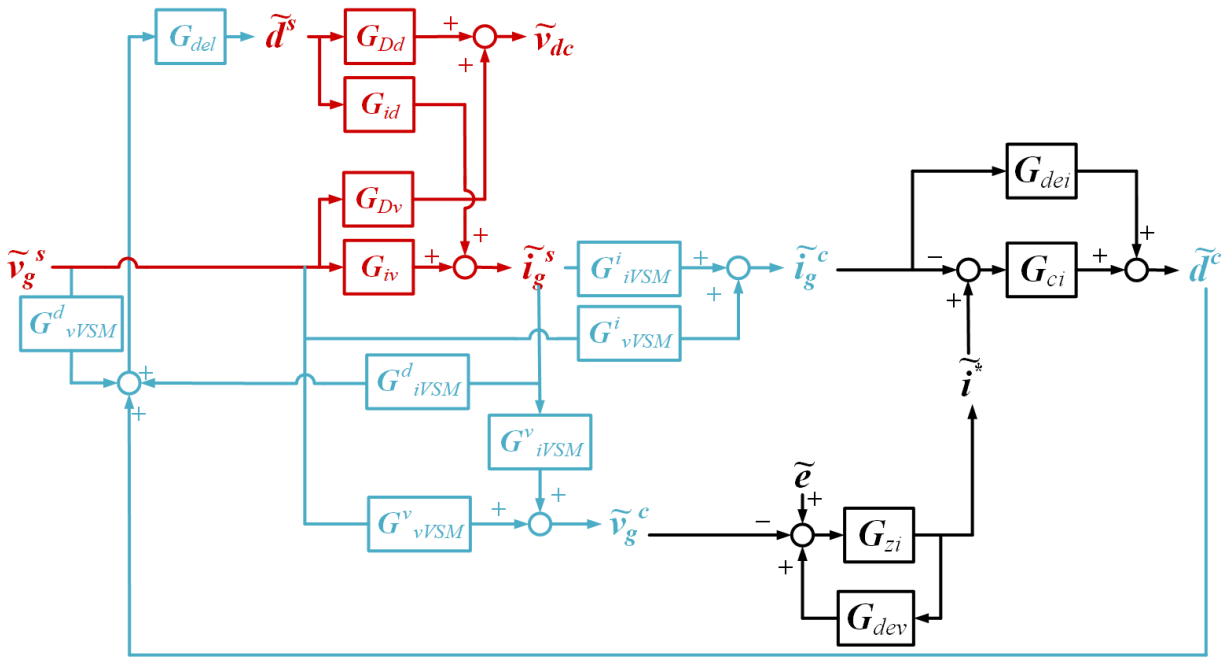

Figure 4.12: Small-signal model with virtual impedance loop for grid-forming control.

where

$$k = \frac{1}{R_v} \qquad \text{and} \qquad \omega_c = \frac{R_v}{L_v}$$

The values of the virtual impedance, consisting of L_v and R_v, are chosen based on the desired bandwidth of the low-pass filter (LPF), determined by selecting ω_c, which also sets the bandwidth of this outer loop. The approach taken in this work is such that the virtual inductance, L_v, is chosen to be 30 % of the power rating of the converter, which is a common value of the output inductance of a synchronous machine [9]. Secondly, the value of the virtual resistance, R_v, is chosen such that the bandwidth of the LPF meets the design requirements of the outer loop. It should be kept in mind that the bandwidth of this outer loop should be small enough to avoid interactions with the inner ac current loop, yet large enough for better controller performance. The parameters for the virtual impedance are

shown in Table 4.3, such that the resulting bandwidth is 31.4 Hz, about a tenth of the ac current loop bandwidth.

Table 4.3: Parameters of the Virtual Impedance Loop

L_v	34.664 mH
R_v	0.0653 Ω

4.4 Reactive Power Control Modes

As designed for the grid-tracking control scheme, the grid-forming scheme also implements reactive power control in accordance to the IEEE 1547-2018 Standard [33]. Once again, the three modes of active and reactive power compensation considered for the grid-tracking scheme is also considered for grid-forming. However, unlike the grid-tracking scheme, the d- and q-channel currents are not used to independently control the active and reactive power control. Recall that the basis of the grid-forming control scheme is to emulate a virtual synchronous machine in which the active power injection is based on the connected load in addition to the power required to align the grid and controller dq frames. Therefore, the active power is controlled in the power-balance synchronization loop, as derived in section 4.2, and the reactive power reference should be connected to the internal voltage reference, e, in the virtual impedance loop from the previous section. In fact, the deviation of the reactive power can be used to generate the internal voltage reference [11, 24].

4.4.1 Fixed Reactive Power

Under fixed reactive power mode, the inverter injects a set amount of reactive power according to some set point in the same manner as the grid-tracking control scheme. This reactive power controller (RPC) implements the same structure as discussed in [15] and [16] where a PI regulator is used to eliminate the deviation of the measured reactive power from

the set point, as shown in Fig. 4.13. It is clear to see that the structure of this control loop is nearly identical to that in Fig. 3.13 with the exception of the generated reference variable. The PI gains for the reactive power control loop are shown in Table 4.4.

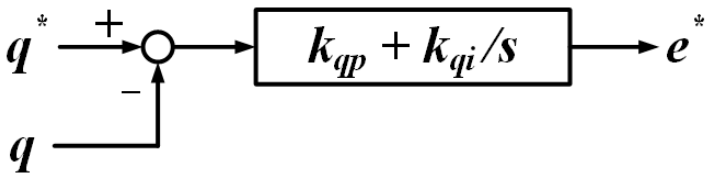

Figure 4.13: Reactive power controller for grid-forming control.

Table 4.4: Grid-tracking Reactive Power Loop PI Gains

k_{qp}	1.2×10^{-6}
k_{qi}	0.0012

From Fig. 4.13, the internal voltage reference is

$$e^* = \left(k_{pq} + \frac{k_{iq}}{s}\right)(q^* - q) \tag{4.39}$$

from which the small-signal expression for e^* is

$$\tilde{e}^* = G_{qs}\left(0 + V_{gd}^c \tilde{i}_{gq}^c + I_{gq}^c \tilde{v}_{gd}^c - V_{gq}^c \tilde{i}_{gd}^c - I_{gd}^c \tilde{v}_{gq}^c\right) \tag{4.40}$$

$$\Rightarrow \tilde{e}^* = \begin{bmatrix} -G_{qs}V_{gq}^c & G_{qs}V_{gd}^c \end{bmatrix} \begin{bmatrix} \tilde{i}_{gd}^c \\ \tilde{i}_{gq}^c \end{bmatrix} + \begin{bmatrix} G_{qs}I_{gq}^c & -G_{qs}I_{gd}^c \end{bmatrix} \begin{bmatrix} \tilde{v}_{gd}^c \\ \tilde{v}_{gq}^c \end{bmatrix} \tag{4.41}$$

where

$$G_{qs} = k_{pq} + \frac{k_{iq}}{s}$$

Taking into consideration that the q-channel internal voltage reference is set to 0, then

$$\mathbf{e} = \begin{bmatrix} \tilde{e}^* \\ 0 \end{bmatrix} = \mathbf{G_{ciq}} \begin{bmatrix} \tilde{i}^c_{gd} \\ \tilde{i}^c_{gq} \end{bmatrix} + \mathbf{G_{cvq}} \begin{bmatrix} \tilde{v}^c_{gd} \\ \tilde{v}^c_{gq} \end{bmatrix} \tag{4.42}$$

where

$$\mathbf{G_{ciq}} = \begin{bmatrix} -G_{qs}V^c_{gq} & G_{qs}V^c_{gd} \\ 0 & 0 \end{bmatrix} \quad \text{and} \quad \mathbf{G_{cvq}} = \begin{bmatrix} G_{qs}I^c_{gq} & -G_{qs}I^c_{gd} \\ 0 & 0 \end{bmatrix}$$

The fixed reactive power controller is incorporated in the small-signal model of the grid-forming controller as shown, in black, in Fig. 4.14.

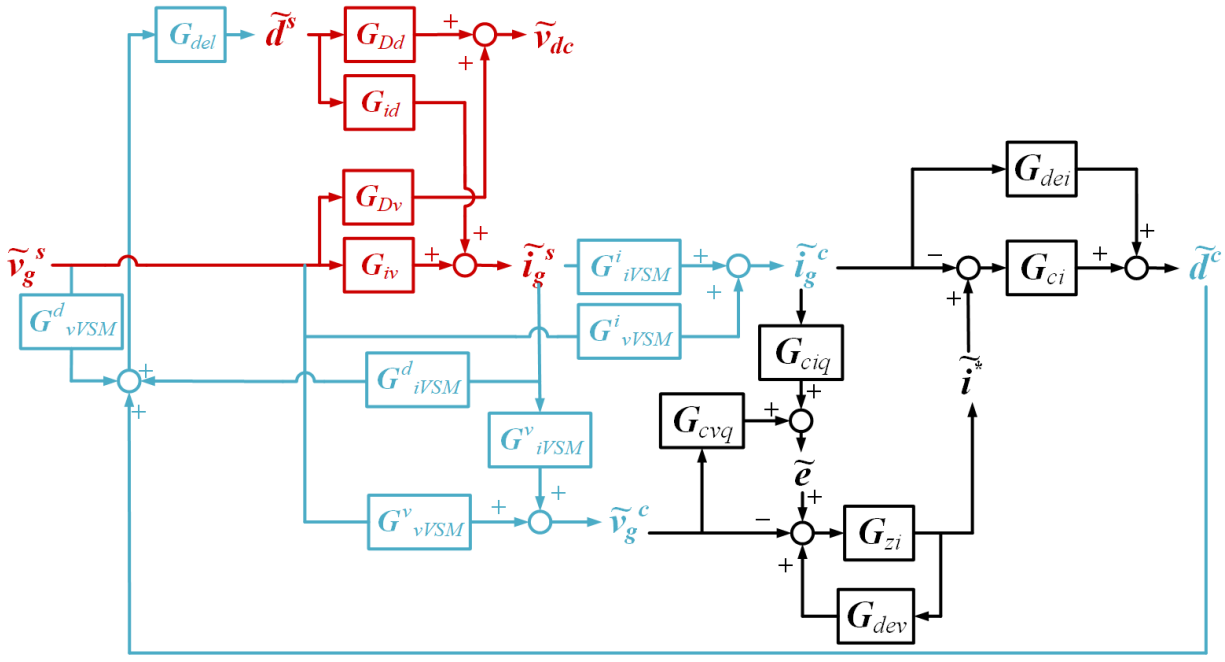

Figure 4.14: Small-signal model with reactive power control for grid-forming control.

4.4.2 Voltage-Reactive Power Mode

Finally, the dynamic reactive power controller is also considered for the grid-forming controller. Consider that the inverter operates in the inductive region of the volt-var curve discussed in 3.3.2. Unlike the grid-tracking case, where only the d-channel of the measured voltage passed to the controller, v_{gd}^c, was taken as an input to the droop curve, the grid-forming control takes the magnitude of the measured voltage as an input. The reason for this is due to the coupling from the virtual impedance. Although a decoupling term is introduced in the control scheme, it does not completely remove the dependency of the two channels in the synchronous frame; therefore, it is necessary to consider both the d- and q-channel components of the measured voltage passed to the controller. The droop function from (3.49) is rewritten as

$$q^* = \begin{cases} Q_{max} & K = \frac{\Delta Q}{\Delta V} & V < V1 \\ \left(\frac{Q_{max}}{V1-V2}\right)\left(\sqrt{{v_{gd}^c}^2 + {v_{gq}^c}^2} - V1\right) + Q_{max} & K = \frac{\Delta Q}{\Delta V} = \frac{Q_{max}}{V1-V2} & V1 < V \leq V2 \\ 0 & K = \frac{\Delta Q}{\Delta V} = 0 & V2 < V \leq V3 \\ \left(\frac{Q_{max}}{V3-V4}\right)\left(\sqrt{{v_{gd}^c}^2 + {v_{gq}^c}^2} - V3\right), & K = \frac{\Delta Q}{\Delta V} = \frac{Q_{max}}{V3-V4} & V3 < V \leq V4 \\ -Q_{max} & K = \frac{\Delta Q}{\Delta V} = 0 & V > V4 \end{cases} \tag{4.43}$$

where K is the slope of the droop curve. Consider that the ac bus voltage is once again measured to be between $V3$ and $V4$ such that the inverter operates in the inductive region of the droop curve. Then, by (4.43),

$$q^* = K\left[\left(\sqrt{{v_{gd}^c}^2 + {v_{gq}^c}^2}\right) - V3\right], \qquad K = \left(\frac{Q_{max}}{V3 - V4}\right) \tag{4.44}$$

Substituting (4.44) into (4.39) and expressing the measured reactive power in terms of the measured voltage and current passed to the controller yields

$$e^* = G_{qs}K\sqrt{{v_{gd}^c}^2 + {v_{gq}^c}^2} - G_{qs}KV3 + G_{qs}v_{gd}^c i_{gq}^c - G_{qs}v_{gq}^c i_{gd}^c \tag{4.45}$$

In order to include the volt-var controller in the small-signal model of the grid-forming controller, then the small-signal expression for (4.45) must be derived. Due to the nonlinear term, $\sqrt{{v_{gd}^c}^2 + {v_{gq}^c}^2}$, it is necessary to consider the full procedure in obtaining the small-signal expression for a equation of system of equations. Consider a differential-algebraic system of equations, $\mathbf{F}$, which is a function of a vector $\mathbf{x}$ such that

$$\mathbf{F} = \begin{bmatrix} f_1(\mathbf{x}) \\ f_2(\mathbf{x}) \\ \vdots \\ f_m(\mathbf{x}) \end{bmatrix} \tag{4.46}$$

and

$$\mathbf{x} = \begin{bmatrix} x_1 \\ x_2 \\ \vdots \\ x_n \end{bmatrix} \tag{4.47}$$

Then, for a specific operating point, $\mathbf{x}_0$, then the small-signal expression of $\mathbf{F}$ is expressed as

$$\frac{d\tilde{\mathbf{F}}}{dt} = J_{\mathbf{F}}|_{\mathbf{x}=\mathbf{x}_0} * \tilde{\mathbf{x}} \tag{4.48}$$

where $\tilde{\mathbf{x}}$ is the small-signal perturbation of $\mathbf{x}$ and $J_{\mathbf{F}}$ is the Jacobian function which takes the partial derivative of each differential equation with respect to the vector $\mathbf{x}$ such that

$$J_{\mathbf{F}} = \frac{\partial F}{\partial \mathbf{X}} = \begin{bmatrix} \frac{\partial f_1}{\partial x_1} & \cdots & \frac{\partial f_1}{\partial x_n} \\ \vdots & \ddots & \vdots \\ \frac{\partial f_m}{\partial x_1} & \cdots & \frac{\partial f_m}{\partial x_n} \end{bmatrix} \tag{4.49}$$

Thus,

$$\frac{d\tilde{\mathbf{F}}}{dt} = \begin{bmatrix} \frac{\partial f_1}{\partial x_1} & \cdots & \frac{\partial f_1}{\partial x_n} \\ \vdots & \ddots & \vdots \\ \frac{\partial f_m}{\partial x_1} & \cdots & \frac{\partial f_m}{\partial x_n} \end{bmatrix} \Bigg|_{\mathbf{x}=\mathbf{x}_0} \tilde{\mathbf{x}} \tag{4.50}$$

For example, the small-signal expression of the first function is

$$\frac{d\tilde{f}_1}{dt} = \frac{\partial f_1}{\partial x_1}\Big|_{\mathbf{x}=\mathbf{x}_0} \tilde{x}_1 + \frac{\partial f_1}{\partial x_2}\Big|_{\mathbf{x}=\mathbf{x}_0} \tilde{x}_2 + ... + \frac{\partial f_1}{\partial x_n}\Big|_{\mathbf{x}=\mathbf{x}_0} \tilde{x}_n \tag{4.51}$$

The small-signal expression of the internal voltage in (4.45) is derived using the following setup

$$\tilde{e}^* = \frac{\partial e^*}{\partial i^c_{gd}}\Big|_{\mathbf{x}=\mathbf{x}_0} \tilde{i}^c_{gd} + \frac{\partial e^*}{\partial i^c_{gq}}\Big|_{\mathbf{x}=\mathbf{x}_0} \tilde{i}^c_{gq} + \frac{\partial e^*}{\partial v^c_{gd}}\Big|_{\mathbf{x}=\mathbf{x}_0} \tilde{v}^c_{gd} + \frac{\partial e^*}{\partial v^c_{gq}}\Big|_{\mathbf{x}=\mathbf{x}_0} \tilde{v}^c_{gq} \tag{4.52}$$

The first two terms can easily be derived due to their linear characteristics such that

$$\tilde{e}^* = -G_{qs} V^c_{gq} \tilde{i}^c_{gd} + G_{qs} V^c_{gd} \tilde{i}^c_{gq} + \frac{\partial e^*}{\partial v^c_{gd}}\Big|_{\mathbf{x}=\mathbf{x}_0} \tilde{v}^c_{gd} + \frac{\partial e^*}{\partial v^c_{gq}}\Big|_{\mathbf{x}=\mathbf{x}_0} \tilde{v}^c_{gq} \tag{4.53}$$

However, the last two terms contain the nonlinear term, which is a function of v_{gd}^c and v_{gq}^c. Consider only the third term; the expression to be derived is

$$\left.\frac{\partial e^*}{\partial v_{gd}^c}\right|_{\mathbf{x}=\mathbf{x}_0} = \left.\frac{\partial}{\partial v_{gd}^c}\right|_{\mathbf{x}=\mathbf{x}_0} \left(G_{qs}K\sqrt{{v_{gd}^c}^2 + {v_{gq}^c}^2} + G_{qs}v_{gd}^c i_{gq}^c\right) \tag{4.54}$$

Using calculus

$$\left.\frac{\partial e^*}{\partial v_{gd}^c}\right|_{\mathbf{x}=\mathbf{x}_0} = \left.\frac{\partial}{\partial v_{gd}^c}\right|_{\mathbf{x}=\mathbf{x}_0} \left(G_{qs}K\sqrt{{v_{gd}^c}^2 + {v_{gq}^c}^2}\right) + \left.\frac{\partial}{\partial v_{gd}^c}\right|_{\mathbf{x}=\mathbf{x}_0} \left(G_{qs}v_{gd}^c i_{gq}^c\right) \tag{4.55}$$

$$= G_{qs}K\left.\frac{\partial}{\partial v_{gd}^c}\right|_{\mathbf{x}=\mathbf{x}_0} \sqrt{{v_{gd}^c}^2 + {v_{gq}^c}^2} + G_q s\left.\frac{\partial}{\partial v_{gd}^c}\right|_{\mathbf{x}=\mathbf{x}_0} v_{gd}^c i_{gq}^c \tag{4.56}$$

$$= G_{qs}K \cdot \frac{1}{2\sqrt{{V_{gd}^c}^2 + {V_{gq}^c}^2}} \cdot 2V_{gd}^c + G_{qs}I_{gq}^c \tag{4.57}$$

$$= \frac{G_{qs}K}{\sqrt{{V_{gd}^c}^2 + {V_{gq}^c}^2}} + G_{qs}I_{gq}^c \tag{4.58}$$

Applying the same procedure to the fourth term in (4.53), the resulting small-signal expression is

$$\begin{aligned}\tilde{e}^* = &\left(-G_{qs}V_{gq}^c\right)\tilde{i}_{gd}^c + \left(G_{qs}V_{gd}^c\right)\tilde{i}_{gq}^c \\ &+ \left(\frac{G_{qs}KV_{gd}^c}{\sqrt{{V_{gd}^c}^2 + {V_{gq}^c}^2}} + G_{qs}I_{gq}^c\right)\tilde{v}_{gd}^c + \left(\frac{G_{qs}KV_{gd}^c}{\sqrt{{V_{gd}^c}^2 + {V_{gq}^c}^2}} - G_{qs}I_{gd}^c\right)\tilde{v}_{gq}^c\end{aligned} \tag{4.59}$$

Therefore, the expression for the small-signal internal voltage reference is

$$\mathbf{e} = \begin{bmatrix}\tilde{e}^* \\ 0\end{bmatrix} = \mathbf{G_{ciq}}\begin{bmatrix}\tilde{i}_{gd}^c \\ \tilde{i}_{gq}^c\end{bmatrix} + \mathbf{G_{cvq}}\begin{bmatrix}\tilde{v}_{gd}^c \\ \tilde{v}_{gq}^c\end{bmatrix} \tag{4.60}$$

where

$$\mathbf{G_{ciq}} = \begin{bmatrix} -G_{qs}V_{gq}^{c} & G_{qs}V_{gd}^{c} \\ 0 & 0 \end{bmatrix} \quad \text{and} \quad \mathbf{G_{cvq}} = \begin{bmatrix} \frac{G_{qs}KV_{gd}^{c}}{\sqrt{{V_{gd}^{c}}^{2}+{V_{gq}^{c}}^{2}}} + G_{qs}I_{gq}^{c} & \frac{G_{qs}KV_{gd}^{c}}{\sqrt{{V_{gd}^{c}}^{2}+{V_{gq}^{c}}^{2}}} - G_{qs}I_{gd}^{c} \\ 0 & 0 \end{bmatrix}$$

The expression for $\tilde{e}^{*}$ is the same as that found in 3.3.1, where the difference lies in the matrices $\mathbf{G}_{ciq}$ and $\mathbf{G}_{cvq}$. Therefore, the same small-signal model from Fig. 4.14 can be used for all modes of operation.

4.5 Terminal Ac Impedance for Grid-Forming Control

The *dq* ac impedance of the inverter with grid-forming control is derived from solving the equations in (4.61), which are obtained from the small-signal model in Fig. 4.14.

$$\begin{cases} \tilde{\mathbf{i}}^{*} = \left(\mathbf{I} - \mathbf{G_{zi}}\mathbf{G_{dev}}\right)^{-1}\mathbf{G_{zi}}\left(\tilde{\mathbf{e}} - \tilde{\mathbf{v}}_{\mathbf{g}}^{\mathbf{c}}\right) \\ \tilde{\mathbf{v}}_{\mathbf{g}}^{\mathbf{c}} = \mathbf{G}_{\mathbf{vVSM}}^{\mathbf{v}}\tilde{\mathbf{v}}_{\mathbf{g}}^{\mathbf{s}} + \mathbf{G}_{\mathbf{iVSM}}^{\mathbf{v}}\tilde{\mathbf{i}}_{\mathbf{g}}^{\mathbf{s}} \\ \tilde{\mathbf{i}}_{\mathbf{g}}^{\mathbf{c}} = \mathbf{G}_{\mathbf{vVSM}}^{\mathbf{i}}\tilde{\mathbf{v}}_{\mathbf{g}}^{\mathbf{s}} + \mathbf{G}_{\mathbf{iVSM}}^{\mathbf{i}}\tilde{\mathbf{i}}_{\mathbf{g}}^{\mathbf{s}} \\ \tilde{\mathbf{e}}^{*} = \mathbf{G_{cvq}}\tilde{\mathbf{v}}_{\mathbf{g}}^{\mathbf{c}} + \mathbf{G_{ciq}}\tilde{\mathbf{i}}_{\mathbf{g}}^{\mathbf{c}} \\ \tilde{\mathbf{d}}^{\mathbf{c}} = \mathbf{G_{ci}}\left(\tilde{\mathbf{i}}^{*} - \tilde{\mathbf{i}}_{\mathbf{g}}^{\mathbf{c}}\right) + \mathbf{G_{dei}}\tilde{\mathbf{i}}_{\mathbf{g}}^{\mathbf{c}} \\ \tilde{\mathbf{d}}^{\mathbf{s}} = \mathbf{G_{del}}\left(\tilde{\mathbf{d}}^{\mathbf{c}} + \mathbf{G}_{\mathbf{vVSM}}^{\mathbf{d}}\tilde{\mathbf{v}}_{\mathbf{g}}^{\mathbf{s}} + \mathbf{G}_{\mathbf{iVSM}}^{\mathbf{d}}\tilde{\mathbf{i}}_{\mathbf{g}}^{\mathbf{s}}\right) \\ \tilde{\mathbf{i}}_{\mathbf{g}}^{\mathbf{s}} = \mathbf{G_{iv}}\tilde{\mathbf{v}}_{\mathbf{g}}^{\mathbf{s}} + \mathbf{G_{id}}\tilde{\mathbf{d}}^{\mathbf{s}} \end{cases} \tag{4.61}$$

In order to derive the terminal *dq* ac impedance of the PV inverter for each mode of operation for the grid-forming control, $\tilde{\mathbf{e}}^{*}$ and $\tilde{\mathbf{v}}_{\mathbf{g}}^{\mathbf{c}}$ are first substituted into $\tilde{\mathbf{i}}^{*}$ such that

$$\tilde{\mathbf{i}}^{*} = \left(\mathbf{I} - \mathbf{G_{iz}}\mathbf{G_{dev}}\right)^{-1}\mathbf{G_{zi}}\left(\mathbf{G_{cvq}}\tilde{\mathbf{v}}_{\mathbf{g}}^{\mathbf{c}} + \mathbf{G_{ciq}}\tilde{\mathbf{i}}_{\mathbf{g}}^{\mathbf{c}} - \mathbf{G}_{\mathbf{vVSM}}^{\mathbf{v}}\tilde{\mathbf{v}}_{\mathbf{g}}^{\mathbf{s}} - \mathbf{G}_{\mathbf{iVSM}}^{\mathbf{v}}\tilde{\mathbf{i}}_{\mathbf{g}}^{\mathbf{s}}\right) \tag{4.62}$$

Substituting for $\tilde{\mathbf{i}}_{\mathbf{g}}^{\mathbf{c}}$ and combining like-terms

$$\begin{aligned}\tilde{\mathbf{i}}^{*} = &\left(\mathbf{I}-\mathbf{G_{iz}}\mathbf{G_{dev}}\right)^{-1}\mathbf{G_{zi}}\left(\mathbf{G_{cvq}}\mathbf{G}_{\mathbf{vVSM}}^{\mathbf{v}}+\mathbf{G_{ciq}}\mathbf{G}_{\mathbf{vVSM}}^{\mathbf{i}}-\mathbf{G}_{\mathbf{vVSM}}^{\mathbf{v}}\right)\tilde{\mathbf{v}}_{\mathbf{g}}^{\mathbf{s}}+\\ &\left(\mathbf{I}-\mathbf{G_{iz}}\mathbf{G_{dev}}\right)^{-1}\mathbf{G_{zi}}\left(\mathbf{G_{cvq}}\mathbf{G}_{\mathbf{iVSM}}^{\mathbf{v}}+\mathbf{G_{ciq}}\mathbf{G}_{\mathbf{iVSM}}^{\mathbf{i}}-\mathbf{G}_{\mathbf{iVSM}}^{\mathbf{v}}\right)\tilde{\mathbf{i}}_{\mathbf{g}}^{\mathbf{s}}\end{aligned} \tag{4.63}$$

Next, $\tilde{\mathbf{i}}^{*}$ and $\tilde{\mathbf{i}}_{\mathbf{g}}^{\mathbf{c}}$ are substituted into $\tilde{\mathbf{d}}^{\mathbf{c}}$ so that, after combining like-terms,

$$\begin{aligned}\tilde{\mathbf{d}}^{\mathbf{c}} = &\left[\mathbf{G_{ci}}\left(\mathbf{I}-\mathbf{G_{iz}}\mathbf{G_{dev}}\right)^{-1}\mathbf{G_{zi}}\left(\mathbf{G_{cvq}}\mathbf{G}_{\mathbf{vVSM}}^{\mathbf{v}}+\mathbf{G_{ciq}}\mathbf{G}_{\mathbf{vVSM}}^{\mathbf{i}}-\mathbf{G}_{\mathbf{vVSM}}^{\mathbf{v}}\right)+\left(\mathbf{G_{dei}}-\mathbf{G_{ci}}\right)\mathbf{G}_{\mathbf{vVSM}}^{\mathbf{i}}\right]\tilde{\mathbf{v}}_{\mathbf{g}}^{\mathbf{s}}+\\ &\left[\mathbf{G_{ci}}\left(\mathbf{I}-\mathbf{G_{iz}}\mathbf{G_{dev}}\right)^{-1}\mathbf{G_{zi}}\left(\mathbf{G_{cvq}}\mathbf{G}_{\mathbf{iVSM}}^{\mathbf{v}}+\mathbf{G_{ciq}}\mathbf{G}_{\mathbf{iVSM}}^{\mathbf{i}}-\mathbf{G}_{\mathbf{iVSM}}^{\mathbf{v}}\right)+\left(\mathbf{G_{dei}}-\mathbf{G_{ci}}\right)\mathbf{G}_{\mathbf{iVSM}}^{\mathbf{i}}\right]\tilde{\mathbf{i}}_{\mathbf{g}}^{\mathbf{s}}\end{aligned} \tag{4.64}$$

Then, $\tilde{\mathbf{d}}^{\mathbf{c}}$ is substituted into $\tilde{\mathbf{d}}^{\mathbf{s}}$ and like-terms are combined to obtain

$$\begin{aligned}\tilde{\mathbf{d}}^{\mathbf{c}} = &\mathbf{G_{del}}\Big\{\mathbf{G_{ci}}\left(\mathbf{I}-\mathbf{G_{iz}}\mathbf{G_{dev}}\right)^{-1}\mathbf{G_{zi}}\left(\mathbf{G_{cvq}}\mathbf{G}_{\mathbf{vVSM}}^{\mathbf{v}}+\mathbf{G_{ciq}}\mathbf{G}_{\mathbf{vVSM}}^{\mathbf{i}}-\mathbf{G}_{\mathbf{vVSM}}^{\mathbf{v}}\right)+\\ &\left(\mathbf{G_{dei}}-\mathbf{G_{ci}}\right)\mathbf{G}_{\mathbf{vVSM}}^{\mathbf{i}}+\mathbf{G}_{\mathbf{vVSM}}^{\mathbf{d}}\Big\}\tilde{\mathbf{v}}_{\mathbf{g}}^{\mathbf{s}}+\\ &\mathbf{G_{del}}\Big\{\mathbf{G_{ci}}\left(\mathbf{I}-\mathbf{G_{iz}}\mathbf{G_{dev}}\right)^{-1}\mathbf{G_{zi}}\left(\mathbf{G_{cvq}}\mathbf{G}_{\mathbf{iVSM}}^{\mathbf{v}}+\mathbf{G_{ciq}}\mathbf{G}_{\mathbf{iVSM}}^{\mathbf{i}}-\mathbf{G}_{\mathbf{iVSM}}^{\mathbf{v}}\right)+\\ &\left(\mathbf{G_{dei}}-\mathbf{G_{ci}}\right)\mathbf{G}_{\mathbf{iVSM}}^{\mathbf{i}}+\mathbf{G}_{\mathbf{iVSM}}^{\mathbf{d}}\Big\}\tilde{\mathbf{i}}_{\mathbf{g}}^{\mathbf{s}}\end{aligned} \tag{4.65}$$

Finally, $\tilde{\mathbf{d}}^{\mathbf{s}}$ is substituted into $\tilde{\mathbf{i}}_{\mathbf{g}}^{\mathbf{s}}$, from which resulting terminal dq ac impedance of the PV inverter for each mode of operation can be expressed by one equations as follows:

$$\begin{aligned}\mathbf{Z} = \frac{\tilde{\mathbf{v}}_{\mathbf{g}}^{\mathbf{s}}}{-\tilde{\mathbf{i}}_{\mathbf{g}}^{\mathbf{s}}} = &-\Big(\mathbf{G_{iv}}+\mathbf{G_{id}}\mathbf{G_{del}}\Big[\mathbf{G_{ci}}\left(\mathbf{I}-\mathbf{G_{zi}}\mathbf{G_{dev}}\right)^{-1}\mathbf{G_{zi}}\left(\mathbf{G_{cvq}}\mathbf{G}_{\mathbf{vVSM}}^{\mathbf{v}}+\mathbf{G_{ciq}}\mathbf{G}_{\mathbf{vVSM}}^{\mathbf{i}}-\mathbf{G}_{\mathbf{vVSM}}^{\mathbf{v}}\right)+\\ &\left(\mathbf{G_{dei}}-\mathbf{G_{ci}}\right)\mathbf{G}_{\mathbf{iVSM}}^{\mathbf{i}}+\mathbf{G}_{\mathbf{vVSM}}^{\mathbf{d}}\Big]\Big)^{-1}\cdot\\ &\Big(\mathbf{I}-\mathbf{G_{id}}\mathbf{G_{del}}\Big[\mathbf{G_{ci}}\left(\mathbf{I}-\mathbf{G_{zi}}\mathbf{G_{dev}}\right)^{-1}\mathbf{G_{zi}}\left(\mathbf{G_{cvq}}\mathbf{G}_{\mathbf{iVSM}}^{\mathbf{v}}+\mathbf{G_{ciq}}\mathbf{G}_{\mathbf{iVSM}}^{\mathbf{i}}-\mathbf{G}_{\mathbf{iVSM}}^{\mathbf{v}}\right)+\\ &\left(\mathbf{G_{dei}}-\mathbf{G_{ci}}\right)\mathbf{G}_{\mathbf{iVSM}}^{\mathbf{i}}+\mathbf{G}_{\mathbf{iVSM}}^{\mathbf{d}}\Big]\Big)\end{aligned} \tag{4.66}$$

The derived impedance above is compared to the numerical linearization of the PV inverter using MATLAB Simulink for unity power factor, fixed reactive power, and volt-var modes in Figs. 4.15, 4.16, and 4.17, respectively. Under unity power factor, the inverter operates at $P = 250$ kW and $Q = 0$ kvar; under fixed reactive power and volt-var modes, the inverter operates at $P = 250$ kW and $Q = -75$ kvar. For each case, the derived closed form terminal ac impedance closely matches the numerical linearization. For each mode of operation, the terminal dq ac impedance is not diagonally dominant. A comparison of the impedance under each operating mode is shown in Fig. 4.18.

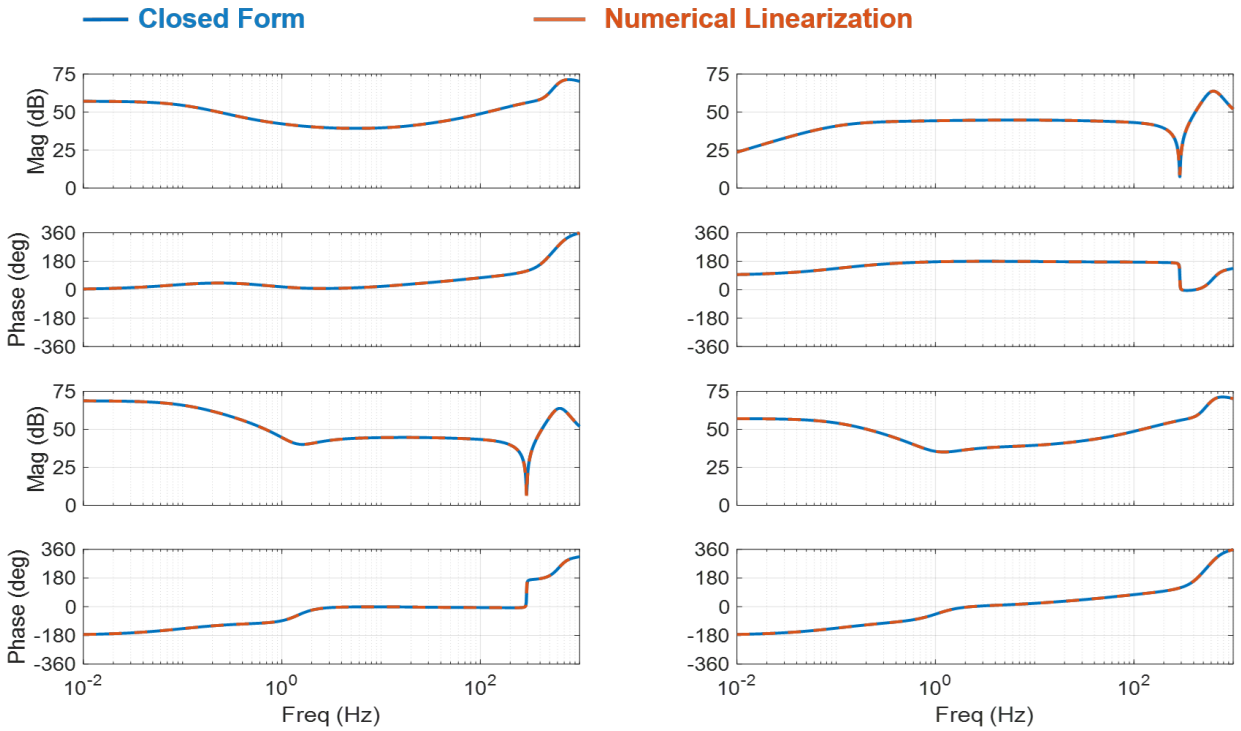

Figure 4.15: PV inverter terminal ac impedance under unity power factor mode for grid-forming control.

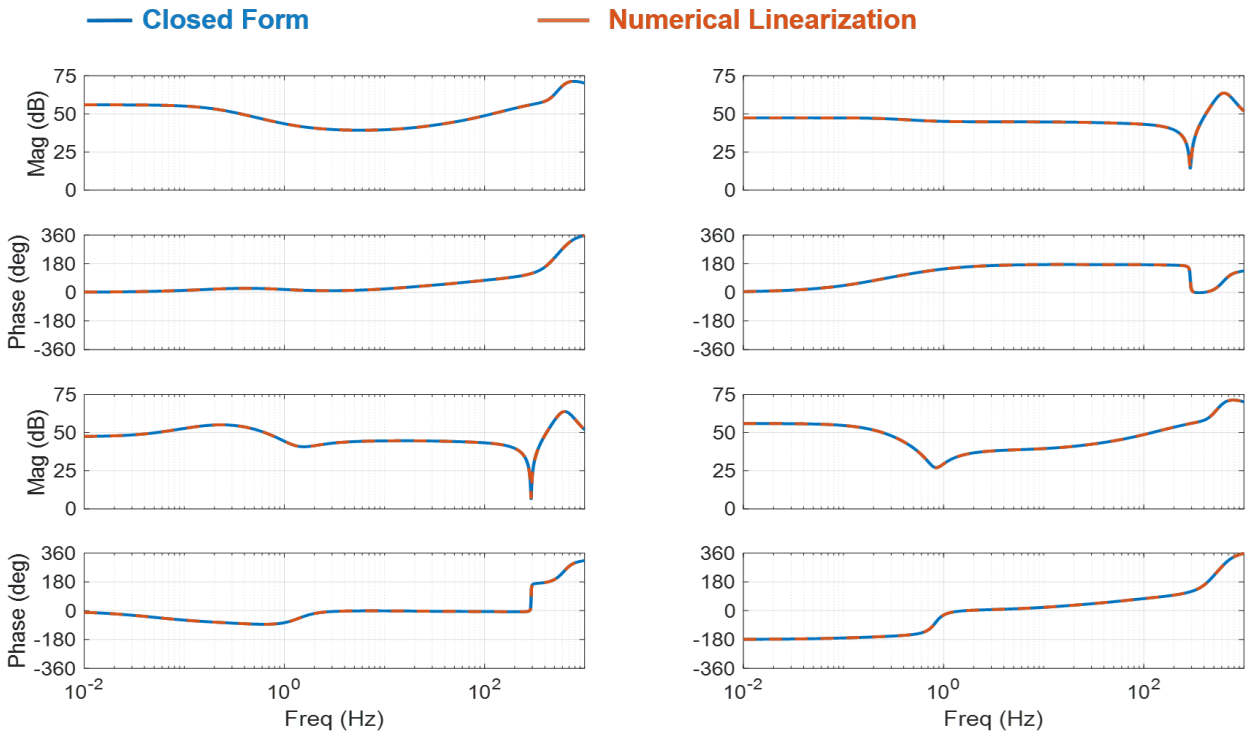

Figure 4.16: PV inverter terminal ac impedance under fixed reactive power mode for grid-forming control.

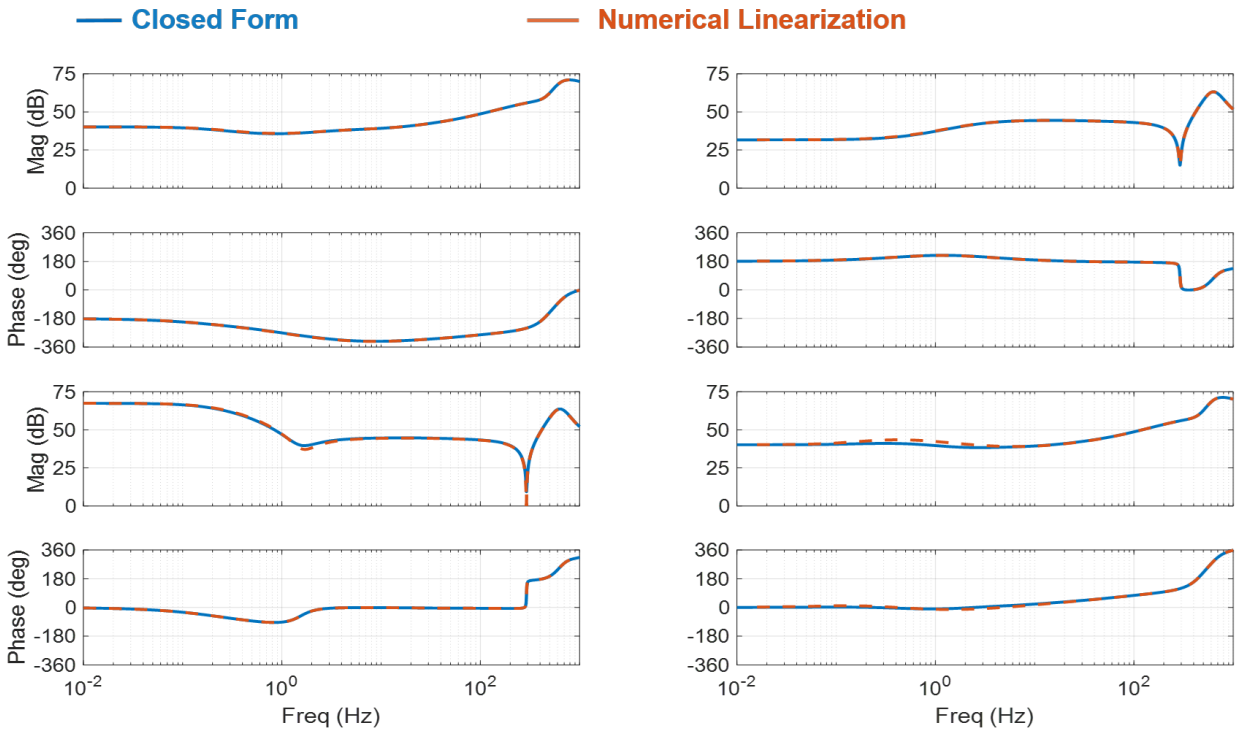

Figure 4.17: PV inverter terminal ac impedance under volt-var mode for grid-forming control.

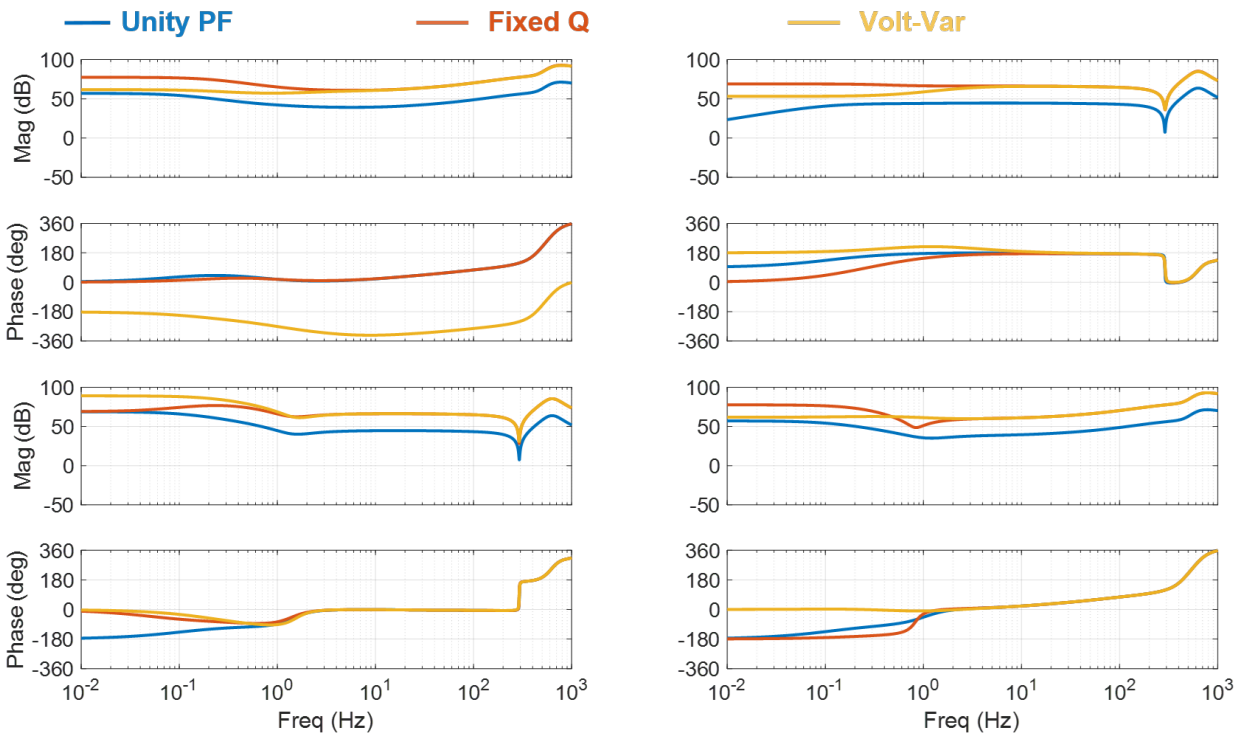

Figure 4.18: Comparison of terminal ac impedance with grid-forming control for different modes of operation.

4.5.1 Comparison to Grid-Tracking Control

One of the main points of this work is to compare the grid-tracking and grid-forming controllers in terms of their terminal dq ac impedance. Figs. 4.19, 4.20, and 4.21 compare the impedance of the grid-tracking control scheme from Ch. 3 to the grid-forming scheme from this chapter for unity power factor, fixed reactive power, and volt-var mode, respectively.

Under the grid-forming control scheme, the range of the negative incremental impedance in the Z_{qq} channel, for unity power factor and fixed reactive power, and Z_{dd}, for volt-var, is one to two decades lower than for the grid-tracking control scheme. This is indicative of a favorable, but not certain, condition for stability in the connection of the inverter to the grid. Additionally, for all modes of operation, the impedance of the grid-forming control is not diagonally dominant; in this regard, it is not possible to draw a conclusion on the stability of the connection. On the other hand, the grid-tracking control is diagonally dominant under unity power factor mode, and it is very likely that the connection is stable.

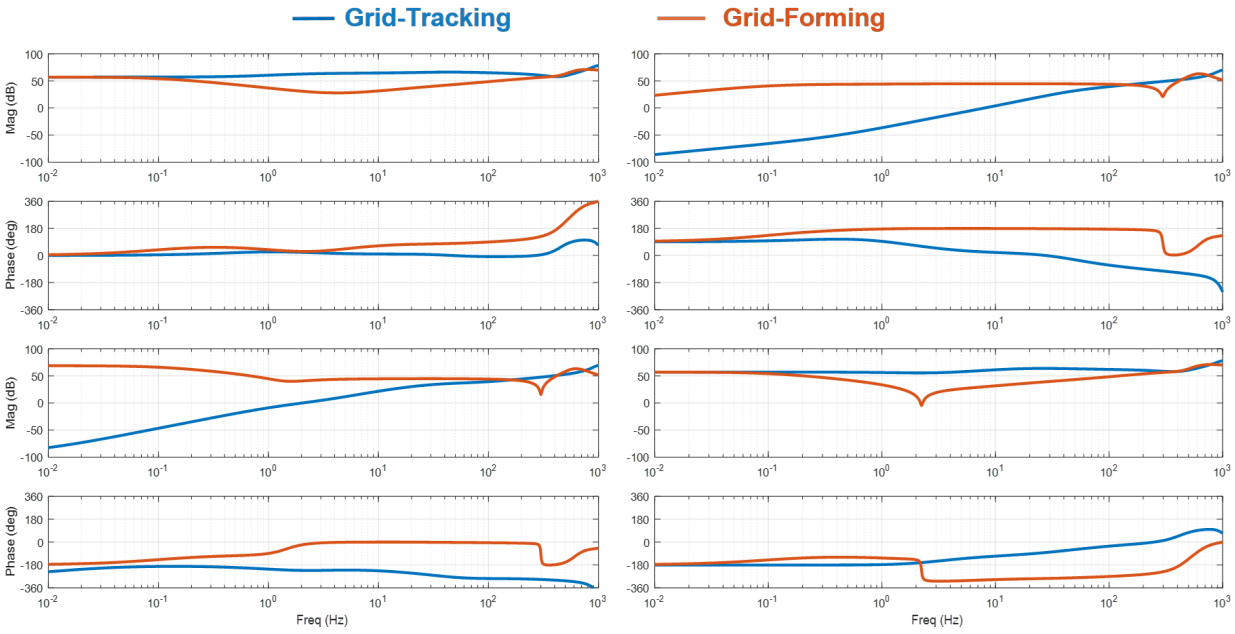

Figure 4.19: Terminal dq ac impedance comparison under unity power factor mode.

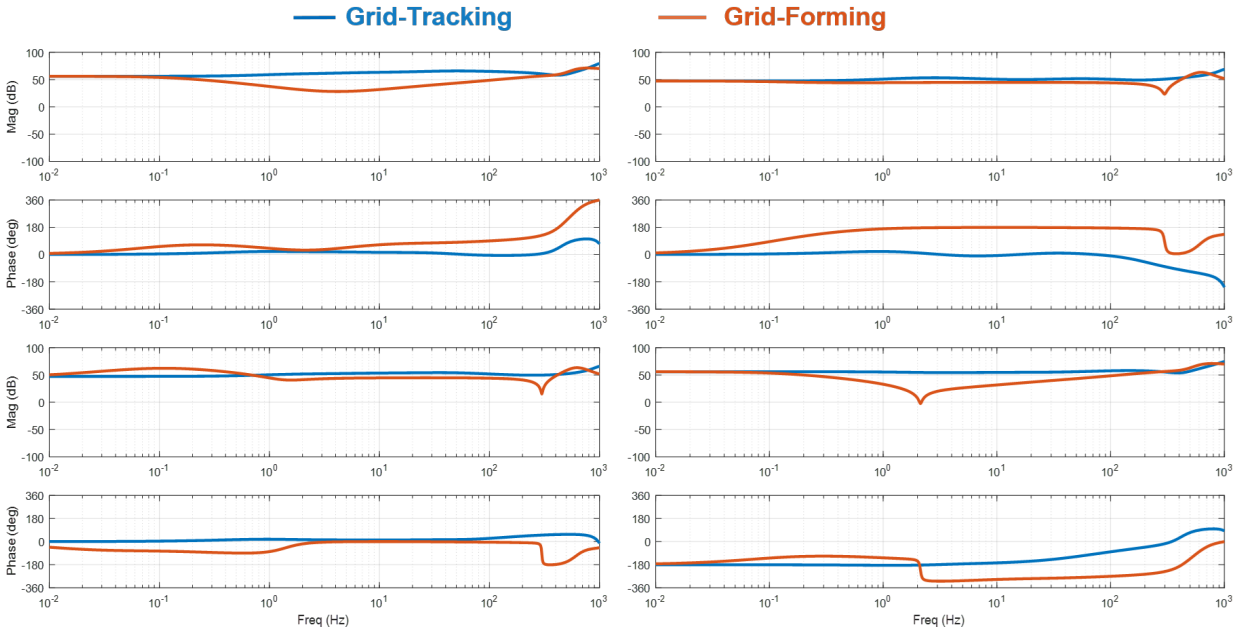

Figure 4.20: Terminal dq ac impedance comparison under fixed reactive power mode.

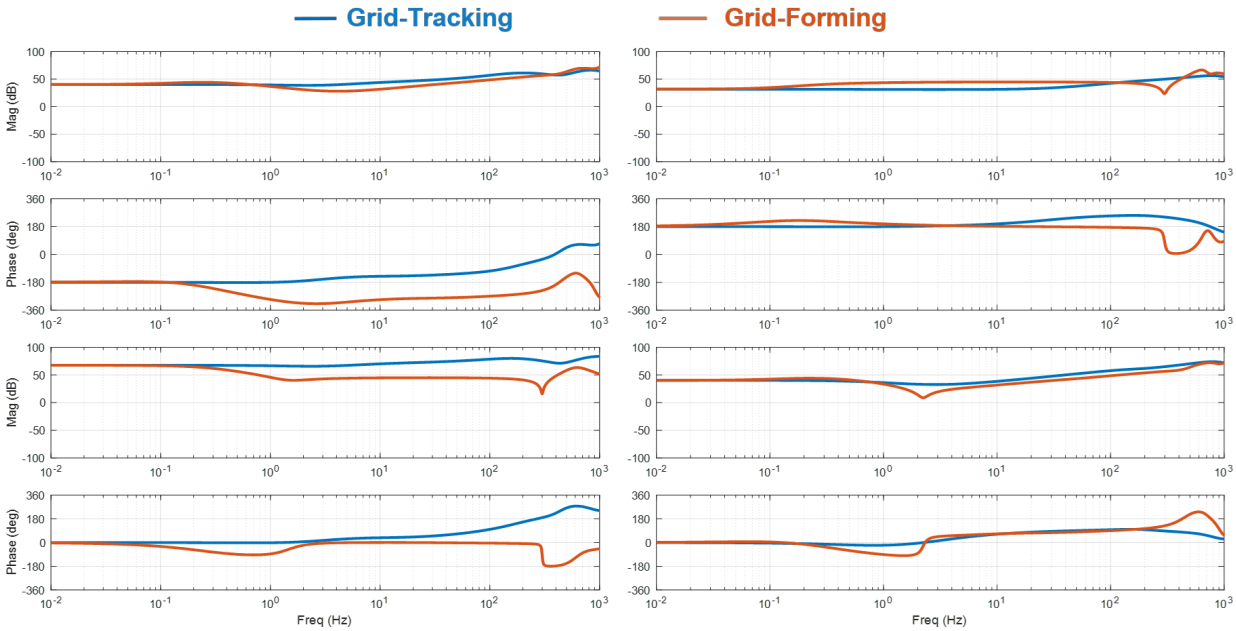

Figure 4.21: Terminal dq ac impedance comparison under volt-var mode.

4.6 Effect of Parameter Variation

The effect of varying control parameters is seen in the performance of the controller. For example, changing the PI gains in the ac current loop will affect the bandwidth of the inner

loop and, therefore, could introduce dynamic interactions with other control loops or with the switching of the inverter. Therefore, it is necessary to ensure that the parameters are chosen in such a manner to ensure the robustness of the controller. As the grid-forming controller emulates the nature of a synchronous machine, the inherent response due to the inertia can be observed, as well as the effect of changing the impedance. One of the benefits of this controller is the fact that the parameters are not limited by the physical capability of a machine and, instead, some parameters may be designed for values unattainable by a real synchronous machine. The aim of this section is to observe the effect of varying the parameters seen in a synchronous machine, including the inertia constant and impedance, on the terminal impedance derived in the previous section.

At low frequency, the power-balance synchronization loop affects the terminal dq ac impedance curve due to the low bandwdith of the control loop. Alternatively, at high frequency, the ac current controller affects the shape of the impedance curves. The outer control loops, primarly the virtual impedance loop, will affect the impedance at medium frequency. Consider Fig. 4.22 in which the inertia constant, H, from (4.23) is varied from 3 to 10 seconds under unity power factor mode. The impedance in all channels will be affected at the low frequency range; therefore, this parameter can be varied, in conjunction with the damping factor D, to shape the impedance.

On the other hand, varying the virtual impedance will affect the impedance at a higher frequency range compared to the variation of the inertia constant. The result of varying the virtual resistance, R_v, is shown in Fig. 4.23 while the result of varying the virtual inductance, L_v, is shown in Fig. 4.24. Varying the virtual resistance results in a relatively small effect on the impedance since the majority of the impedance of a machine is its reactance, which is a function of the inductance of the machine. In fact, the effect of varying the virtual

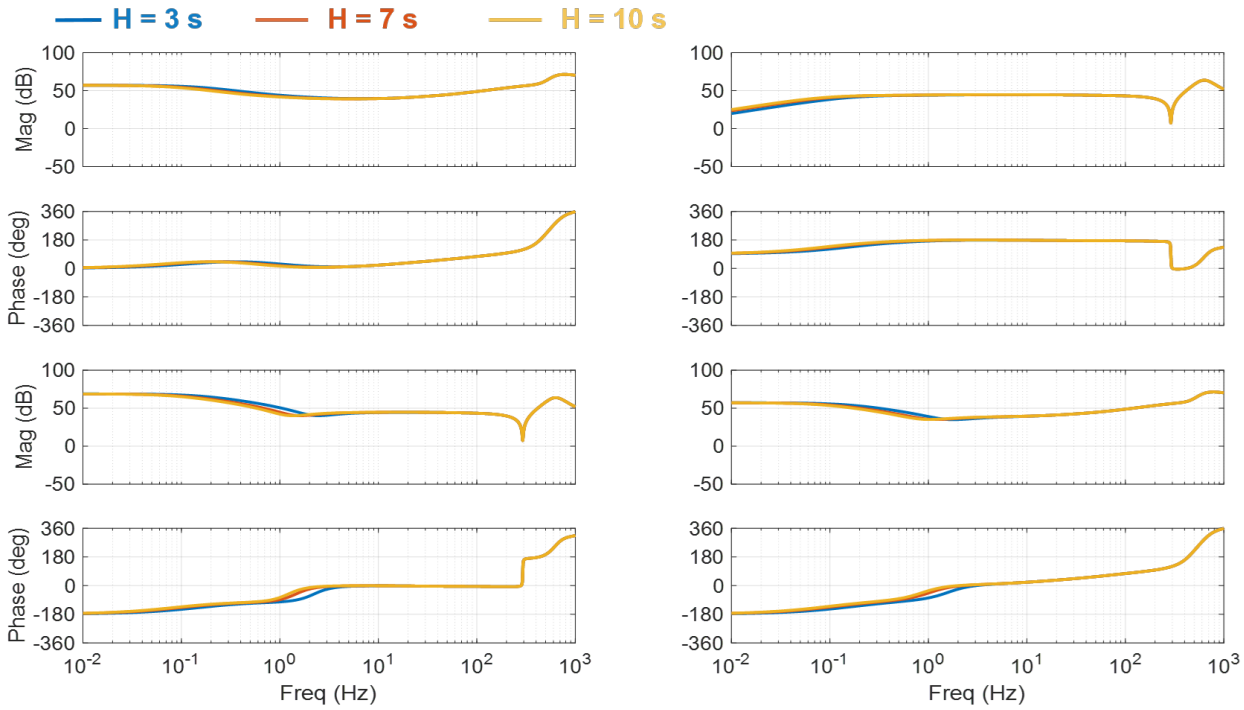

Figure 4.22: Variation of the power loop bandwidth under unity power factor.

inductance and, in turn, the virtual reactance, is far more significant. Not only does the variation of this single parameter affect the bandwidth of the virtual impedance outer loop, but it also considerably affects the magnitudes and phases of the terminal ac impedance, especially the range of the negative incremental resistance in the Z_{qq} channel, where a lower virtual inductance results in a smaller range. Coupling the variation of the virtual resistance and inductance, it is possible to shape the curve of the ac impedance to favor a stable case.

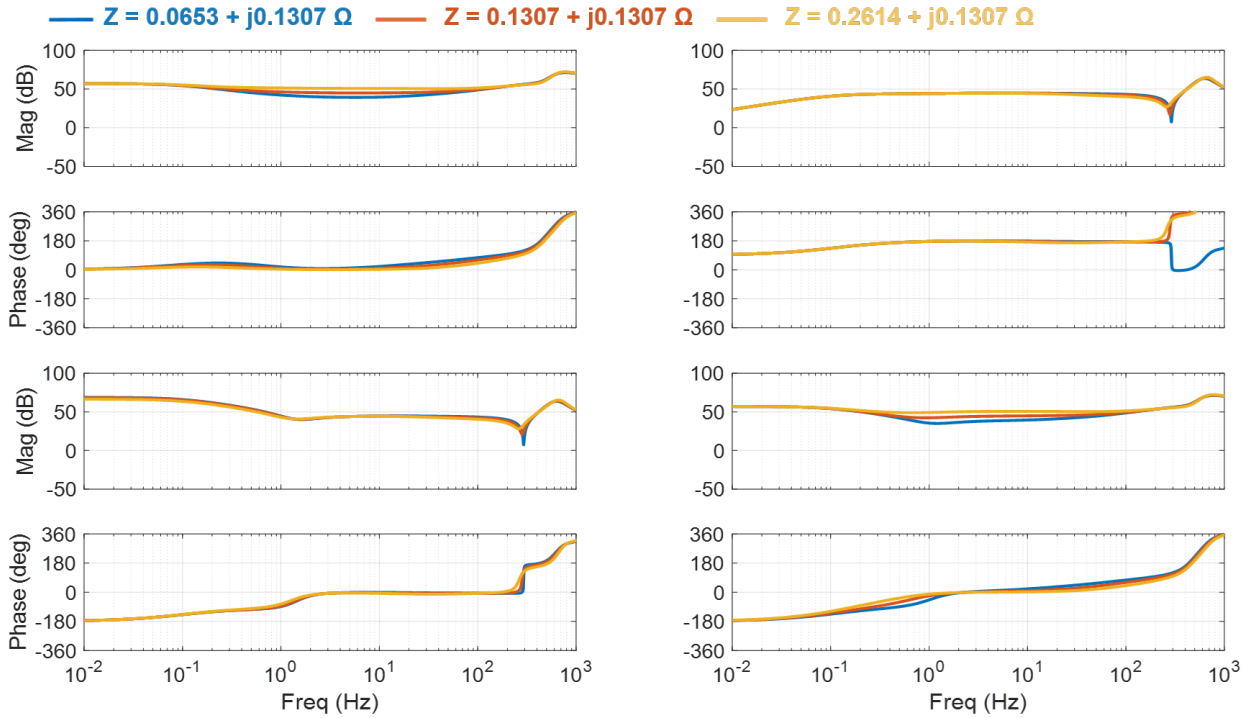

Figure 4.23: Variation of the virtual resistance under unity power factor.

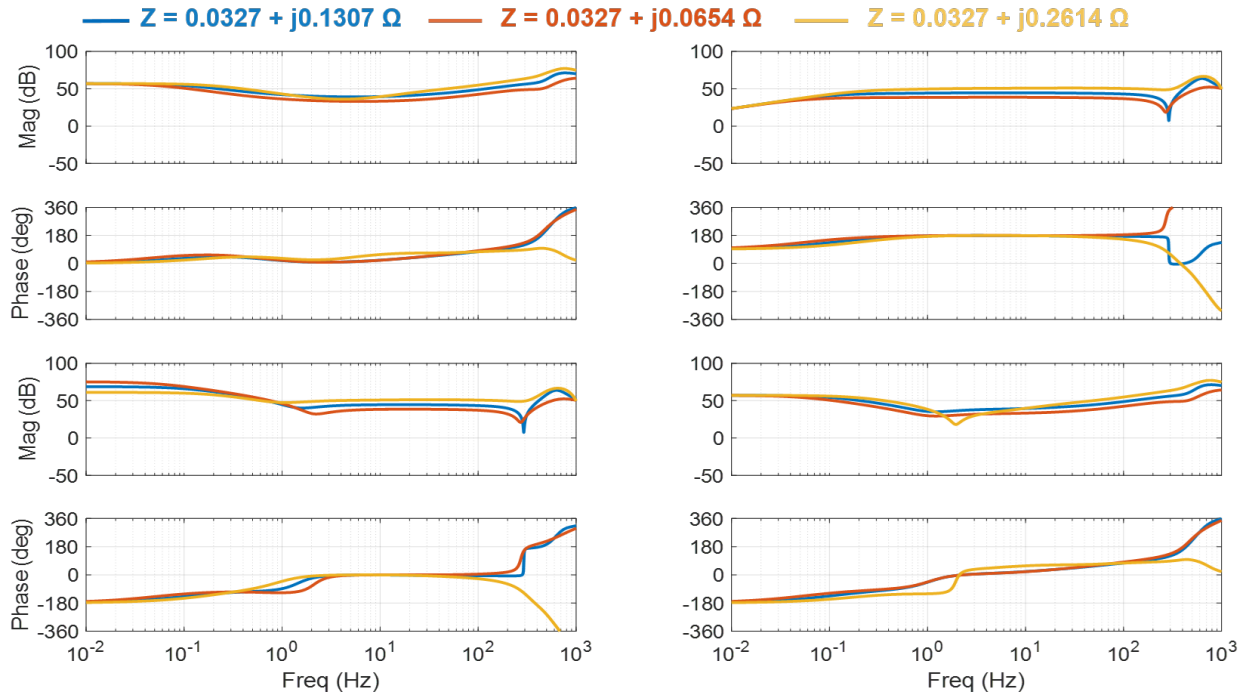

Figure 4.24: Variation of the virtual inductance under unity power factor.

Chapter 5

Stability Analysis of Grid-Tracking and Grid-Forming Controls in PV Inverters

5.1 Introduction

One major focus of this work is the stability of the connection of a PV inverter with grid-tracking and grid-forming controls. As mentioned in 4.5, the small range of the negative incremental impedance of the grid-forming controller is a favorable condition for a stable connection [83, 84]; however, this one factor does not guarantee stability nor instability. Therefore, an alternate means of stability analysis must be performed.

One method of analyzing the system stability is through the use of the character root method [29]. In this method, a full model of the system under study is constructed, as done in [85] and [24]. However, the inverter and controller are designed and built by a manufacturer and comprises proprietary information in which a full-detailed information packet is unattainable by the system operator. As such, only an educated guess of the parameters of the controller and control structure can be made based on the information provided by the manufacturer and the results obtained by the system operator when testing and implementing the device. Therefore, the stability analysis obtained via this method is not guaranteed to be accurate. Additionally, analyzing the stability of the system via time-domain simulations presents the same issues.

On the other hand, the generalized Nyquist Criterion (GNC) for stability analysis of three-phase systems only requires the dq ac impedance of the inverter and grid [26, 27, 67, 86–88]. The benefit of this method is that it does not require any knowledge of the controller nor its parameters. Similar to how the impedance of a machine can be measured at its

terminals through a series of open-circuit and closed-circuit tests, the impedance of the inverter, coupled with the controller, can be measured, as shown in [31, 32, 89].

The aim of this chapter is to apply the GNC to terminal dq ac impedance obtained in Chapter 4 and to assess the stability of the PV inverter with grid-tracking and grid-forming controls under unity power factor, fixed reactive power, and volt-var modes.

5.2 Generalized Nyquist Criterion for Stability

Consider that the PV inverter is connected to the distribution grid with line impedance $\mathbf{Z}_{grid} = 3.3552 + j4.3920\Omega$, as shown in Fig. 5.1. The terminal impedance of the PV inverter, $\mathbf{Z}_{pv}$, is measured at the PCC with the grid looking at the inverter while the grid impedance is measured looking at the grid. Then, the eigenvalues of the return ratio matrix, $\mathbf{L}_s$ is computed as

$$\mathbf{L}_s = \mathbf{Z}_{grid}(s) \cdot \mathbf{Y}_{PV} \tag{5.1}$$

where $\mathbf{Y}_{PV}$ is the inverse of $\mathbf{Z}_{pv}$. The resulting characteristic loci are swept over a range of frequencies and plotted on a Nyquist plot in the imaginary plane. The connection is stable if and only if the number of counter-clockwise encirclements of the critical point $(-1 + j0)$ by the characteristic loci is equal to the total number of right-hand plane poles [27]. Otherwise, the system is unstable.

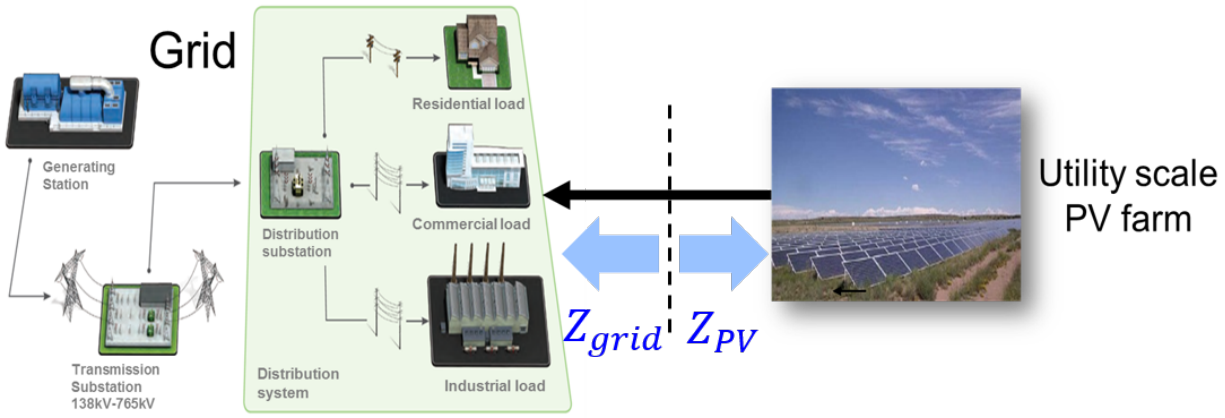

Figure 5.1: Measurement of terminal impedance for stability analysis.

5.2.1 Application of GNC to Terminal DQ Ac Impedance

The characteristic loci of the minor loop gain $\mathbf{L}(s) = \mathbf{Z}_{grid}\mathbf{Y}_{PV}$ under unity power factor is shown in Fig. 5.2 for an operating point of $P = 200$ kW and $Q = 0$ kvar. For both control schemes, since the inverter admittance and grid impedance have no right-hand plane poles and the characteristic loci do not encircle the critical point $(-1 + j0)$, then the system is considered stable for this operating point. Similarly, GNC is applied to the minor loop gain under fixed reactive power mode for an operating point of $P = 200$ kW and $Q = -75$ kvar, as shown in Fig. 5.3, and, as is observed, the loci do not encircle the critical point $(-1 + j0)$. Thus, the connection is considered stable under this control mode for both controllers.

Lastly, the characteristic loci of the minor loop gain under volt-var mode is shown in Fig. 5.4 for an operating point of $P = 200$ kW and $Q = -75$ kvar. In this case, since the inverter admittance and grid impedance have no right-hand plane poles and the characteristic loci λ_1 in the grid-tracking control scheme encircles the critical point $(-1 + j0)$, then the connection is considered unstable. On the other hand, for the same mode of operation at the same operating point, the inverter admittance and grid impedance for the grid-forming case have no right-hand plane poles and the loci do not encircle the critical point, therefore

the connection is stable. These results are confirmed in the time-domain simulation in Fig. 5.5, in which it is clear to see that the grid-tracking control currents oscillates whereas the grid-forming control reaches a stable steady-state operation.

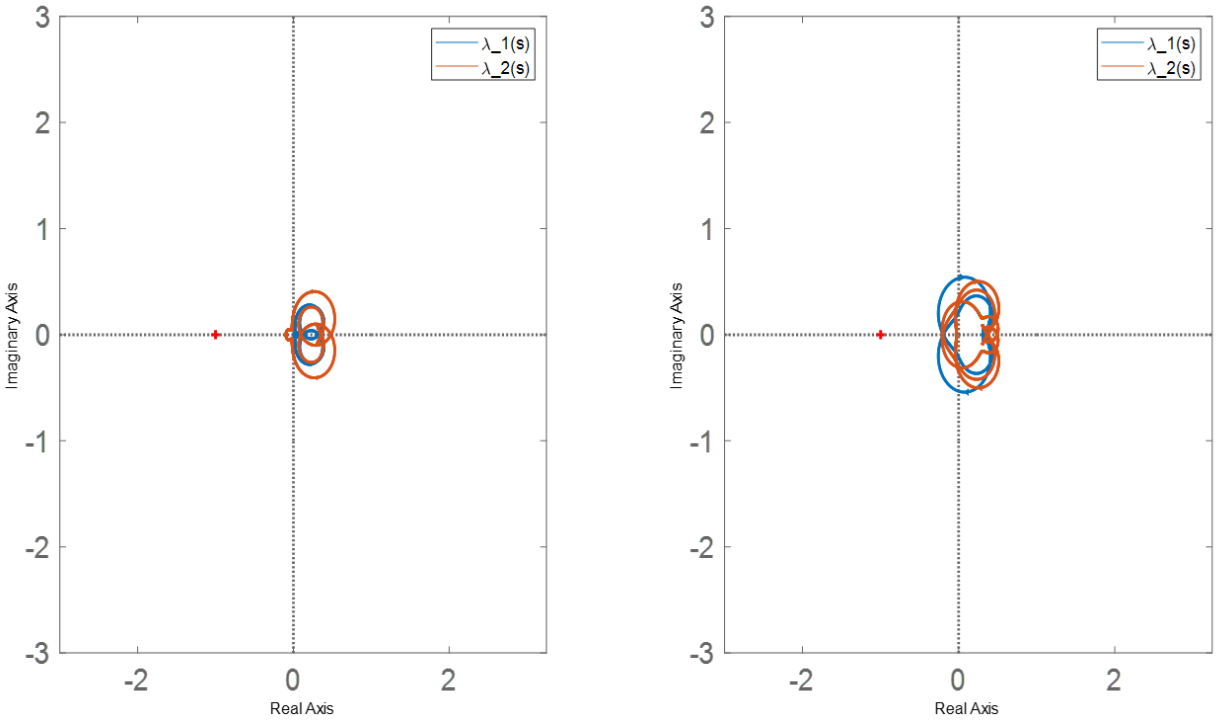

Figure 5.2: Characteristic loci of PV inverter under unity power factor mode for grid-tracking (left) and grid-forming (right).

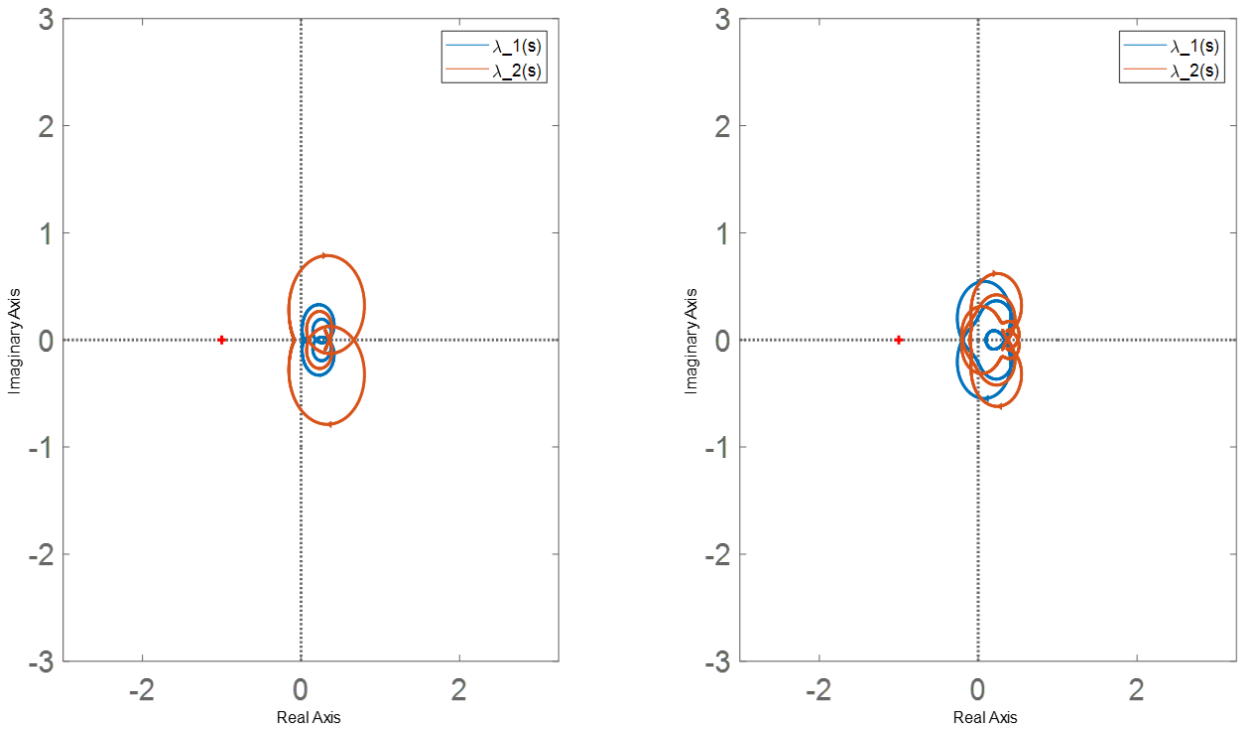

Figure 5.3: Characteristic loci of PV inverter under fixed reactive power mode for grid-tracking (left) and grid-forming (right).

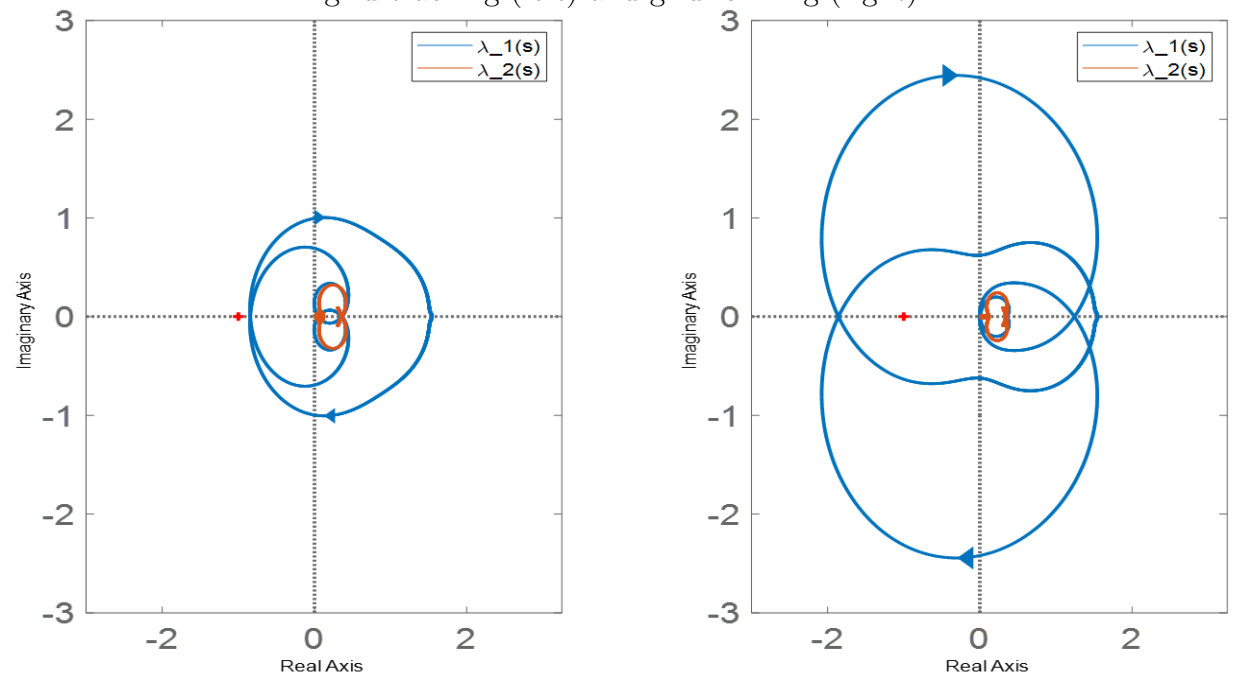

Figure 5.4: Characteristic loci of PV inverter under volt_var mode for grid-tracking (left) and grid-forming (right).

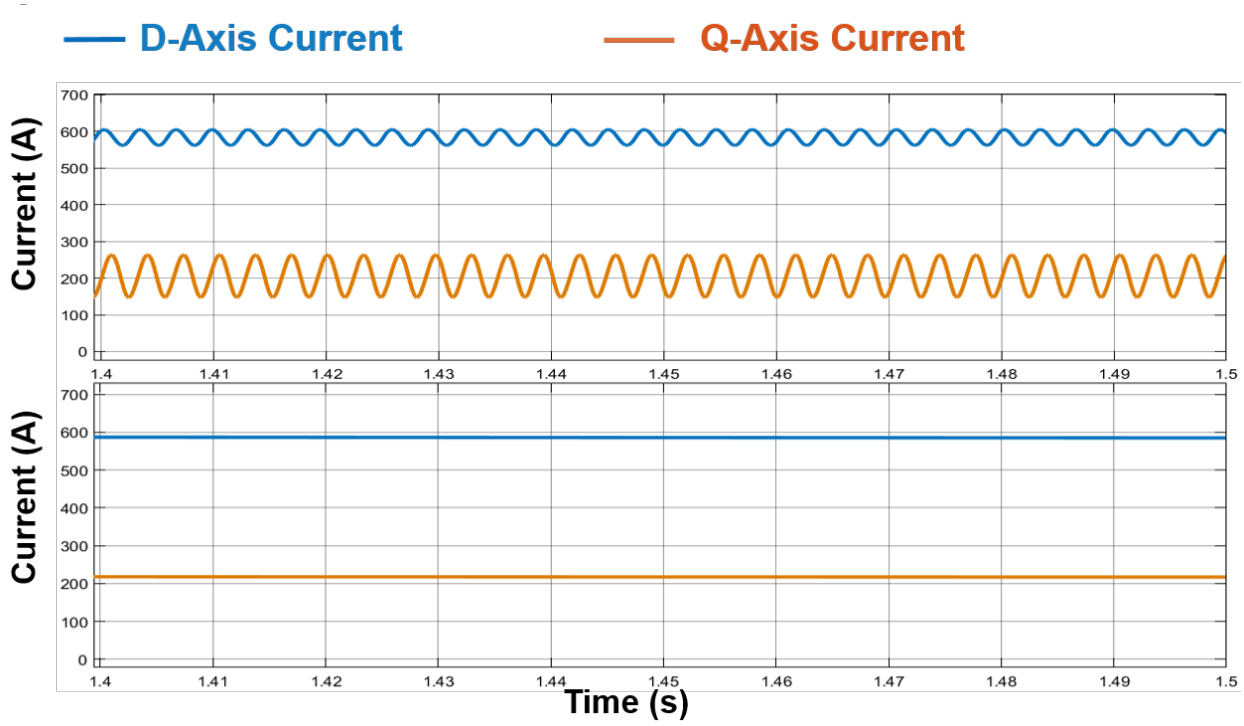

Figure 5.5: Time-domain simulation of PV inverter under volt-var mode for grid-tracking (top) and grid-forming (bottom).

5.2.2 Stable Power Injection Capability Comparison

As the grid-forming control enables a stable operation under volt-var control, the maximum power capability using grid-forming control should be analyzed and compared to the maximum stable power injection of the grid-tracking control. In order to perform this analysis, the power rating capability of the PV array in MATLAB Simulink is adjusted to find the maximum power injection capability for each control scheme. Alternatively, several PV arrays can be connected in parallel to achieve the same goal; however, since the purpose of this section is to analyze the maximum stable power injection capability for each control scheme, the dynamics introduced by the parallel operation of PV inverters is not considered and the first approach is used.

The maximum stable active power injection achievable by the grid-tracking control is found to be $P = 150$ kW. Due to the fact that the injection of the active power also affects the magnitude of the voltage at the PCC, then, according to the droop curve for volt-var mode defined in 3.3.2, the resulting reactive power injection is $Q = -52.5$ kvar. The characteristic loci of this power injection for grid-tracking control is shown on the left in Fig. 5.6, in which it can be seen that neither locus encircles the critical point, considering that the inverter admittance and grid impedance have no right-hand plane poles.

On the other hand, the maximum stable active power injection achievable by the grid-forming control is found to be $P = 320$ kW. Once again, this will also affect the amount of reactive power injected to the grid; at this operating point, the maximum reactive power capability of the inverter is injected: $Q = -112.5$ kvar. The characteristic loci of the minor loop gain for the grid-forming control scheme is shown on the right in Fig. 5.6, in which it can be seen that the characteristic loci do not encircle the critical point, once again considering that the inverter admittance and grid impedance have no right-hand plane poles. It is seen

that the grid-forming control scheme is capable of injecting 2.1 times the active power with the grid compared to the grid-tracking control under the volt-var mode of operation before dynamic interactions are triggered.

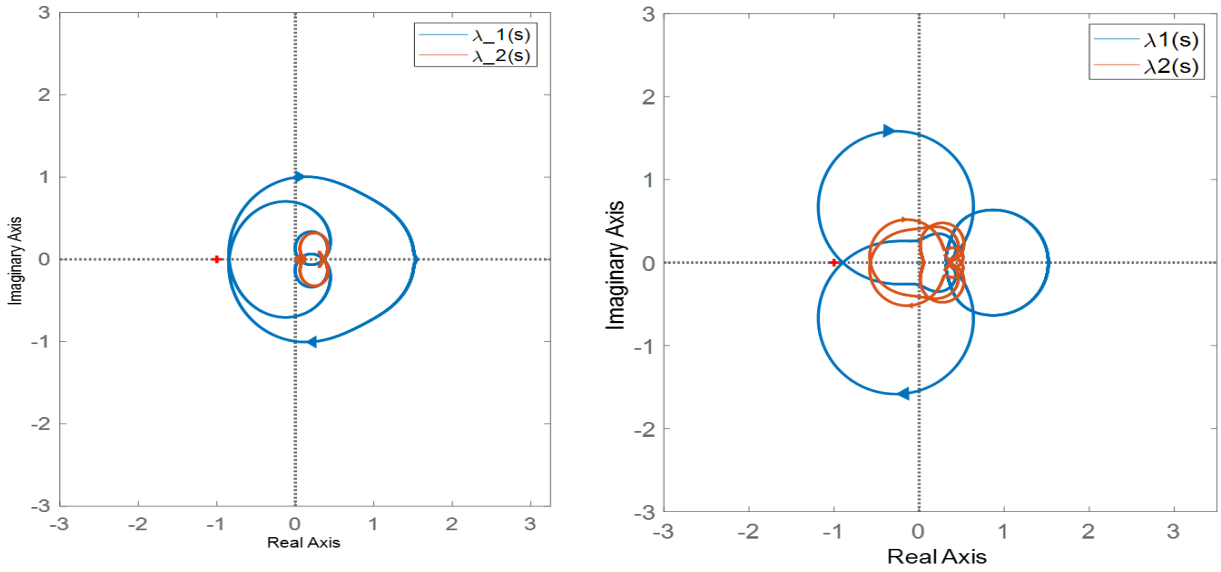

Figure 5.6: Characteristic loci of PV inverter for a nearly unstable case under volt-var mode for grid-tracking (left) and grid-forming (right).

Chapter 6

Conclusions and Future Work

6.1 Conclusions

In this work, the design procedure of a grid-tracking and grid-forming controller for a PV inverter is detailed. Specifically, the parameterization of the grid-forming control scheme is derived and discussed and the effect of the variation of key parameters relating to the emulation of a real synchronous machine on the control is analyzed. Furthermore, a comparison between the two controllers is drawn in terms of the small-signal terminal dq-frame ac impedance and via the stability of the connection of the inverter with the grid for each control structure using GNC.

The effect of the virtual inertia in the power-balance synchronization loop of the grid-forming control is clearly seen in the diagonal elements of the terminal impedance of the inverter, specifically in the Z_{qq} element. The virtual inertia also affects the shape of the terminal impedance at low frequencies, around the bandwidth of the power-balance loop; as a result, the tuning of these parameters are used for loop shaping to obtain a desired impedance at low frequency.

On the contrary, the virtual impedance parameters affect the PV inverter terminal impedance at the mid-frequency range. As explored in Chapter 4, it is seen that the virtual inductance affects the impedance considerably more compared to the virtual resistance primarily due to the fact that the X/R ratio of a synchronous machine is high. Even so, the effect of tuning the virtual resistance is not negligible as it further shapes the impedance loop in the diagonal terms, which contributes to the small-signal stability of the system.

By tuning the virtual parameters and designing appropriate loop bandwidths for the

cascaded grid-forming control, which are designed to be similar to those of the grid-tracking control, it is seen that the negative incremental impedance of the grid-forming control is one to two decades lower than the grid-tracking control. This is a favorable condition for stability and is indicative of the improved performance of the grid-forming control over the grid-tracking control under each mode of operation.

In comparing the small-signal stability of the grid-tracking control to the grid-forming control, both controllers achieve similar active power injection capability under unity power factor and fixed reactive power control modes. However, the active power injection capability of the grid-forming control under volt-var mode is two times that of the grid-tracking control due to the inherent lax power-balance synchronization, which is the main feature of this control structure. In this manner, the grid-forming control's benefits are twofold: first, it inherently regulates the frequency at the PCC, thus contributing to the overall frequency regulation of the system frequency, and, secondly, the grid-forming control allows for more flexible voltage regulation at higher active power operating points. As a result, the need for secondary voltage regulation units, such as static var compensators (SVCs) and STATCOMs, is reduced, therefore lowering the overall cost.

6.2 Future Work

In regards to future work, experimental verification of the proposed grid-forming controller for the PV inverter is required. Specifically, the terminal dq-frame impedance may be experimentally measured and compared to the closed form derivation from this work as well as the numerical linearization obtained from the simulation. The measured results should be compared to the measured results from the grid-tracking control structure and GNC can be applied to these results and compared to those from this work.

Additionally, the control scheme provided in this work may be improved upon. Such improvements include adding a dc-bus voltage regulation scheme to provide the reference for the active power in the power-balance synchronization loop. A proposed loop structure is to use a PI regulator, such as in the grid-tracking scheme, to provide this reference. Another improvement includes control over reserve energy sources, islanding and grid-connection support, parallel inverter operation, black-start capability, ride-through capability, and harmonic mitigation. The stability analysis with this improved control scheme should be analyzed and compared to the grid-tracking control scheme, with similar functionalities, for various operating modes.

References

[1] "Inventory of U.S. greenhouse gas emissions and sinks: 1990-2017," United States Environmental Protection Agency, Tech. Rep., 2019.

[2] W. Du, X. Chen, J. Cao, and H. Wang, "Performance of a phase locked loop as affected by power system dynamics," in *2015 IEEE 2nd International Future Energy Electronics Conference (IFEEC)*, Nov 2015, pp. 1–6.

[3] D. Dong, B. Wen, P. Mattavelli, D. Boroyevich, and Y. Xue, "Grid-synchronization modeling and its stability analysis for multi-paralleled three-phase inverter systems," in *2013 Twenty-Eighth Annual IEEE Applied Power Electronics Conference and Exposition (APEC)*, March 2013, pp. 439–446.

[4] H. Beck and R. Hesse, "Virtual synchronous machine," in *2007 9th International Conference on Electrical Power Quality and Utilisation*, Oct 2007, pp. 1–6.

[5] J. Driesen and K. Visscher, "Virtual synchronous generators," in *2008 IEEE Power and Energy Society General Meeting - Conversion and Delivery of Electrical Energy in the 21st Century*, July 2008, pp. 1–3.

[6] Q. Zhong and G. Weiss, "Synchronverters: Inverters that mimic synchronous generators," *IEEE Transactions on Industrial Electronics*, vol. 58, no. 4, pp. 1259–1267, April 2011.

[7] Q. Zhong, P. Nguyen, Z. Ma, and W. Sheng, "Self-synchronized synchronverters: Inverters without a dedicated synchronization unit," *IEEE Transactions on Power Electronics*, vol. 29, no. 2, pp. 617–630, Feb 2014.

[8] S. D'Arco, J. A. Suul, and O. B. Fosso, "Control system tuning and stability analysis of virtual synchronous machines," in *2013 IEEE Energy Conversion Congress and Exposition*, Sep. 2013, pp. 2664–2671.

[9] P. Rodriguez, I. Candela, C. Citro, J. Rocabert, and A. Luna, "Control of grid-connected power converters based on a virtual admittance control loop," in *2013 15th European Conference on Power Electronics and Applications (EPE)*, Sep. 2013, pp. 1–10.

[10] P. Rodriguez, I. Candela, and A. Luna, "Control of pv generation systems using the synchronous power controller," in *2013 IEEE Energy Conversion Congress and Exposition*, Sep. 2013, pp. 993–998.

[11] S. D'Arco, J. A. Suul, and O. B. Fosso, "A virtual synchronous machine implementation for distributed control of power converters in smartgrids," *Electric Power Systems Research*, vol. 122, pp. 180 – 197, 2015. [Online]. Available: http://www.sciencedirect.com/science/article/pii/S0378779615000024

[12] P. Rodríguez, C. Citro, J. I. Candela, J. Rocabert, and A. Luna, "Flexible grid connection and islanding of spc-based pv power converters," *IEEE Transactions on Industry Applications*, vol. 54, no. 3, pp. 2690–2702, May 2018.

[13] D. Remon, A. M. Cantarellas, E. Rakhshani, I. Candela, and P. Rodriguez, "An active power synchronization control loop for grid-connected converters," in *2014 IEEE PES General Meeting | Conference Exposition*, July 2014, pp. 1–5.

[14] S. D'Arco and J. A. Suul, "A synchronization controller for grid reconnection of islanded virtual synchronous machines," in *2015 IEEE 6th International Symposium on Power Electronics for Distributed Generation Systems (PEDG)*, June 2015, pp. 1–8.

[15] W. Zhang, A. Luna, and P. Rodriguez, "Start-up of virtual synchronous machine: Methods and experimental comparison," in *2018 2nd IEEE Conference on Energy Internet and Energy System Integration (EI2)*, Oct 2018, pp. 1–9.

[16] D. Remon, W. Zhang, A. Luna, I. Candela, and P. Rodriguez, "Grid synchronization of renewable generation systems using synchronous power controllers," in *2017 IEEE 6th International Conference on Renewable Energy Research and Applications (ICRERA)*, Nov 2017, pp. 169–174.

[17] W. Zhang, D. Remon, I. Candela, A. Luna, and P. Rodriguez, "Grid-connected converters with virtual electromechanical characteristics: experimental verification," *CSEE Journal of Power and Energy Systems*, vol. 3, no. 3, pp. 286–295, Sep. 2017.

[18] C. Li, R. Burgos, I. Cvetkovic, D. Boroyevich, L. Mili, and P. Rodriguez, "Analysis and design of virtual synchronous machine based statcom controller," in *2014 IEEE 15th Workshop on Control and Modeling for Power Electronics (COMPEL)*, June 2014, pp. 1–6.

[19] ——, "Evaluation and control design of virtual-synchronous-machine-based statcom for grids with high penetration of renewable energy," in *2014 IEEE Energy Conversion Congress and Exposition (ECCE)*, Sep. 2014, pp. 5652–5658.

[20] C. Li, R. Burgos, I. Cvetkovic, D. Boroyevich, and L. Mili, "Design, analysis and experimental evaluation of a virtual-synchronous-machine-based statcom with lcl filter,"

in *2015 IEEE Energy Conversion Congress and Exposition (ECCE)*, Sep. 2015, pp. 5771–5778.

[21] D. Remon, A. M. Cantarellas, J. D. Nieto, , and P. Rodriguez, "Aggregated model of a distributed pv plant using the synchronous power controller," in *2015 IEEE 24th International Symposium on Industrial Electronics (ISIE)*, June 2015, pp. 654–659.

[22] F. Garofalo, L. Iannelli, and F. Vasca, "Participation factors and their connections to residues and relative gain array," *IFAC Proceedings Volumes*, vol. 35, no. 1, pp. 125–130, 2002.

[23] S. Danielsen, O. B. Fosso, and T. Toftevaag, "Use of participation factors and parameter sensitivities in study and improvement of low-frequency stability between electrical rail vehicle and power supply," in *2009 13th European Conference on Power Electronics and Applications*, Sep. 2009, pp. 1–10.

[24] S. D'Arco, J. A. Suul, and O. B. Fosso, "Small-signal modelling and parametric sensitivity of a virtual synchronous machine," in *2014 Power Systems Computation Conference*, Aug 2014, pp. 1–9.

[25] L. Marin, A. Tarrasó, I. Candela, and P. Rodriguez, "Stability analysis of a droop-controlled grid-connected vsc," in *2018 IEEE Energy Conversion Congress and Exposition (ECCE)*, Sep. 2018, pp. 4161–4167.

[26] B. Wen, D. Boroyevich, R. Burgos, P. Mattavelli, and Z. Shen, "Analysis of d-q small-signal impedance of grid-tied inverters," *IEEE Transactions on Power Electronics*, vol. 31, no. 1, pp. 675–687, Jan 2016.

[27] B. Wen, "Stability analysis of three-phase ac power systems based on measured d-q

frame impedances," dissertation, Virginia Polytechnic Institute and State University, 2015.

[28] B. Wen, D. Boroyevich, R. Burgos, P. Mattavelli, and Z. Shen, "Inverse nyquist stability criterion for grid-tied inverters," *IEEE Transactions on Power Electronics*, vol. 32, no. 2, pp. 1548–1556, Feb 2017.

[29] Y. Tang, R. Burgos, C. Li, and D. Boroyevich, "Ac impedance derivation of utility scale pv farm," in *2017 IEEE Energy Conversion Congress and Exposition (ECCE)*, Oct 2017, pp. 4049–4054.

[30] ——, "Stability assessment of utility pv integration to the distributed systems based on d-q frame impedances and gnc," in *2017 IEEE 18th Workshop on Control and Modeling for Power Electronics (COMPEL)*, July 2017, pp. 1–6.

[31] ——, "Stability impact of pv inverter generation on medium voltage distribution systems," in *2018 International Power Electronics Conference (IPEC-Niigata 2018 -ECCE Asia)*, May 2018, pp. 3705–310.

[32] ——, "Utility-scale pv inverter impedances in d-q frame under different q-control modes," in *2018 IEEE Energy Conversion Congress and Exposition (ECCE)*, Sep. 2018, pp. 3725–3731.

[33] "Ieee standard for interconnection and interoperability of distributed energy resources with associated electric power systems interfaces," *IEEE Std 1547-2018 (Revision of IEEE Std 1547-2003)*, pp. 1–138, April 2018.

[34] F. Blaabjerg, R. Teodorescu, M. Liserre, and A. V. Timbus, "Overview of control and grid synchronization for distributed power generation systems," *IEEE Transactions on Industrial Electronics*, vol. 53, no. 5, pp. 1398–1409, Oct 2006.

[35] M. Bobrowska-Rafal, K. Rafal, M. Jasinski, and M. Kazmierkowski, "Grid synchronization and symmetrical components extraction with pll algorithm for grid connected power electronic converters - a review," *Bulletin of the Polish Academy of Sciences: Technical Sciences*, vol. 59, 12 2011.

[36] S. K. Chung, "Phase-locked loop for grid-connected three-phase power conversion systems," *IEE Proceedings - Electric Power Applications*, vol. 147, no. 3, pp. 213–219, May 2000.

[37] P. Rodriguez, J. Pou, J. Bergas, J. I. Candela, R. P. Burgos, and D. Boroyevich, "Decoupled double synchronous reference frame pll for power converters control," *IEEE Transactions on Power Electronics*, vol. 22, no. 2, pp. 584–592, March 2007.

[38] L. Hadjidemetriou, E. Kyriakides, and F. Blaabjerg, "A new hybrid pll for interconnecting renewable energy systems to the grid," in *2012 IEEE Energy Conversion Congress and Exposition (ECCE)*, Sep. 2012, pp. 2075–2082.

[39] P. Rodriguez, J. Pou, J. Bergas, I. Candela, R. Burgos, and D. Boroyevic, "Double synchronous reference frame pll for power converters control," in *2005 IEEE 36th Power Electronics Specialists Conference*, June 2005, pp. 1415–1421.

[40] Lie Xu, B. R. Andersen, and P. Cartwright, "Vsc transmission operating under unbalanced ac conditions - analysis and control design," *IEEE Transactions on Power Delivery*, vol. 20, no. 1, pp. 427–434, Jan 2005.

[41] W. Sinsukthavorn, E. Ortjohann, A. Mohd, N. Hamsic, and D. Morton, "Control strategy for three-/four-wire-inverter-based distributed generation," *IEEE Transactions on Industrial Electronics*, vol. 59, no. 10, pp. 3890–3899, Oct 2012.

[42] M. G. Villalva, T. G. D. Siqueira, and E. Ruppert, "Voltage regulation of photovoltaic arrays: small-signal analysis and control design," *IET Power Electronics*, vol. 3, no. 6, pp. 869–880, Nov 2010.

[43] *Two-Level, Three-Phase Voltage-Sourced Converter*. John Wiley Sons, Ltd, 2010, ch. 5, pp. 115–126. [Online]. Available: https://onlinelibrary.wiley.com/doi/abs/10.1002/9780470551578.ch5

[44] "Ieee recommended practice and requirements for harmonic control in electric power systems," *IEEE Std 519-2014 (Revision of IEEE Std 519-1992)*, pp. 1–29, June 2014.

[45] D. Wuest, H. Stemmler, and G. Scheuer, "A comparison of different circuit configurations for an advanced static var compensator (asvc)," in *PESC '92 Record. 23rd Annual IEEE Power Electronics Specialists Conference*, June 1992, pp. 521–529 vol.1.

[46] Y. Tang and L. Xu, "A new converter topology for advanced static var compensation in high power applications," in *Conference Record of the 1993 IEEE Industry Applications Conference Twenty-Eighth IAS Annual Meeting*, Oct 1993, pp. 947–953 vol.2.

[47] *Three-Level, Three-Phase, Neutral-Point Clamped, Voltage-Sourced Converter*. John Wiley Sons, Ltd, 2010, ch. 6, pp. 127–159. [Online]. Available: https://onlinelibrary.wiley.com/doi/abs/10.1002/9780470551578.ch6

[48] Jih-Sheng Lai and Fang Zheng Peng, "Multilevel converters-a new breed of power converters," *IEEE Transactions on Industry Applications*, vol. 32, no. 3, pp. 509–517, May 1996.

[49] K. V. Patil, R. M. Mathur, J. Jiang, and S. H. Hosseini, "Distribution system compensation using a new binary multilevel voltage source inverter," *IEEE Transactions on Power Delivery*, vol. 14, no. 2, pp. 459–464, April 1999.

[50] Gui-Jia Su, "Multilevel dc-link inverter," *IEEE Transactions on Industry Applications*, vol. 41, no. 3, pp. 848–854, May 2005.

[51] E. N. Abildgaard and M. Molinas, "Modelling and control of the modular multilevel converter (mmc)," *Energy Procedia*, vol. 20, pp. 227 – 236, 2012, technoport 2012 - Sharing Possibilities and 2nd Renewable Energy Research Conference (RERC2012). [Online]. Available: http://www.sciencedirect.com/science/article/pii/S1876610212007539

[52] A. Perez-Santiago, M. Lugo-Alvarez, L. Sepulveda-Hernandez, and E. I. Ortiz-Rivera, "Design of a nine-switch three-phase multilevel inverter with a pv array source," in *2018 IEEE Texas Power and Energy Conference (TPEC)*, Feb 2018, pp. 1–6.

[53] V. F. Pires, A. Cordeiro, D. Foito, and J. F. Silva, "Three-phase multilevel inverter for grid-connected distributed photovoltaic systems based in three three-phase two-level inverters," *Solar Energy*, vol. 174, pp. 1026 – 1034, 2018. [Online]. Available: http://www.sciencedirect.com/science/article/pii/S0038092X18309770

[54] H. . Krug, T. Kume, and M. Swamy, "Neutral-point clamped three-level general purpose inverter - features, benefits and applications," in *2004 IEEE 35th Annual Power Electronics Specialists Conference (IEEE Cat. No.04CH37551)*, vol. 1, June 2004, pp. 323–328 Vol.1.

[55] M. J. Chudasama, S. Chauhan, V. Patel, and P. P. N. Tekwani, "Simulation, design, and analysis of three-level shunt active harmonic filter using t-type npc topology," 02 2017.

[56] S. Hiti, "Modeling and control of three-phase pwm converters," dissertation, Virginia Polytechnic Institute and State University, 1995.

[57] S. Hiti, D. Boroyevich, and C. Cuadros, "Small-signal modeling and control of three-phase pwm converters," in *Proceedings of 1994 IEEE Industry Applications Society Annual Meeting*, vol. 2, Oct 1994, pp. 1143–1150 vol.2.

[58] L. Marin, A. Tarrasó, I. Candela, and P. Rodriguez, "Stability analysis of a droop-controlled grid-connected vsc," in *2018 IEEE Energy Conversion Congress and Exposition (ECCE)*, Sep. 2018, pp. 4161–4167.

[59] L. Harnefors, A. G. Yepes, A. Vidal, and J. Doval-Gandoy, "Passivity-based stabilization of resonant current controllers with consideration of time delay," *IEEE Transactions on Power Electronics*, vol. 29, no. 12, pp. 6260–6263, Dec 2014.

[60] D. Pan, X. Ruan, C. Bao, W. Li, and X. Wang, "Capacitor-current-feedback active damping with reduced computation delay for improving robustness of lcl-type grid-connected inverter," *IEEE Transactions on Power Electronics*, vol. 29, no. 7, pp. 3414–3427, July 2014.

[61] S. Buso and P. Mattavelli, *Digital Control in Power Electronics*. Morgan Claypool, 2006. [Online]. Available: https://ieeexplore.ieee.org/document/6813194

[62] S. K. Chung, "A phase tracking system for three phase utility interface inverters," *IEEE Transactions on Power Electronics*, vol. 15, no. 3, pp. 431–438, May 2000.

[63] D. G. Holmes, T. A. Lipo, B. P. McGrath, and W. Y. Kong, "Optimized design of stationary frame three phase ac current regulators," *IEEE Transactions on Power Electronics*, vol. 24, no. 11, pp. 2417–2426, Nov 2009.

[64] S. Ali, I. Setiawan, and S. Handoko, "Design and performance test of three phased synchronous reference frame-phase locked loop (srf-pll) using dspic30f4011," in *2018 5th*

International Conference on Information Technology, Computer, and Electrical Engineering (ICITACEE), Sep. 2018, pp. 51–56.

[65] S. Golestan, M. Monfared, and F. D. Freijedo, "Design-oriented study of advanced synchronous reference frame phase-locked loops," *IEEE Transactions on Power Electronics*, vol. 28, no. 2, pp. 765–778, Feb 2013.

[66] A. Kulkarni and V. John, "Analysis of bandwidth–unit-vector-distortion tradeoff in pll during abnormal grid conditions," *IEEE Transactions on Industrial Electronics*, vol. 60, no. 12, pp. 5820–5829, Dec 2013.

[67] B. Wen, D. Boroyevich, P. Mattavelli, Z. Shen, and R. Burgos, "Influence of phase-locked loop on input admittance of three-phase voltage-source converters," in *2013 Twenty-Eighth Annual IEEE Applied Power Electronics Conference and Exposition (APEC)*, March 2013, pp. 897–904.

[68] W. Zhang, C. Citro, A. M. Cantarellas, D. Remon, A. Luna, and P. Rodriguez, "Tuning of proportional resonant controllers for three phase pv power converters with lcl+trap filter," in *2014 IEEE PES T D Conference and Exposition*, April 2014, pp. 1–5.

[69] K. H. Ahmed, A. M. Massoud, S. J. Finney, and B. W. Williams, "A modified stationary reference frame-based predictive current control with zero steady-state error for lcl coupled inverter-based distributed generation systems," *IEEE Transactions on Industrial Electronics*, vol. 58, no. 4, pp. 1359–1370, April 2011.

[70] I. J. Gabe, V. F. Montagner, and H. Pinheiro, "Design and implementation of a robust current controller for vsi connected to the grid through an lcl filter," *IEEE Transactions on Power Electronics*, vol. 24, no. 6, pp. 1444–1452, June 2009.

[71] C. Bao, X. Ruan, X. Wang, W. Li, D. Pan, and K. Weng, "Step-by-step controller design for lcl-type grid-connected inverter with capacitor–current-feedback active-damping," *IEEE Transactions on Power Electronics*, vol. 29, no. 3, pp. 1239–1253, March 2014.

[72] T. Huang, X. Shi, Y. Sun, and D. Wang, "Three-phase photovoltaic grid-connected inverter based on feedforward decoupling control," in *2013 International Conference on Materials for Renewable Energy and Environment*, vol. 2, Aug 2013, pp. 476–480.

[73] J. Alcalá, E. Bárcenas, and V. Cárdenas, "Practical methods for tuning pi controllers in the dc-link voltage loop in back-to-back power converters," in *12th IEEE International Power Electronics Congress*, Aug 2010, pp. 46–52.

[74] M. Tankari, M. Camara, B. Dakyo, and C. Nichita, "Ultracapacitors and batteries integration for power fluctuations mitigation in wind-pv-diesel hybrid system," *International Journal Of Renewable Energy Research*, vol. 1, pp. 86–95, 01 2011.

[75] A. Hajizadeh and M. A. Golkar, "Control of hybrid fuel cell/energy storage distributed generation system against voltage sag," *International Journal of Electrical Power Energy Systems*, vol. 32, no. 5, pp. 488 – 497, 2010. [Online]. Available: http://www.sciencedirect.com/science/article/pii/S0142061509001574

[76] K. Turitsyn, P. Sulc, S. Backhaus, and M. Chertkov, "Options for control of reactive power by distributed photovoltaic generators," *Proceedings of the IEEE*, vol. 99, no. 6, pp. 1063–1073, June 2011.

[77] M. Farivar, C. R. Clarke, S. H. Low, and K. M. Chandy, "Inverter var control for distribution systems with renewables," in *2011 IEEE International Conference on Smart Grid Communications (SmartGridComm)*, Oct 2011, pp. 457–462.

[78] H. Qamar, H. Qamar, A. Vaccaro, and N. Ahmed, "Reactive power control for voltage regulation in the presence of massive pervasion of distributed generators," in *2017 IEEE International Conference on Environment and Electrical Engineering and 2017 IEEE Industrial and Commercial Power Systems Europe (EEEIC / I CPS Europe)*, June 2017, pp. 1–5.

[79] Y. Tang, R. Burgos, C. Li, and D. Boroyevich, "Impact of pv inverter penetration on voltage profile and power loss in medium voltage distribution systems," in *2016 IEEE 17th Workshop on Control and Modeling for Power Electronics (COMPEL)*, June 2016, pp. 1–8.

[80] S. Chapman, *Electric Machinery and Power System Fundamentals*, ser. McGraw-Hill series in electrical and computer engineering. McGraw-Hill, 2002. [Online]. Available: https://books.google.com/books?id=suceAQAAIAAJ

[81] L. Zhang, L. Harnefors, and H. Nee, "Power-synchronization control of grid-connected voltage-source converters," *IEEE Transactions on Power Systems*, vol. 25, no. 2, pp. 809–820, May 2010.

[82] P. Rodriguez Cortés, J. I. Candela Garcia, J. R. Delgado, and R. Teodorescu, "Synchronous power controller for a generating system based on static power converters," Patent, Oct. 20, 2015, US9166508.

[83] S. Anand and B. G. Fernandes, "Reduced-order model and stability analysis of low-voltage dc microgrid," *IEEE Transactions on Industrial Electronics*, vol. 60, no. 11, pp. 5040–5049, Nov 2013.

[84] Z. Liu, M. Su, Y. Sun, H. Han, X. Hou, and J. M. Guerrero, "Stability analysis of dc microgrids with constant power load under distributed control

methods," *Automatica*, vol. 90, pp. 62 – 72, 2018. [Online]. Available: http://www.sciencedirect.com/science/article/pii/S0005109817306386

[85] L. Marin, A. Tarras´, I. Candela, and P. Rodriguez, "Stability analysis of a grid-connected vsc controlled by spc," in *2018 7th International Conference on Renewable Energy Research and Applications (ICRERA)*, Oct 2018, pp. 1209–1214.

[86] B. Wen, D. Boroyevich, R. Burgos, P. Mattavelli, and Z. Shen, "Small-signal stability analysis of three-phase ac systems in the presence of constant power loads based on measured d-q frame impedances," *IEEE Transactions on Power Electronics*, vol. 30, no. 10, pp. 5952–5963, Oct 2015.

[87] B. Wen, D. Boroyevich, P. Mattavelli, R. Burgos, and Z. Shen, "Modeling the output impedance negative incremental resistance behavior of grid-tied inverters," in *2014 IEEE Applied Power Electronics Conference and Exposition - APEC 2014*, March 2014, pp. 1799–1806.

[88] B. Wen, D. Boroyevich, P. Mattavelli, Z. Shen, and R. Burgos, "Experimental verification of the generalized nyquist stability criterion for balanced three-phase ac systems in the presence of constant power loads," in *2012 IEEE Energy Conversion Congress and Exposition (ECCE)*, Sep. 2012, pp. 3926–3933.

[89] Y. Tang, R. Burgos, B. Wen, D. Boroyevich, J. Verhulst, D. Vrtachnik, and M. Belkhayat, "A novel dq impedance measurement method in three-phase balanced systems," in *2019 20th Workshop on Control and Modeling for Power Electronics (COMPEL)*, June 2019, pp. 1–5.